Behaviour and Analysis of Strain Hardening Fiber Reinforced Cementitious Composites Under Shear and Flexure

Najmeh Eshghi

A THESIS SUBMITTED TO

THE FACULTY OF GRADUATE STUDIES

IN PARTIAL FULFILLMENT OF THE REQUIREMENTS

FOR THE DEGREE OF

MASTER OF APPLIED SCIENCE

GRADUATE PROGRAM IN CIVIL ENGINEERING

YORK UNIVERSITY

TORONTO, ONTARIO

December 2018

ABSTRACT

Significant effort has been vested over the years in quantifying the contribution of concrete to the shear strength of concrete members. By introduction of novel cementitious material, a much greater need to develop a standard to treat the concrete in a systematic manner is felt.

In this thesis, an alternative framework of analysis to interpret the shear failure and the corresponding strength of the failure mechanism is suggested which gives an insight into a new interpretation of shear failure and relates to the state of bond of reinforcement over the entire span of a member. This approach is adaptable to be used for new concrete materials such as Strain Hardening Fiber Reinforced Cementitious Composites.

An experimental program is also designed to provide a basis for the development of design rules which are prerequisite for the introduction of these novel materials in new construction. All experiments are conducted at York University.

AKNOWLEDGMENT

I would like to express my deepest gratitude to my supervisor Professor Voula (S.J) Pantazopoulou for her unwavering support and encouragement over the years. Her expertise and immense knowledge have always helped me through difficult times. She is an exemplary supervisor and a great human being to be followed. I indeed consider myself very fortunate to have had the chance to be her student.

Appreciation is also extended to my friends and colleges who have helped me throughout the experimental program of this study: Roberto, Adrien, Mena, Rita, Kostas. I also would like to express my appreciation to our Laboratory Technician at York University, Riad Rajab, for his technical support throughout the experimental program.

I am also deeply and forever indebted to my parents for their love, support and encouragement throughout my entire life. Words cannot describe my gratitude and appreciation towards my husband, Mehdi. His support and kindness are not comparable to any other motivation.

TABLE OF CONTENTS

LIST OF TABLES

LIST OF FIGURES

LIST OF NOTATIONS

Latin Upper-Case Symbols

A_s	area of longitudinal reinforcements
$A_{c,eff}$	effective area of concrete cover engaged in tension
A_{sl}	the cross-sectional area of the reinforcement which extends $\geq l_{bd} + d$ beyond the considered section
A_{st}	the area of the stirrups legs crossing the splitting plane
E	Measured modulus of elasticity in tension
E_c	Young's Modulus of concrete
E_f	Young's Modulus of fiber
E_s	Young's Modulus of steel bar reinforcement
F_{ctk}	the characteristic value of the tensile strength for the concrete matrix, in MPa;
F_{Ftuk}	the characteristic value of the ultimate residual tensile strength for FRC, by considering $w_u = 1.5mm$
F_{max}	maximum force undertaken in flexural tests
F_{sA}	the tension force in the longitudinal reinforcement at the end support at ultimate load
$F_{R,4}$	load recorded at $CMOD_4$
I_g	area moment of inertia
L	span of the specimen
L_b	available anchorage length measured from the critical section to the end of the bar length
L_s	shear span length
M	moment at the cracked section
M_u	factored internal moment
M_0	maximum constant moment in the middle of a beam
M_{cr}	cracking moment
M_{Ed}	design moment of stress resultants determined from the factored design loads
$M_{u,cal}$	calculated maximum moment (based on reinforcement yielding)
$M_{u,max}$	maximum absolute values of the internal forces in the region between the maximum bending moment and the zero-bending moment in which the considered section is located
$M_{u,test}$	Experimental maximum moment

M_y	yielding moment
T	ultimate strength of the tension tie
V	ultimate shear capacity of the section
V_{ACI}	shear strength of concrete calculated as per ACI 318-14
V_c	concrete contribution to shear strength
V_{cc}	shear force across the compression region
V_{cd}	design shear capacity of a linear member without any shear reinforcement steels, excluding the strength exerted by reinforcing fiber
V_{Ed}	design shear of stress resultants determined from the factored design loads
V_{FRC}	vertical component of the diagonal tension resistance provided by the fibers
V_{fd}	design shear capacity of reinforcing fiber
V_s	steel contribution to shear strength of a beam
V_{st}	stirrups contribution to shear strength of a beam
V_{Rd}	design value for the shear resistance in members with conventional longitudinal reinforcement and without shear reinforcement
$V_{Rd,c}$	design value of concrete contribution to shear strength
$V_{Rd,F}$	design value of the fiber contribution to the shear strength
$V_{Rd,Fmin}$	minimum shear resistance
V_{cd}	shear strength contributions from the concrete compression zone
V_{fd}	shear strength contribution from the tension zone owing to fibers that bridge the tension cracks
$V_{r,max}$	factored shear resistance
V_u	factored internal shear force
V_{uc}	shear resisted by concrete
V_{uf}	contribution of fibers to shear capacity
$V_{u,max}$	maximum absolute values of the internal shear force in the region between the maximum bending moment and the zero-bending moment in which the considered section is located
V_{test}	experimental shear strengths of beams without any stirrups
V_{yd}	design shear capacity of a linear member consisting solely of HPFRCC and reinforcing steel
T_s	force in the tension reinforcement
T_f	tensile force transferred across the critical diagonal crack through fiber tension

Latin Lower-Case Symbols

a shear span

a_A support plate dimensions

b cross section width

b_A beam overhang beyond the end supports of the beams

b_w smallest width of the cross-section in the tensile zone, in mm.

$b_{v,eff}$ effective flange width for shear strength

c neutral axis depth

c_1 clear cover of the reinforcing bars

d Effective depth of cross section

d_0 maximum of effective depth d or 4 in

d_b diameter of one reinforcing bar

d_g maximum size of the aggregate particles

d_f fiber diameter

d_{st} average diameter of longitudinal tension reinforcement

d_t distance from the extreme compression fiber of the member to the centroid of the reinforcement nearest the tension face.

f_{1c} uniaxial strength of a slender prism

$f_{1ct,ca}$ calculated value of tensile strength

$f_{1ctm,c}$ calculated axial tensile strength

f_b bond stress

$f_{b,0}$ design bond strength

f_{bd} ultimate bond strength

f_{bf} bond stress of fiber

$f_{c,cyl}$ cylinder strength of concrete

f_{ck} the characteristic value of cylindrical compressive strength

f_{crm} Average cracking strength of the FRC matrix

f_{ct} tensile resistance of the concrete

f_{R1} residual strength significant for service condition

f_{R3} residual strength significant for ultimate condition

$f_{Rk,4}$ characteristic residual flexural tensile strength at the crack mouth opening $\mathrm{CMOD4} = 7.5$ (or $\delta_{\mathrm{R},4} = 3\ \mathrm{mm}$) is determined by the CMOD (crack mouth opening displacement) - or deflection controlled bending test on a notched prism according to standards.

f_t concrete tensile strength

f_{tf} tensile strength provided by the fibers over a plane of unit area

$f_{t,fl}$ tensile strength of concrete obtained indirectly from the 4PB tests conducted on unreinforced beams

$f_{t,u}$ Specified ultimate tensile strength for THFRC

f_y yielding strength of longitudinal reinforcements

$f_{y,st}$ yielding strength of stirrups

f_{vd} design tensile yield strength of HPFRCC

f_u ultimate strength of reinforcements

f'_c specified compressive strength of concrete; the compressive cylinder strength

f'_{cd} design compressive strength of concrete

f_b^{max} maximum bond strength in bond slip relationship

h cross section height

h_{sp} distance between tip of the notch and top of cross section

Jd moment lever arm

k_s size effect factor

$l_{b,cal}$ calculated anchorage length

$l_{b,req}$ required anchorage length

$l_{b,prov}$ provided anchorage length

l_{crit} critical fiber length for fiber fracture

l_{D1} disturbed length

l_f available fiber length

l_n length of beam between two supports

l_p the length of bond plastification

l_r debonded length

m initial slope of the load-deflection curve

n_b number of reinforcing bars (restrained by a stirrup)

p_{tr} transverse pressure that engages frictional resistance at the splitting plane.

s_x effective crack spacing in the longitudinal direction

n elastic modulus ratio

s bar slip

s_{st} the spacing of stirrups

t thickness of the specimens

w crack width at the mid-height on the section

w_0 Crack opening displacement in softening model of THFRC (used in inverse analysis only)

w_{cr} current crack opening displacement

w_u maximum crack opening accepted in structural design

x height of the compression zone

x_{cr1} location of first crack

y depth of the tensile region of the cross section

y_g distance of the reinforcement from the centroid of the cross section

z internal moment lever arm

Greek Symbols

α_f aspect ratio of the fiber

$\beta_1 c$ Whitney's stress block

β_u angle of the diagonal crack surface to the member axis

γ_c is the material safety factor

γ_d size effect factor

δ_i Displacement corresponding to the load P_i in the four-point bending test for the THFRC inverse analysis

ε_c concrete strain

ε_f fiber strain

ε_{fl} strain in the bar and concrete at the level of the reinforcement,

ε_s steel bar strain

ε_{so} the tension strain at the critical cross section

ε_{sh} strain hardening strain of longitudinal reinforcement

ε_{sy} yielding strain of longitudinal reinforcement

ε_{t0} Computed strain value in THFRC inverse analysis

ε_{tu} Specified ultimate tensile strain for THFRC

ε_u ultimate strain of longitudinal reinforcement

ζ coefficient for inner lever arm

κ_c coefficient for maximum stress of stress block over full depth

λ	modification factor for light weight concrete
ξ	combined size and slenderness factor
ρ	longitudinal reinforcement ratio
ρ_ℓ	ratio of longitudinal tension reinforcement crossing the flexure-shear crack.
ρ_f	volumetric ratio of fiber
σ	equivalent flexural tensile stress
σ_{ct}	average compressive normal stress developed by flexural moment
σ_{fu}	tensile strength of the fiber
ϕ	inclined crack angle
σ_{1f}	principal stress in x direction
σ_{3f}	principal stress in y direction
σ_f	normal stress
σ_{ff}	normal stress on the failure plane
$(\sigma_t)_{ave}$	Average tensile stress determined from ASTM 1609
τ_b	bond stress between the fibers and the concrete matrix
τ_f	maximum shear stresses that concrete can attain just before failure
τ_{ff}	shear stress on the failure plane
τ_{fd}	design value of the increase in shear strength in the tension zone due to steel fibers
ω_1	mechanical reinforcement ratio of tension chord

CHAPTER 1: INTRODUCTION

1.1 Background

Concrete is one of the most widely used construction materials. The main disadvantage of conventional concrete is its low tensile strength and limited ductility in tension. The inherent brittleness of cementitious material leads to creation of cracks at very low principal tensile strain levels (in the order of 0.0001), which disrupt the stress transfer across the crack. When microcracks align and form a major crack, the tensile strength normal to the crack path is lost and no more load can be carried, and failure would occur unless reinforcement crosses the crack path (Georgiou 2017).

To control the propagation of cracks which limit concrete functionality, longitudinal and transverse reinforcement is used. Longitudinal reinforcement provides flexural strength, but general Reinforced Concrete (RC) mechanics are only possible by the presence of shear reinforcement. The common and traditional option to suppress the occurrence of diagonal tension failure in the web of structural members is through the use of stirrups. However, reinforcement congestion (especially in coupling beams), labour intensity, susceptibility of stirrups to corrosion, and labour cost underscores the need for a more effective option. Fiber Reinforced Concrete (FRC) has been developed with the intent to be used as a possible remedy to this problem. However, fibers had not been able to secure the ductility in conventional concrete that was provided by stirrups – the reason is that fibers can only suppress flaws that do not exceed their range of action, which is of the same order as their size. However, conventional concrete contains aggregates that may be considered flaws in terms of material continuity. They intercept the transfer mechanism between fibers through the gel, having a length dimension that is often of comparable size to that of the fibers. This is why FRC has been considered an improvement to plain concrete, providing through the fibers a small to moderate amount of residual toughness after cracking, but being primarily a softening material in tension. Recently, however, this obstacle has been bypassed by eliminating the coarse aggregate from fiber reinforced mixes, the result being a mortar-like concrete which exhibits spectacular tensile strain capacity after cracking. This concrete has been termed Ultra-

High-Performance Concrete (UHPC) and holds promise for many an innovation in the field of structural engineering.

In fact, use of fibers in construction was an ancient idea, however, in the last decade, it is leading novel developments in the area of high performance cementitious materials. In the ancient past fibers such as straw, horsehair, or wool were used in mud bricks and lime mortars. However, in 1874, Berard was the first who patented the first fiber reinforced concrete (Balaguru and Shah 1992). Since then, the concept of fibers as mass reinforcement was born and many different types of fibers such as silicon, carbon, ceramics, glass, nylon, polypropylene, asbestos were tested. For a long time, fiber reinforced concrete was not popular because it was difficult to make in the field a dependable material with the coarse aggregates in the mix, as voids were created due to poor workability impacting negatively rather than improving the compressive strength. Additional factors were that on one hand, this was an era that reinforced concrete itself was still new and was developing simultaneously and furthermore, higher material cost and lack of theoretical knowledge of FRC made it less attractive. However, when at the beginning of 1960s, Romualdi, Batson and Mandel (Romualdi and Batson 1963, Romualdi and Mandel 1964) studied the fracture mechanisms design of FRC and published papers in this subject, it drew the attention of the industry in many developed countries and as time passed FRC became a subject of interest for many researchers around the world (Mondo 2011).

Committee 544 (2008) of the American Concrete Institute (ACI) defines fiber reinforced concrete as “concrete made primarily of hydraulic cements, aggregates, and discrete reinforcing fibers” and categorized it into four groups based on the fiber material: steel fiber reinforced concrete (SFRC), glass fiber reinforced concrete (GFRC), synthetic fiber reinforced concrete (SNFRC), and natural fiber reinforced concrete (NFRC). Natural fibers show vulnerability to environmental conditions, therefore leaving the steel and synthetic fibers as the most practical options for industrial applications. In the early twenties, glass fibers were mostly used in production of precast cladding materials, whereas steel fiber reinforced concrete was mostly used for defence-related construction. Since that time, however, many specifications have been developed by Codes paving the

way for the introduction of UHPC in construction such as the Canadian Highway Bridge Design Code and Annexes thereof (CHBDC 2006). In the context of UHPC, the usage of fibers has multiple advantages including, but not limited to:

- Fibers delay crack propagation by bridging the cracks thereby providing a mechanism of stress transfer that delays crack growth and prevents brittle failure.
- The “Confining Effect” exerted by fibers to the surrounding matrix also helps to reduce the rate of expansion and to prevent uncontrolled expansion in the direction of the tensile stress due to crack opening; this is exactly analogous to the mechanism of stirrups providing the confining lateral pressure in traditional concrete (Georgiou 2017).
- Fibers engage part of the mix water (for coating of their surface with at least a monolayer of water) inside the fresh concrete and are therefore very effective to control shrinkage cracking, reduce bleeding and segregation (Lawler et al. 2005).

Today, the state-of-the art is focused on self-consolidated Strain Hardening synthetic-Fiber-Reinforced Cementitious Composites (SHFRCC) with fine aggregates demonstrating great crack control and high ductility and improved durability performance. Most popular synthetic fibers are polyvinyl-alcohol (PVA) fibers, polypropylene (PP), ultra-high-molecular-weight polyethylene (PE-UHMW) and carbon-fibers (Figure 1.1) and hybridization resulting from mixes of various sizes and qualities of fibers. In the present investigation, the focus is in study of Strain Hardening Fiber Reinforced Cementitious Composites (SHFRCC) with use of polyvinyl-alcohol (PVA) fibers as mass reinforcement.

Due to a large number of free hydroxyls in the molecule structure of PVA fibers, they have hydrophilic surface which leads to creation of high chemical bonding with the surrounding cementitious matrix. If not controlled properly, the strong bond between fibers and the matrix leads to limited strain capacity due to brittle rupture of fibers. However, it has been shown that through proper surfactants it is possible to change the water binding capacity of the fibers, thereby altering the mode of failure from fiber rupture to fiber pull-out, which

then leads to a superior overall performance (multiple cracking behaviour, high ductility, and high strain capacity) (Georgiou 2017).

The objective of this study is to understand the behaviour of this material in shear and to evaluate its contribution to the mechanics of resistance of structural members. It is a goal of the research to evaluate the role of the fibers not only as a mechanism providing sustained web resistance to diagonal tension cracking but also the mechanism by which the fiber concrete protects the propagation of splitting cracks along bar anchorages which marks the final stage prior to failure of conventional concrete beams.

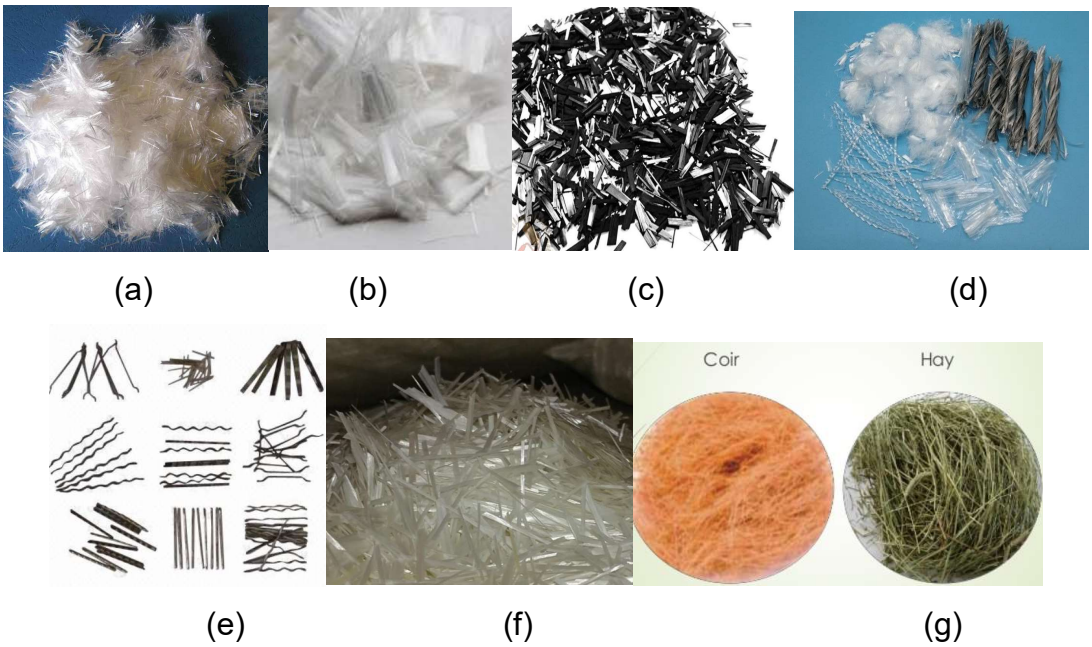

Figure 1.1: Various Types of Fibers (a) PP (b) PVA (c) Carbon (d) PE (e) Steel (f) Glass

(g) Natural (Adapted from https://mohandesbano.wordpress.com/)

Another way of categorizing FRC is to classify the various material types according to their mechanical performance in tension: two primary groups are listed in the literature, namely Strain Hardening and Strain Softening materials. These terms are meant to describe the response to direct tension, however, Strain Softening materials may exhibit a resilient behavior when tested indirectly to tension, such as for example in the case of flexural prism tests. Considering that tension tests are not straightforward to carry out,

and the tests in flexure are the main means of assessing the material's strain capacity under tension, this class of FRCs is classified further to deflection hardening and deflection softening materials as depicted in Figure 1.2 (Naaman and Reinhardt 2006).

The term High Performance Fiber Reinforced Cementitious Composites (HPFRCC) is attributed to FRCCs that show strain hardening behaviour along with multiple cracking and related large energy absorption capacity and tensile strength in the order of 10MPa or more (Naaman and Reinhardt 2003). Engineered Cementitious Composites (ECC) are High Performance Fiber Reinforced Cementitious Composites (HPFRCC) but unlike some HPFRCC they contain a relatively small fraction of synthetic fiber (generally PVA at 2% or less) (Li and Kanda 1998). ECC typically has a sustained tensile strength of 4-6 MPa and tensile strain capacity of 2-5% (Li 2003).

To secure a large tensile capacity, the phenomenon known as crack stabilization should be delayed or avoided, to enable the formation of multiple cracks under constant stress (rather than a single localized crack) so that greater ductility may be observed. The most recent stage in the development of ECC is use of short discontinuous fibers in self-consolidating fine aggregate cementitious mixes. Based on the specific mechanical properties of each type of fiber and their binding with surrounding matrix, different final product's characteristics are expected and may be designed for. Here in this research, the focus is on evaluation of the behaviour of polyvinyl- alcohol (PVA) strain hardening fiber reinforced cementitious composites (PVA-SHFRCC).

Being also motivated by the emerging concerns for environmentally sustainable development, in the advancement of SHFRCC technology, a high volume of fly ash (more than 60% of cement replacement) is used for binding. Usage of High Volume Fly Ash (HVFA) would improve both the fresh mix state and the hardened mix properties of FRCC in terms of higher workability, larger strain capacity, improved ductility, negligible permeability and higher durability (Ferraris et al. 2001, Thomas 2007, Georgiou 2017).

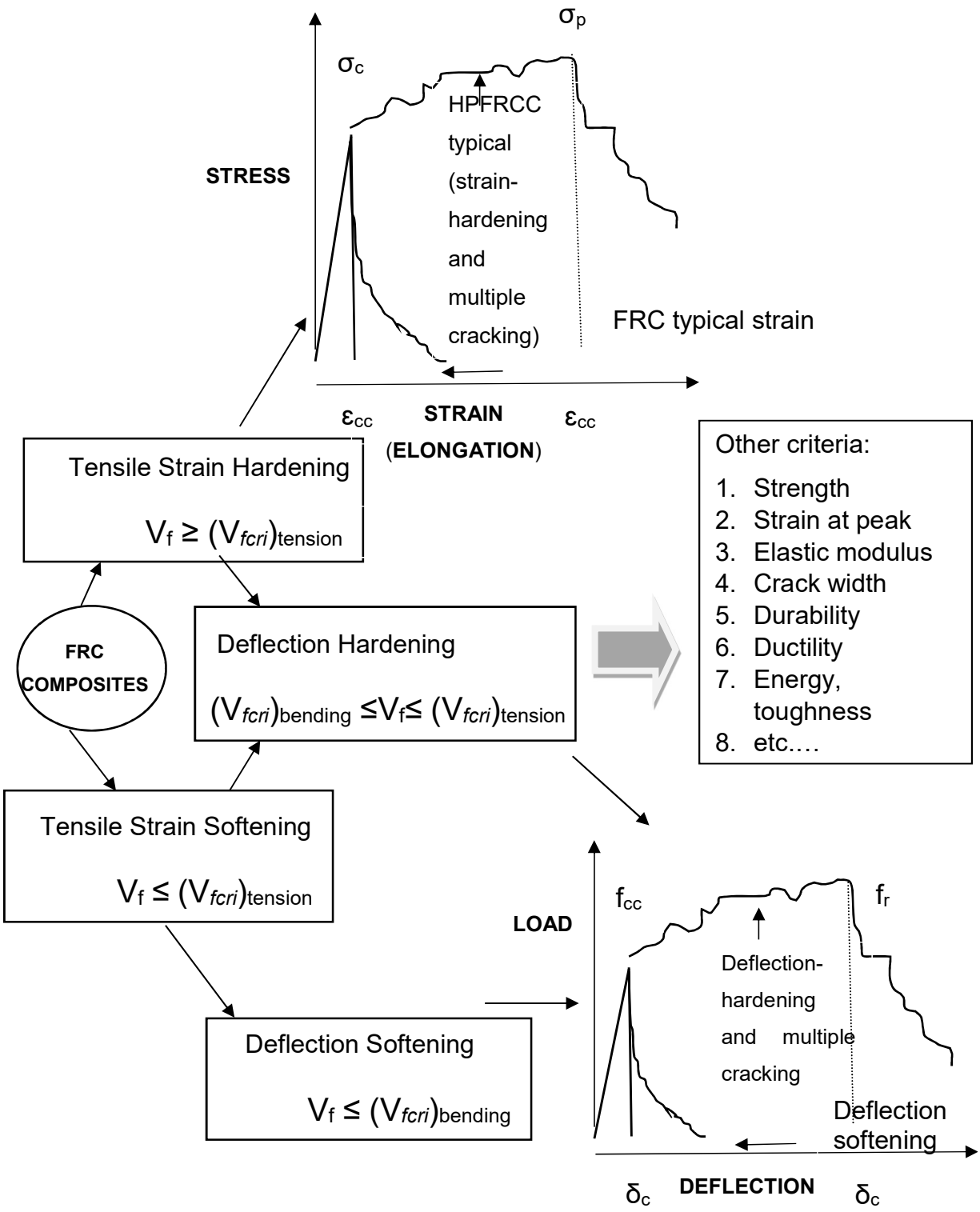

Figure 1.2: Classification of FRC composites based on their tensile stress-strain response (Naaman and Reinhardt 2006)

1.2 Scope of the Thesis

While in normal concrete the contribution of concrete in tension is neglected in all established design procedures, in the case of SHFRCC, promising results have been published indicating the efficiency of fibers in bridging the cracks and showing post cracking resilience and remarkable tensile deformation capacity (Li and Kanda 1998, Li 2003, Paegle and Fischer 2012, Georgiou and Pantazopoulou 2016). There is a great possibility of the substituting bar-type shear reinforcement with this new type of material and therefore there is a need to quantify the strength of this material in shear and flexure.

The focus of this thesis is on investigation of the shear and flexural strength of Strain Hardening Fiber Reinforced Cementitious Composites (SHFRCC) and the implications this has on the structural response of whole members. This thesis includes both analytical and experimental components and has three designed main thrusts:

1. Analytical investigation of shear in order to identify the inter-relationship of bond and development capacity of primary reinforcement on the shear strength of concrete structural members.
2. Establish, test and fabricate Strain Hardening Fiber Reinforced Cementitious Composites (SHFRCC) with local non-proprietary materials as an easily accessible, feasible, state-of-the-art solution for achieving improved concrete mechanical properties.
3. Illustrate the concepts developed regarding the mechanistic behavior of SHFRCC material in shear and support the analytical developments through pertinent experimental evidence.

Regarding the analytical component of the research, the objective is to formulate and support through corroboration with the experimental literature a theoretical interpretation of concrete contribution in shear strength of structural members. This investigation was motivated by previous attempts to quantify the shear strength contribution of concrete to the shear strength of members: as is evident from the literature, significant effort has been vested over the years in quantifying this term, mostly supported and corroborated by experiments on beams containing longitudinal reinforcement without stirrups. In fact the

literature has been absorbed with the effect of size in the estimation of shear strength component, as there has been experimental evidence that with increasing size of specimens the shear strength contribution is deprecated (Reineck et al. 2003). On close examination of this evidence and the appearance of the tests it seems that bar size, the most significant measure of specimen size, has not been considered in the study, whereas the last stages of shear specimens in the database invariably illustrate bond failure. Thus, by the introduction of novel cementitious materials in construction, which have already been shown to be favorable in terms of bond strength of embedded bars, it is expected that improved shear strength may occur as they are likely to preclude the bond-failure stage that marks the end of shear strength in concrete.

Furthermore, with the development and introduction of ductile materials in civil engineering works, emerges the practical need to develop design standards for construction of structural members. In this context, shear lies at the forefront of open issues in structural concrete design and remains the same in the case of FRCC. Here in this research, an alternative framework of analysis to interpret the shear failure and the corresponding strength of the failure mechanism is suggested which gives an insight into a totally new interpretation of shear failure and relates to the state of bond of reinforcement over the entire span of a loaded member. This approach is adaptable and may be used to establish a design framework for new concrete materials such as SHFRCC.

While the increase in shear strength of Fiber Reinforced Cementitious Composites (FRCC) is well recognized in today's research community, there is an outstanding need to corroborate this claim by further investigation of the behaviour of this new material under the main states of stress in structural members and incorporate these materials in modern codes of practice. The major problems in the field of shear are the limited experimental data regarding the functionality of SHFRCC in shear/flexure and a lack of a systematic theory for the shear strength of SHFRCC. In fact, the concern is that the real variables that cause the shear failure have not been understood yet. Evidently several of the parameters that affect the concrete-reinforcement interaction, such as bar size, cover, and development length, have been neglected in the emerging shear strength proposals.

Since the documented test evidence regarding the performance of strain hardening fiber reinforced cementitious composites (SHFRCC) when used in structural members is still limited, and it being considered a recent advent in concrete materials technology, there is a lack of design expressions for this kind of material and therefore in this study an experimental program is designed to provide a basis for development of design rules which are prerequisite for introduction of these novel materials in new construction. The first part of the experimental program is dedicated to study of shear in SHFRCC and investigation of any possible size effect in SHFRCC using push-off specimens. The second part of the experiment and analysis focuses on the behaviour of SHFRCC in combined shear and flexure in concrete beams. All experiments are conducted in the Structural Lab of Lassonde School of Engineering, York University.

1.3 Organization of the Thesis

In this thesis, the attempt is to contribute towards the overall understanding of shear failure in structural members and specifically shear in the case of novel materials such as the synthetic Strain Hardening Fiber Reinforced Cementitious Composites (SHFRCC), with the ultimate goal of identifying the true mechanism behind shear failure and encouraging the widespread use of this novel material. The background of Fiber Reinforced Concrete and brief introduction and overview of this master thesis' research project is presented in Chapter 1.

The detailed review of the state of the art concerning the three main thrusts of the thesis, namely, (a) one-way shear strength in concrete structural members, (b) Strain Hardening Fiber Reinforced Cementitious Composites (SHFRCC) with PVA fibers and high volume of fly ash as cement replacement, and (c) the scope of the available experimental investigations with this type of material, is discussed in Chapter 2.

Chapter 3 points out the importance of shear strength and the challenges presented to its quantification. Several different alternatives from among the current "shear proposals" are used to calculate shear strength of concrete beams without shear reinforcement (from the ACI database).

Chapter 4 presents an analytical formulation to provide an alternative interpretation for shear failure, where the catastrophic effect of strain penetration on shear resistance is illustrated through mechanics. Two sample cases from ACI database are included for illustration of concepts and application of the analytical procedures (Eshghi and Pantazopoulou 2018). The performance of the basic shear-contribution proposals is also presented for comparison.

In Chapter 5, the experimental program which was conducted during the preliminary and subsequently in the main phase of the study is described in detail. In the preliminary phase of the experimental program, the development of Strain Hardening Fiber Reinforced Cementitious Composites (SHFRCC) in the lab using local materials without proprietary ingredients was pursued through the studying of the effect of different mix variables (size of sand, presence of silica fume and slag, and coating of PVA fibers); several mix designs were carried out in small trials, followed by testing small-scale specimens to proof test the design concepts of each mix. Four-point bending, and compression tests were conducted on prisms and cubes or cylinder specimens. In the main phase, compression, four-point bending of unreinforced prism and reinforced beams, and shear push-off tests were conducted. Test specimen's dimensions, test set-ups, testing equipment's, and the testing procedures are discussed in detail.

In Chapter 6, the results of both phases of the experiments are described extensively. The details of the test observations and digital image correlation (DIC) analysis are used to interpret the performance of each specimen and the essential characteristic constitutive models (Mohr-Coulomb failure envelope, material size effects) are calibrated and presented.

In Chapter 7, a review of the existing shear design provisions for SHFRCC in various studies, codes and standards is presented. Furthermore, a database of collected experiments on PVA-FRCC beams under flexure and shear is assembled and the state of the art regarding the estimation of shear strength of SHFRCC materials is reviewed. The detail of experimental setups and specimen dimensions and characteristics are also included in the database input. The presentation is followed by comparison of the

experimental values with calculated shear strengths of these specimens based on several different existing codes and recommendations for UHPC.

Finally, the conclusions of the study along with recommendations for continuation of the research work are summarized in Chapter 8.

CHAPTER 2: LITERATURE REVIEW

2.1 Introduction

The purpose of this chapter is to review the state of the art and to provide context for the open issues addressed in this thesis: a) The influence of strain penetration and bond on the shear strength of concrete structural members without stirrups, b) Strain Hardening Fiber Reinforced Cementitious Composites (SHFRCC) as a state-of-the-art solution for improving concrete mechanical properties, particularly shear strength and strain penetration resistance, c) Experimental investigation of the performance of SHFRCC structural members in shear. In this way, we hope this thesis can materially contribute to the development of design provisions for the structural use of SHFRCC.

2.2 Literature Review on Shear

2.2.1 The Shear Strength of RC Structural Members without Stirrups

Plain concrete is well known to be brittle in tension and to rely on bar-type reinforcements to resist tensile stresses after cracking. The first patent of reinforced concrete goes back to the second half of 19th century when Joseph Monier, a Parisian gardener, used a metal cage to shape his flower pots and realized this would strengthen the concrete in tension. And in 1847, another Frenchman, Joseph-Luis Lambot, built a boat with metal structure covered with concrete, and it was filed as a patent (Hasse 1989). The study of concrete in shear, in particular, goes back to the end of 19th century when Ritter (1899) presented Hennebique's construction method that was patented in 1985 and 1987 in Switzerland and pioneered the use of stirrups for shear resistance. As early as the late 1800's Ritter (1899) and Mörsch (1909) proposed a simple 45^{o} truss system to interpret the behavior of Reinforced Concrete (R.C.) beams in shear after cracking initiation. They postulated that owing to the arrangement of diagonal tension cracking at the midweb of beams (see right side of Figure 2.1), diagonal struts form in an idealized truss oriented as shown in the left side of Figure 2.1.

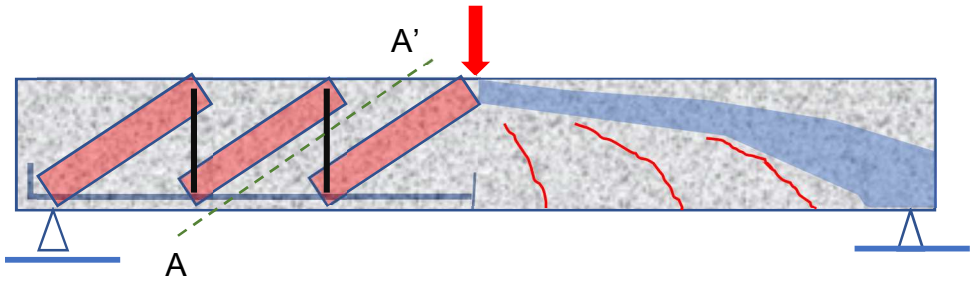

Figure 2.1: A 45° truss proposed by Ritter (1899) and Mörsch (1909) to explain shear behavior in cracked RC members.

From Free Body Equilibrium to the left of cut A-A' shown in Figure 2.1, it follows that shear strength is equal to the yield strength of the vertical tie in the truss, known henceforth as the steel contribution, V_s. This model was used for several decades as the basic tool for shear design. However, when the estimations of the model were compared with experimental results a discrepancy was observed, with the experimental results consistently exceeding the truss strength. This discrepancy was attributed to what was thought to be a secondary contribution, originating from the concrete; sources of the concrete contribution, V_c, have been attributed to (a) the compressive force that develops in the compression zone of the beam which follows an inclined trajectory in the shear span from the position of peak moment to the support, as depicted in the right-hand side of Figure 2.1, (b) Interlocking of aggregates along the crack surfaces depicted in the same region of the figure by the red lines, and (c) by dowel action of the longitudinal reinforcement crossing the cracks and supported by the cover (MacGregor et al. 1997). These terms were meant to be a correction over the original truss value, so that the strength of Reinforced Concrete (RC) beams in shear would comprise the sum of the two contributions: $V = V_c + V_s$. Alternative interpretations were also offered to account for the differences between tests and experiments such as the multiple truss model (Mörsch 1909), whereas Kupfer proposed a variable strut inclination model (Kupfer 1964). In other attempts the angle of the truss was reduced from the 45° value (for example, the current Eurocode 2 allows design to be carried out with a 22.5° truss analogy (Eurocode 2 2004)).

Since its introduction as a concept, the concrete contribution term has challenged researchers because no apparent expression could be established to model well the

experimental trends. Already from the 1960's Kani conducted an extensive experimental campaign on beams of variable sizes at the University of Toronto and found that the V_c term did not follow consistently the experimental trends, particularly with regards to larger size specimens (Kani 1967). As a remedy Kani offered the interpretation of the comb-like mechanism to explain the mechanics of shear in reinforced beams after cracking (Kani 1964), however this approach was never endorsed by the design codes that seemed to adhere to the truss modelling approach. In fact, and because the truss model estimates fell short to the experimental values, the emphasis of codes has been in quantifying this difference – which became known as «the riddle of shear» among connoisseurs (ACI 318-71, 83, 08, Eurocode 2 2004)

As research in shear intensified (Figure 2.2) many aspects and open issues gained further attention: For example, Leonhardt identified the upper limit of shear resistance in the web of beams associated with compression crushing (Leonhardt 1964) which later was introduced as an essential check in design (e.g. in the CSA Code the factored shear resistance (V_r) is required to be less than $V_{r,max} = 0.25\ \phi_c\ f_c' b_w d_v$ on account of avoiding catastrophic strut failure (CSA-23.3-14)). The effect of prestressing on shear strength of beams was studied by Thürlimann et al. (1978) and Warlaven and Mercks (1983), whereas with the advent of Finite Element models Darwin and Pecknold (1977) first and later Vecchio and Collins (1986) formulated a model based on continuum mechanics considering concrete as an orthotropic material in perfect average compatibility with the smeared reinforcement to represent the relationship of average stress and average strain in the general state of stress of a plane concrete panel. Vecchio and Collins's framework also included several important attributes that secured better calibration of the analytical with the experimental results such as a compression softening coefficient that attenuates concrete compressive strength with increasing transverse strain, a local equilibrium check at the cracks, and an indirect account of bond as a tension stiffening phenomenon in the vicinity of the reinforcement. This formulation became known as the Modified Compression Field Theory (MCFT) and has since contributed significantly to improved understanding of the behavior of reinforced concrete under shear stress (Vecchio and Collins 1986).

The reason why this intensive activity spanning over more than 100 years has been dedicated to shear is because still, many aspects of the problem seemed to be poorly understood, particularly when mechanistic estimates were contrasted with the experimental evidence (MacGregor et al. 1997). Despite the intensive work done on the topic of shear, two trends prevailed and transcended the design procedures for shear practically used throughout most of the world:

(a) That shear strength of Reinforced Concrete members in the absence of stirrups was reduced to the concrete contribution. This could no longer be treated as “a correction” since it is accounted for the entire resistance of the member.

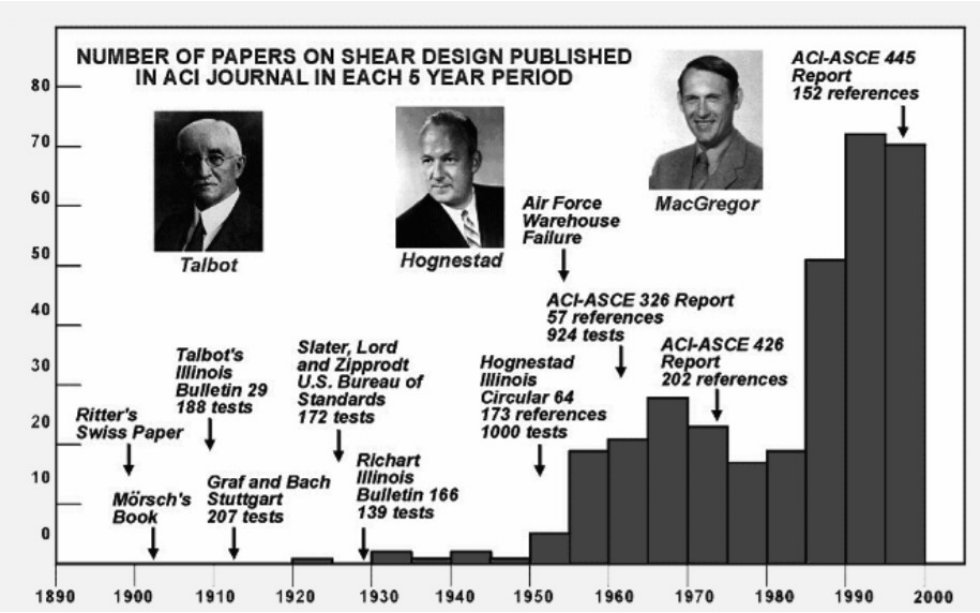

Figure 2.2: Number of papers published on shear design in ACI Journal since the beginning of the last Century (Collins et al. 1996)

(b) That the V_c term was rather poorly understood as evidenced from occasional failures that could not be predicted by the existing models, and by the fact that the level of uncertainty and inaccuracy seemed to increase with the size of the members (Air Force warehouse failures in 1955 and 1956 Ohio, USA (Feld and Carper 1997)). In fact it was found that the V_c term did not increase proportionately with the depth of the member as

the code equations would suggest, leading to unsafe designs in larger structures (Collins and Kuchma 1999).

This brought about the need for the development of databases of similar tests conducted by many investigators from around the world (Reineck et al. 2003) which are used extensively even today to prove or disprove concepts for the various expressions that are advanced to account for the shear strength of R.C. members. Several alternative interpretations for the size effect in shear have been pursued: For example Bazant (2001) postulated that the size effect is due to the limited fracture energy of concrete which is released upon the formation of a single crack (a property of concrete measured in N/m) which does not scale up proportionately with stress (a function of m^{-2}) when going from smaller structures to larger size ones; Frosch et al. (2017) suggested that the size effect is better organized when the compression zone depth, c, rather than the whole section depth, d, is considered active in supporting the V_c.

2.2.2 The Database of Beam Tests with No Stirrups

The size effect flaw was clearly a result of the small size beams tested in the laboratories in order to support calibration of design expressions against the experimental results. This is why in recent years significant effort has been invested (a) in conducting shear tests on larger size experiments, (b) in organizing the supporting databases in subgroups of specimens according to their size range (Reineck et al. 2003) and recalibrating the design expressions to account for that effect. The database has been used already in the past to refine a variety of empirical design expressions and models for V_c. For example, Reineck et al. (2003) used the database to assess the ACI 318-14 design expression for V_c, while developing "a *sanctioned set of criteria"* to accept a test result into an "evaluation level shear databank" (ESDB). They concluded that the ACI 318-14 provisions for shear strength of beams without stirrups becomes increasingly unsafe "as members become larger and more lightly reinforced." In their assessment, they used 11 different "control or elimination criteria (KONi)", as described in Table 2.1, to accept a test result into the database.

In recent decades, significant effort by the ACI community has been invested in addressing this unsatisfactory state of affairs regarding the “riddle of shear” which has been going on for at least 40 years. After an initiative by ACI-ASCE Committee 445 (referred to hereon as C445), proposals were solicited for possible design expressions for V_c, which have been placed under scrutiny against experimental data from beams comprising conventional concrete and no transverse reinforcement (Belarbi et al. 2017).

Table 2.1: Individual selection Criteria KONi for ESDB (Adapted from Reineck et al. (2003))

Criteria	**Description of individual criterion**	
	Description	**Formula**
KON1	Concrete compression strength	$f_{1c} = 0.95 f_{c,cyl} > 12MPa$
KON2	Upper limit of compression strength	$f_{1c} < 100Mpa$
KON3	Width of cross section	$b > 50mm$
KON4	Height of cross section	$h > 70mm$
KON5	Shear span ratio	$^{a}/_{d} > 2.9$
KON6	Lower limit of shear span ratio	$2.4 < {}^{a}/_{d} < 2.89$
KON7	Longitudinal reinforcement ratio	$\rho \leq 0.03$
KON8	Compression zone height at failure	$\omega_l \beta_{flex} < 0.4$
KON9	Flexural failure	$\beta_{flex} = {}^{M_{u,test}}/_{M_{u,cal}} < 1$
KON91	Double checking for failure mode	$1 < \beta_{flex} < 1.1$
KON10	Ribbed bar	-
KON11	Anchorage failure	$\beta_{lb} = {}^{l_{b,req}}/_{l_{b,prov}} < 1$

Table 2.2: Notation used in Table 2.1

f_{1c}	Uniaxial strength of a slender prism
$f_{c,cyl}$	Cylinder strength
b	Cross section width
h	Cross section height
a	Shear span
d	Effective depth of cross section
ρ	Longitudinal reinforcement ratio
ω_l	Mechanical longitudinal reinforcement ratio
$M_{u,test}$	Experimental maximum moment
$M_{u,cal}$	Calculated maximum moment (based on reinforcement yielding)
$l_{b,req}$	Required anchorage length
$l_{b,cal}$	Calculated anchorage length

The carefully controlled database of hundreds of concrete beam tests set up 20 years ago was called into use on the occasion of this re-fueled attempt (Belarbi et al. 2017). In the present competition the acceptance criterion was the ability of the design model to reproduce the experimental sensitivities over the entire range of the experimental parameters. Beams with flexural or anchorage failure were omitted from the database according with the following limiting requirements:

- KON9: Assessment of Flexural Failure

Ignoring the compression reinforcement, the height of the compression zone, x, with a uniform compressive stress block and the sectional flexural capacity, $M_{u,cal}$, were calculated as:

$$x = {\omega_l}/{\kappa_c}\, d$$ (is also denoted by *c* in some reference studies) (2. 1)

$$\omega_l = \rho\, {f_y}/{f_{1c}}$$ (2. 2)

$$\rho = {A_s}/{bd}$$ (2. 3)

$$\kappa_c = (1 - {f_{1c}}/{250})$$ (2. 4)

$$z = (d - 0.5x)$$ (internal moment lever arm) (2. 5)

$$M_{u,cal} = A_s f_y z$$ (2. 6)

$$\beta_{flex} = {M_{u,test}}/{M_{u,cal}} < 1$$ (2. 7)

- KON11: Assessment of Anchorage Failure

The support plate dimensions (a_A), the beam overhang beyond the end supports of the beams (b_A), and concrete cover ($h - d$) (as shown in Figure 2.3) are needed to calculate the provided anchorage length:

$$l_{b,prov} = [b_A + 0.5a_A - (h - d)]$$ (2. 8)

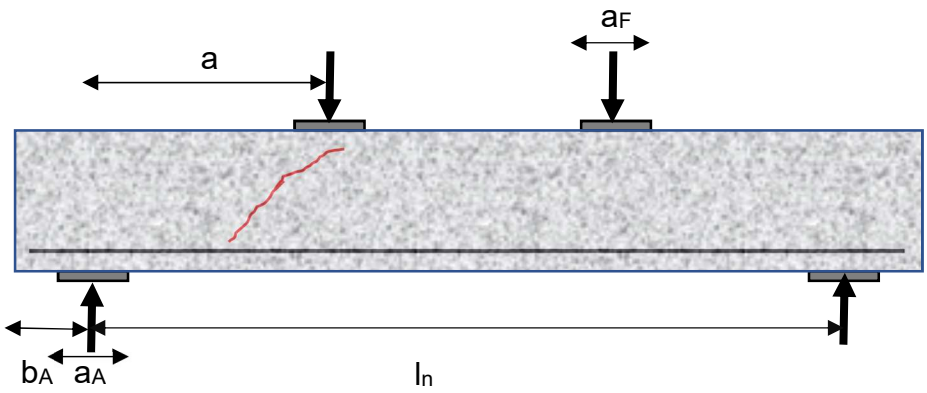

Figure 2.3: Typical beam dimensions and test set up

In case of insufficient information, the provided anchorage length was calculated as follows:

If a_A was not known: $l_{b,prov} = b_A$

If b_A was not known: $l_{b,prov} = a_A + 0.1d$

If a_A and b_A were not known: $l_{b,prov} = 0.25d$

And $l_{b,cal}$ was calculated as follows while the assumed bond stress was based on the FIP Recommendations (1999), i.e., $f_b = 1.5f_{1ct,cal}$ at failure.

$$l_{b,prov} = \alpha_a {d_{st}F_{sA}}/{9A_s f_{1ctm,cal}} \quad (2.9)$$

Table 2.3: Notations used in Equation (2.9)

$\boldsymbol{\alpha_a}$	1 for straight bars 0.7 for hooked bars 0.01 for anchor plates
$\boldsymbol{d_{st}}$	Average diameter of longitudinal tension reinforcement
$\boldsymbol{f_{1ctm,cal}}$	Calculated axial tensile strength

$$f_{1ctm,cal} = 1.15\,(f_{c,cyl} - 4)^{1/3} \quad (2.10)$$

F_{SA}, the tension force in the longitudinal reinforcement at the end support at ultimate load, was determined from the truss model presented by Reineck (1990, 1991):

$$F_{sA} = V_u[{0.5a_A}/{Z} + {1.73d_b}/{Z} + 0.58] \quad (2.11)$$

$$\beta_{lb} = {l_{b,req}}/{l_{b,prov}} < 1 \quad (2.12)$$

It is noteworthy that the study mentions that checking the KON11 is not enough to preclude anchorage failure, and rightly so as the anchorage is known to exhibit “unzipping” failure in the absence of confinement (i.e., precipitous splitting due to cover cracking and bond failure, Darwin at al. 2001).

Table 2.4: Notation used in Equation (2.11)

$\boldsymbol{V_u}$	Ultimate shear force
$\boldsymbol{a_A}$	Support plate dimensions
$\boldsymbol{z}$	Inner lever arm ($z = d.\zeta$)
$\boldsymbol{\zeta}$	Coefficient for inner lever arm ($\zeta = 1 - 0.5\,{}^{\omega_1}/_{\kappa_c}$)
$\boldsymbol{\omega_1}$	Mechanical reinforcement ratio of tension chord ($\omega_1 = {}^{\rho_1 f_{sy}}/_{100 f_{1c}}$)
$\boldsymbol{\kappa_c}$	Coefficient for maximum stress of stress block over full depth ($\kappa_c = 1 - {}^{f_{1c}}/_{250}$)
$\boldsymbol{d_b}$	Longitudinal reinforcement bar diameter

2.2.3 The Effectiveness of the Proposals for V_c

In embarking on the calibration of the V_c proposals with the database it was already established that whereas the empirical models for shear performed adequately when used for beams having similar sizes as those used for model calibration, deviations persisted between calibrated models and test results outside the range of parameters studied, the most dramatic being a systematic overestimation of beam strengths with larger than common size. The effect of size has been at the centre of the shear controversy for years (Kani 1967, Ozbolt and Eligehausen 1995, Collins and Kuchma 1999b, Bažant 1999, Karihaloo et al. 2003, Cladera and Marí 2004, Grégoire and Laboratoire 2013, Kirane et al. 2016, Belarbi et al. 2017). However, there is still great uncertainty about the role of the crucial variables affecting V_c. Experiments indicate that the shear strength of concrete members does not increase proportionately with the bearing (web) area, $b_w d$ – but that instead, there is an implicit size-effect in V_c that is owing to fracture mechanics considerations (Bazant and Planas 1997) and the larger aggregate size used in real life members as compared to the specimens tested in laboratories (Collins and Kuchma 1999b).

In fact, simple comparison between the experimental values for shear strengths of beams without any stirrups (V_{test}) in the database with the values calculated as per ACI 318-14 (V_{ACI}) demonstrates significant scatter particularly in the case of larger members (Figure

2.4). This underscores the fact that the true mechanism behind the shear failure is not completely understood and there might be important aspects that are overlooked in the established models. Revisiting this problem is one more attempt by C445 to correct the discrepancies between test results and design expressions. The proposals submitted for V_c are examined against the experimental trends in Chapter 3. Litmus test for acceptance of any proposal was its performance against the ACI database.

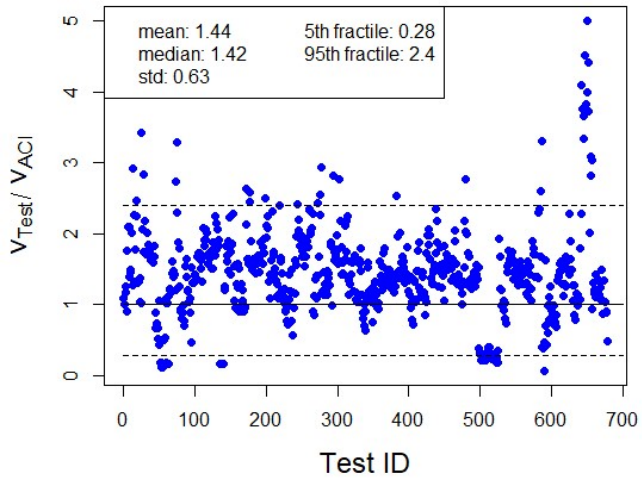

Figure 2.4: (a) Measured V_c value normalized with respect to V_{ACI};

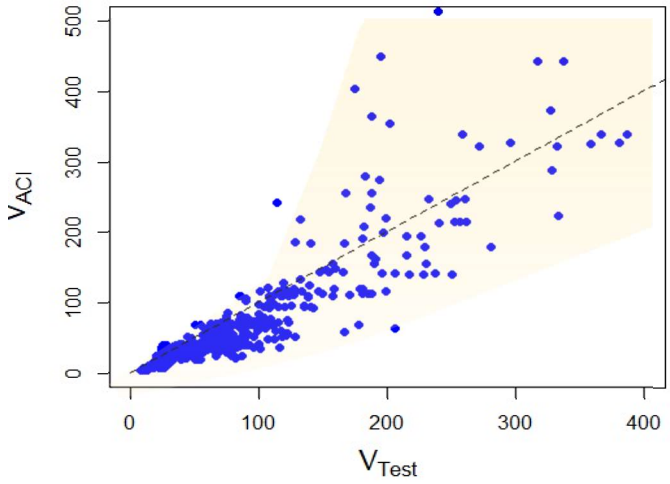

Figure 2.4 (b) V_c plotted against V_{ACI}: note that the discrepancy increases in the range of larger forces measured (i.e. in larger beams)

2.3 Literature Review on Strain Hardening Fiber Reinforced Cementitious Composite (SHFRCC)

2.3.1 Motivation and Background

One way to test the validity of the assumption regarding the interaction of strain penetration with shear strength in beams after bond failure, is to actually study the performance in the presence of a mechanism that significantly enhances bond action along the longitudinal reinforcement. To achieve that without the addition of stirrups is by means of using Fiber Reinforced Concrete (FRC) in the region over the anchorage. In addition, Fiber Reinforced Cementitious Composites (FRCC) as an emerging technology cannot eventually find their way in construction unless their resistance to shear is addressed. Previous studies have provided a limited number of experimental data, however due to the great variety of mixes, fiber types and test setups available in the literature, the conclusions that can be supported thus far are limited and qualitative only.

Understanding the two motivating issues stated above led to the extension of the thesis to the exploration of shear in FRCC steel-reinforced beams without stirrups; in this regard a number of challenges had to be resolved in order for the experimental program to be feasible. These included the ability to reproduce a strain – resilient material in the experimental facility at York University, using non-proprietary ingredients. It was also desirable that the material would be close to other alternatives that have been tested before considering a variety of stress states (e.g. anchorages, see Georgiou 2017).

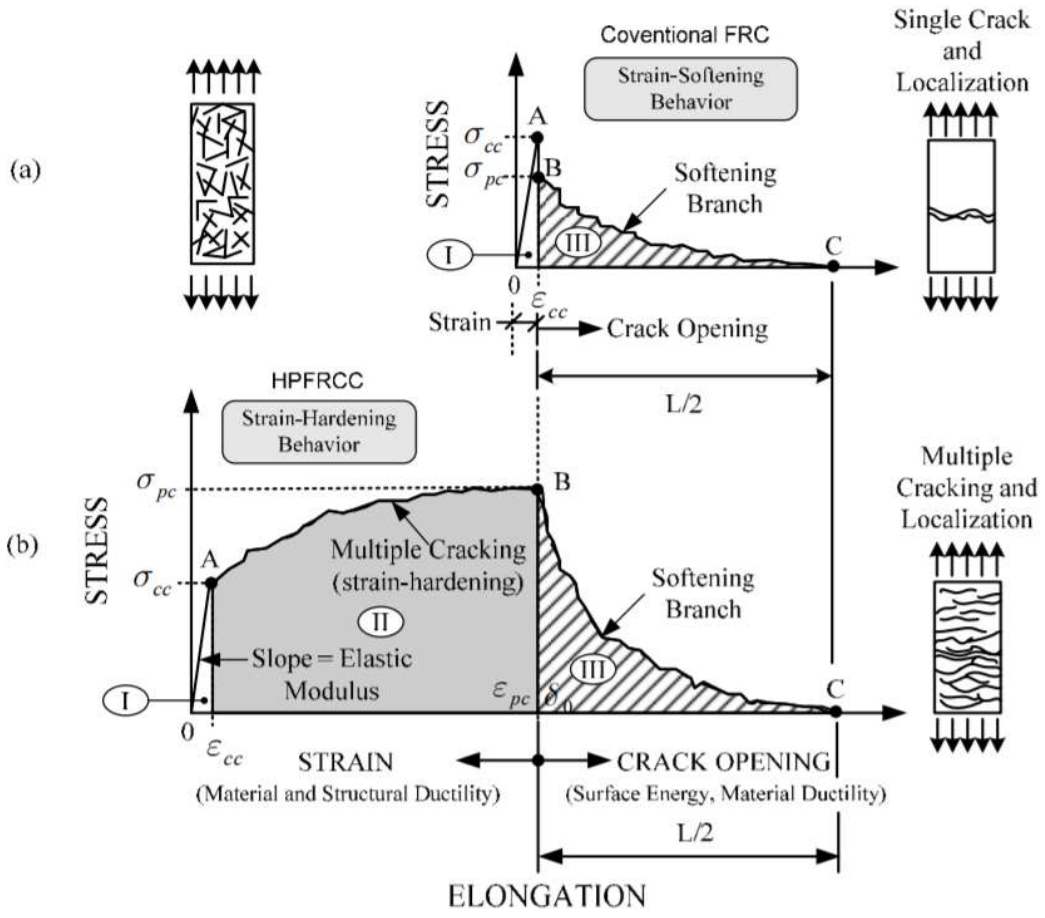

Figure 2.5: Typical stress-strain or elongation curve in tension up to complete separation: (a) Conventional strain-softening FRC composite; (b) Strain-hardening FRC composite or HPFRCC (from Naaman 2007)

In the present section the evolution of material technology that led to the development of FRCC as we know it today is outlined briefly. It was stated earlier that materials that fall under the general family of FRCC may be either strain softening or strain hardening in direct tension (Figure 2.5); the latter being further classified according to their response in flexure (Naaman 2007). The first effort to develop strain hardening composites begun in 1978 (Kasparkiewicsz 1978), however, this technology is still relatively new and has not yet fully grown. The progress of Fiber Reinforced Cementitious material in terms of their fundamental behaviour in tension and their terminology evaluation over four decades is summarized in Figure 2.6.

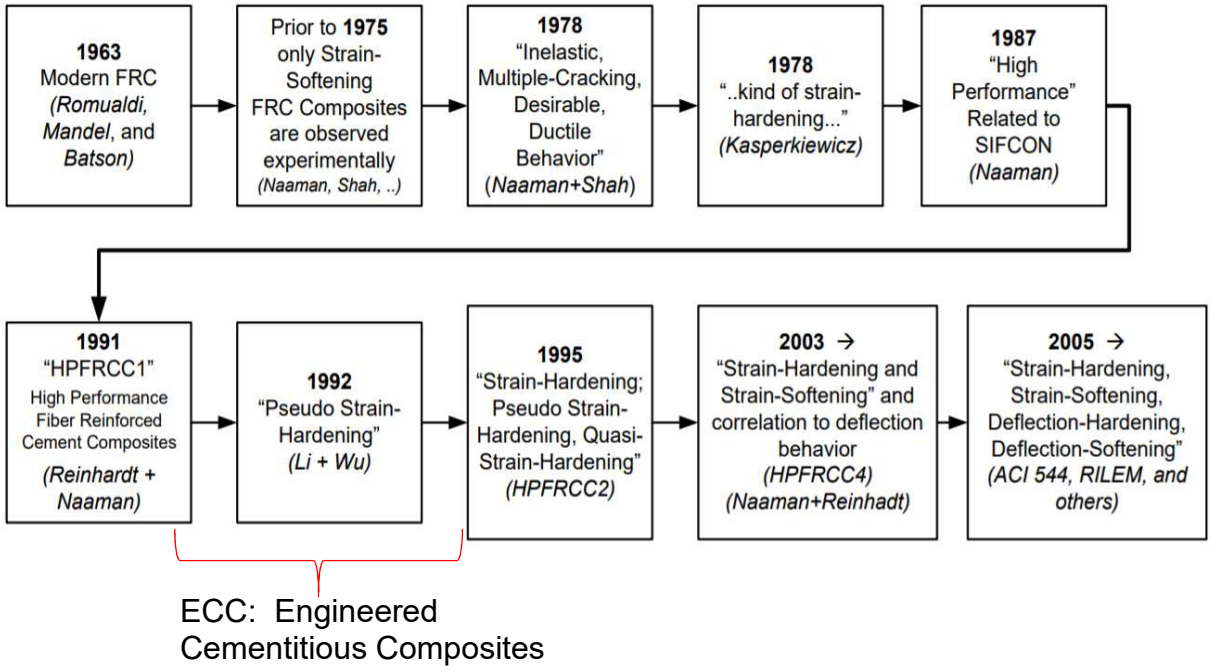

Figure 2.6: Evolution of terminology to describe strain-hardening behavior in tension, since the development of modern theories of FRC (Naaman 2018)

2.3.2 Strain Hardening Fiber Reinforced Cementitious Composites (SHFRCC)

One of the potential aspects of Fiber Reinforced Cementitious Composite (FRCC) development is strain resilience under tension while the material sustains adequate tensile strength. The requirement of having large strain capacity is to delay or completely avoid crack stabilization – note that this is the stage when by further increasing the applied load no new crack would form but the existing cracks would widen (MacGregor et al. 1997). In order to satisfy this requirement, multiple cracking behaviour is needed. "Strain Hardening" is the term to describe the strain resilient materials that sustain and increase their tensile strength up to large deformations by formation of very closely spaced parallel fine cracks. In fact, achieving a very fine crack spacing is key to the material's tensile resilience. This depends to a great extent on the type and intensity of binding between the fibers and the surrounding matrix, a property known as "specific bond" (Georgiou 2017).

Every fiber type is designed to exhibit a different specific bond strength: In general, metallic fibers with twisted profiles or anchors develop excessive bond strength and are prevented from adequate slip that would enable the strain hardening property. FRC's with this type of fiber do not generally exhibit (if at all) significant strain hardening capacity. Brass coating is used on fibers intended for UHPC as they seem to effect an optimal interfacial property. Synthetic fibers such as polypropylene are hydrophobic and therefore have negligible interaction with the surrounding cementitious matrix and for this reason the response of the PP-reinforced composite shows great tendency for localization of strain and wide crack formation. Polyvinyl-Alcohol fibers as well as natural fibers are on the opposite end of the spectrum, because they have a large number of free hydroxyls on their surface (Figure 2.7) which makes the surface hydrophilic and causes high chemical bonding with the surrounding matrix (cement hydrates). In general, stronger bond between PVA fibers and surrounding matrix results in lower tensile strain capacities (0.5-1%) (Li et al. 2002). As fibers are pulled out, a progressive damage occurs at the rupture ends of uncoated PVA fibers which is known called "Shear Delamination Failure" leading to sharp tips with a sudden load drop (stage 3 in Figure 2.8) (Li et al. 2002). As PVA fibers are pulled out, strong slip-hardening response would cause the shear delamination failure (Redon et al. 2001).

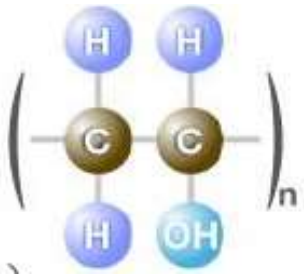

Figure 2.7: Chemical formula of PVA fibers

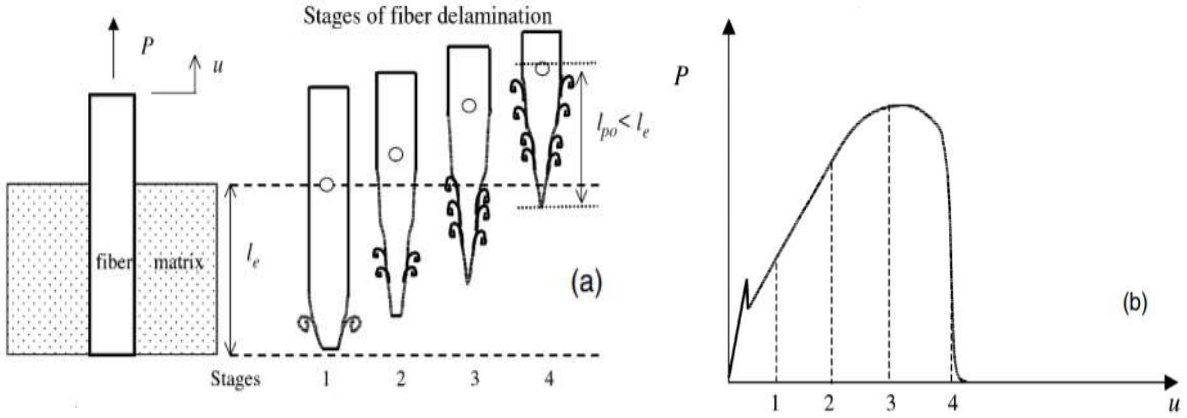

Figure 2.8: (a) Fiber delamination during slip-hardening; and (b) at various stages of pullout process illustrated on P-u curve (Li et al. 2002)

As a remedy to this experimental finding, Li et al. (2002) experimented with various coatings/surfactants in order to control the interfacial bond. In these cases, it was possible to eliminate failure by delamination. Failure by pullout with slight damage was seen when treated fibers were introduced in the cementitious mix (Figure 2.9).

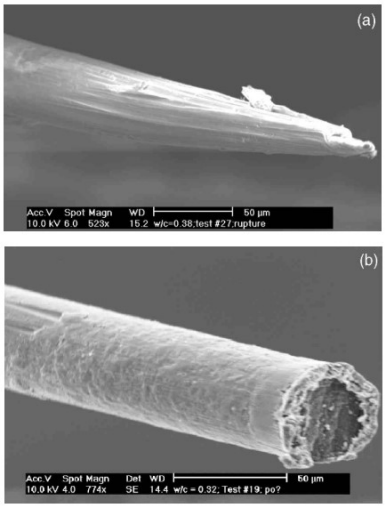

Figure 2.9: Effect of surfactant on delamination of PVA fiber: (a) Ruptured end of non-treated fiber; and (b) pulled out end of treated fiber (Li et al. 2002)

In the study conducted by (Li 2011), single fiber pull-out tests revealed that frictional and chemical bonds are attenuated by increasing the surfactant content (Figure 2.10). Furthermore, dog-bone tensile tests showed that tension strain capacity was increased from 1% for case where uncoated PVA fibers had been used, to more than 5% when 1.2% per weight of fibers treating agents were used to oil the fibers (Figure 2.11).

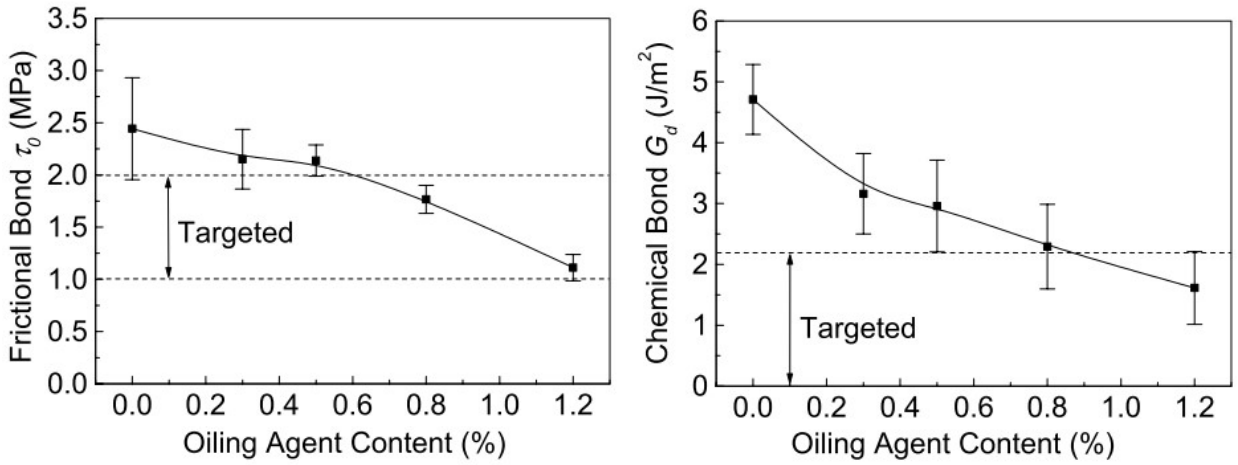

Figure 2.10: Measured (a) frictional bond, τ_0 and (b) Chemical bond G_d as a function of oiling content (Li 2011)

Coating of fibers as a way to moderate and control the specific bond, suggested initially by Lepech and Li (2006), was also tested and used by Georgiou et al (2014). The relevant technical aspects will be discussed in detail in Chapter 3. The driving objective in that study was, that bond between fibers and surrounding matrix (frictional resistance and chemical bond) should be controlled in a way that it should not be too strong to cause brittle failure and rupturing of fibers, nor should it be so weak as to lead to localized crack opening and extensive pullout of the fibers, in light of the fact that this type of behavior would seriously compromise the structural stiffness of the material.

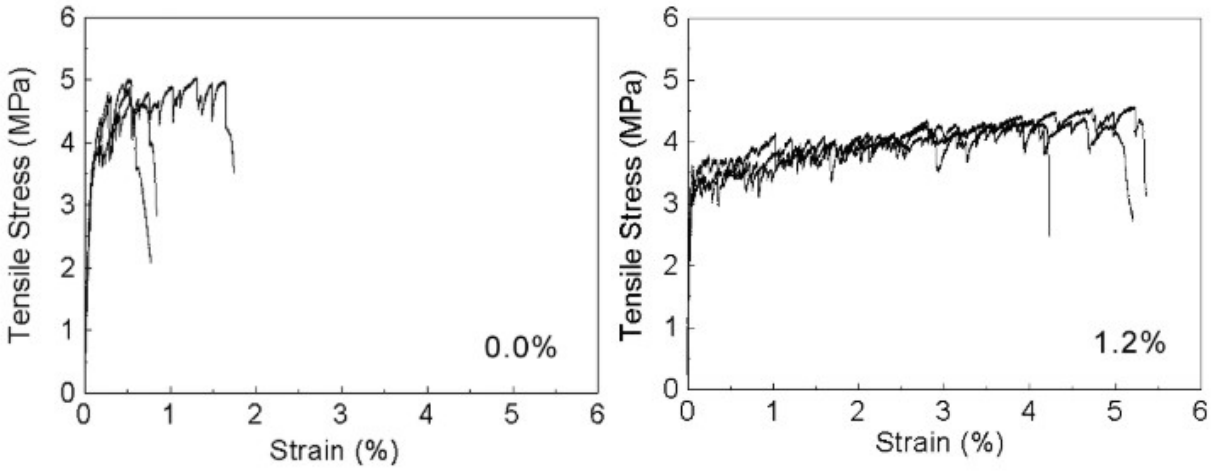

Figure 2.11: Ductility of the composites as a function of oiling content (Li 2011)

In the study of Georgiou et al (2014), four different types of coating agents with different mass ratios were considered and tested. It was concluded that number of fine cracks increase in number prior to crack localization when higher mass ratios of coating are used.

Other important parameters in the response of UHPC include the aspect ratio of the fibers and the gradation of the aggregates used in the mix. Aggregates in fact play the role of flaws embedded in the gel structure and therefore their size and surface roughness determine the length scale of the material before brittle rupture; in this regard the gradation curve is a critical parameter in determining the resilience and strain capacity of the mix. The fiber aspect ratio is very relevant in this regard: the fiber length is orders of magnitude larger than the maximum aggregate, and it determines the contact surface over which bond may develop in a manner that is very similar to “development length” in normal reinforced concrete: $0.5\, l_f = \varepsilon_f\ (d_f/4)(E_f/f_{bf})$, where ε_f is the fiber strain that may be supported and l_f is the available fiber length. To illustrate the role of the aspect ratio on strain development capacity the above expression is rearranged as follows:

$$\varepsilon_f = 2(L_f/d_f).(f_{bf}/E_f) \tag{2.13}$$

2.3.3 Fly Ash as Cement Replacement and Sustainability

Researchers in Fiber Reinforced Cementitious Composites (FRCC) have made remarkable advances and the field has matured with increasing momentum in recent years. One of several reasons behind this is the increased usage of micro-fillers like fly ash, slag, and silica fume as cement replacement and the interest in documenting their effect on strength, durability and ductility (Naaman and Reinhardt 2003).

Fly ash is a bi-product of burning coal in the energy industry. In the past, factories released fly ash into atmosphere but nowadays air pollution control standards oblige industries to capture and store it. Fly ash exhibits hydraulic and pozzolanic properties and contains silicon dioxide (SiO2), aluminum oxide (Al2O3) and calcium oxide (CaO) (Georgiou and Pantazopoulou 2016). Fly ash has been used early on together with other binding agents such as Portland cement to produce cementitious components and therefore it is now considered a valuable resource in the construction industry. Due to the reaction of fly ash with calcium hydroxide ($Ca(OH)_2$) in the gel, calcium silicate hydrates (C-S-H) with cementitious properties are produced (Hopkins et al. 2001). The use of fly ash in concrete goes back to start of 19^{th} century (Anon 1914). However, the last 50 years its usage has grown dramatically exceeding 6 million tonnes per year in United States alone (Manz 1993).

To use fly ash as cement replacement special attention should be placed on its pozzolanic function. The reaction of fly ash with calcium hydroxide ($Ca(OH)_2$) released by Portland cement is slower than cement hydration reactions. Therefore, as fly ash concrete gains strength more slowly at early ages than plain Portland cement concrete, UHPC structures containing fly ash need to be moist cured properly specially at early ages (Hopkins et al. 2001).

Fly ash has spherical shape particles (Jiménez-Quero et al. 2013) and in case of high fineness, using fly ash reduces friction between particles and increases workability and consolidation (Ferraris et al. 2001). Consequently, as reported by Thomas (2007), as a gross approximation, every 10% cement replacement by fly ash leads to 3% reduction in water demand. As a result of reduction of water content, bleeding and segregation in fly

ash concrete would decrease. Packing density of concrete is improved by addition of fly ash and therefore affects the permeability of concrete and makes it more durable (Georgiou 2017).

Two parameters mostly characterized the rheological properties of concrete: plastic viscosity and yield stress (Bentz et al. 2013). The rheological properties of concrete are improved by addition of fly ash (Ferraris et al. 2001) which makes it an economical option to use in order to achieve a self-consolidating concrete (SCC) (Bentz et al. 2013).

Various researchers investigated the interaction of fly ash and PVA fibers (Song and Zijl 2004, Wang and Li 2005, Peled and Shah 2016). Peled and Shah (2016) conduced an experiment studying the effect of high volume fly ash (70% by volume replacement of cement) in PVA Fiber Reinforced Concrete. In order to measure the “topography surfaces of cement composites”, Atomic Force Microscopy (AFM) was used. They observed that in extruded specimens, fly ash reduced the bond strength of fibers and the surface of the fibers were smooth and pull out behaviour was observed while in the composite without fly ash, roughness of fiber surface was observed, and it is suggesting that high friction existed between fibers and the cement matrix leading to fiber rupture rather than smooth pull out.

2.3.4 Durability

Durability properties of Strain Hardening Fiber Reinforced Concrete (SHFRC) has been investigated by various research groups (Miyazato et al., 2005, Zijl et al. 2012, Ahmed and Mihashi 2007, Lepech and Li 2009). Research results show durability properties of SHFRC such as crack width control, permeability in the cracked state, corrosion resistance, freezing and thawing resistance, performance in hot environments, and shrinkage cracking resistance outperform those of normal concrete (Ahmed and Mihashi 2007). Lepech and Li (2009) investigated the water permeability of Engineered Cementitious Composites (ECC). They stated that since ECC has multiple cracking behaviour and micro cracks (with width of approximately 60 μm) are formed rather than one localized big crack, the performance of cracked ECC regarding water permeability is similar to that of uncracked plain concrete. Studies also confirm that resistance of SHFRC

to aggressive substances is better than plain concrete because of tight crack widths in the former. Studies on chloride penetration confirm that penetration of chloride depth is shallower than that of normal concrete (Miyazato et al. 2005). Freezing and thawing tests on SHFRC also show that up to 300 cycles it remains durable without degradation of dynamic modulus, in contrast to what is reported for normal concrete that can only survive up to 110 cycles with severe degradation (Yun and Rokugo 2012, Lepech and Li 2006).

2.3.5 Self Consolidating Concrete (SCC)

Casting of PVA-ECC is a more challenging task than normal concrete due to the presence of fibers in PVA-ECC. If ECC does not have good workability, any vibration or consolidation may lead to amorphous distribution of fibers and the fibers efficiency will be reduced. Therefore, a self consolidating ECC is desired that it flows by itself (without consolidation) under gravity and can be casted into any complex mold. Self consolidating ECC is achieved by optimizing two sets of parameters, namely micromechanical and processing characteristics. The former control concrete properties in hardened state through properly selection of the matrix, fiber, and interface properties whereas the other is related to rheological properties in fresh state by optimal use of superplasticizer and viscosity agent. In order to develop a self compacting ECC, friction between aggregates also has to be minimized by optimum selection of amount and surface roughness of the coarse aggregate (Li et al.1998).

2.3.6 Shear Behaviour of Fiber Reinforced Cementitious Composite

Shear failure in normal concrete is generally brittle. The underlying mechanism behind shear failure is not yet completely understood, whereas most of codes of practice contain empirical formulations and therefore a large disparity exists between Codes and experiments. This requires large safety factors (more than 2) as prescribed by codes of practice for R.C. structures to predict the shear capacity of beams. Therefore, if concrete could be altered to a more ductile material, the demand for using traditional stirrups could be reduced or even eliminated.

For the past decades, many researchers have been studying the effect of fibers on shear resistance and shear crack distribution in FRC structural members and fibers found to improve these properties. Various approaches to predict shear carrying capacity have been proposed, however, these approaches are precise only for the particular circumstances and for a different geometry or material, the predictions are underestimated or overestimated (Paegle and Fischer 2016).

Studies have been focused more on steel-fiber FRCC, where the effectiveness of fibers as shear reinforcement is the object of investigation. However, few published studies exist on the effectiveness of synthetic fibers as shear reinforcement of concrete. The reason behind the limited use of synthetic fibers is perhaps attributed to the fact that mostly polypropylene based synthetic fibers have been used with small improvement in toughness and ductility (Yazdanbakhsh et al. 2015). However, using new generation of micro synthetic fibers such as polyvinyl alcohol (PVA) enabled the development of Engineered Cementitious Composites (ECC) which have much higher tensile strength, higher ductility, and strain hardening and multiple cracking behaviour (Li 2002).

Because of the limited number of studies on synthetic fibers, some codes such as ACI do not allow the use of synthetic fibers as a shear reinforcement. However, studies on PVA fibers have confirmed the beneficial effect of fibers on shear strength of concrete beams (Shimizu et al. 2004, Paegle and Fischer 2016, Hou et al. 2015, Majdzadeh et al.2006). A summary of suggested design equations for quantifying the shear contribution of FRCC in different codes is presented in Chapter 7.

2.4 Experimental Investigation

2.4.1 Background

In North America, no standardized test method exists to evaluate the shear strength of cementitious composites. Xu and Reinhardt (2005) summarized some of the available testing setups and specimen forms conducted by researchers around the world (Figure 2.12)

It is important that the test method and specimen preparation remain simple. In general, shear strength of concrete can be determined by performing two different types of tests:

(a) Direct Shear Tests: Push-off tests are among direst shear tests that enable investigation of shear strength by relating shear to the tensile properties.
(b) Beam Tests: Four-point bending tests are one of the acceptable traditional shear tests on reinforced concrete beams and used also to obtain tensile strength indirectly from flexural strength.

After a comprehensive literature review, few pertinent experimental investigations into shear behaviour of PVA-ECC were found. A summary of these studies is presented in Chapter 7. The sparse number of tests in this area might be attributed to the fact that various types of fiber and mix design exist causing great variety in in the parametric basis of the experimental literature, whereas large-scale production of ECC is difficult and need special consideration.

As a result of a limited research in structural behaviour of ***synthetic*** Fiber Reinforced Cementitious Composites, it has not been codified yet. However, promising results of experimental studies on PVA-ECC confirm that a new generation of concrete will be commercially available soon which will make a big difference in the construction industry.

2.4.2 Direct Shear Tests

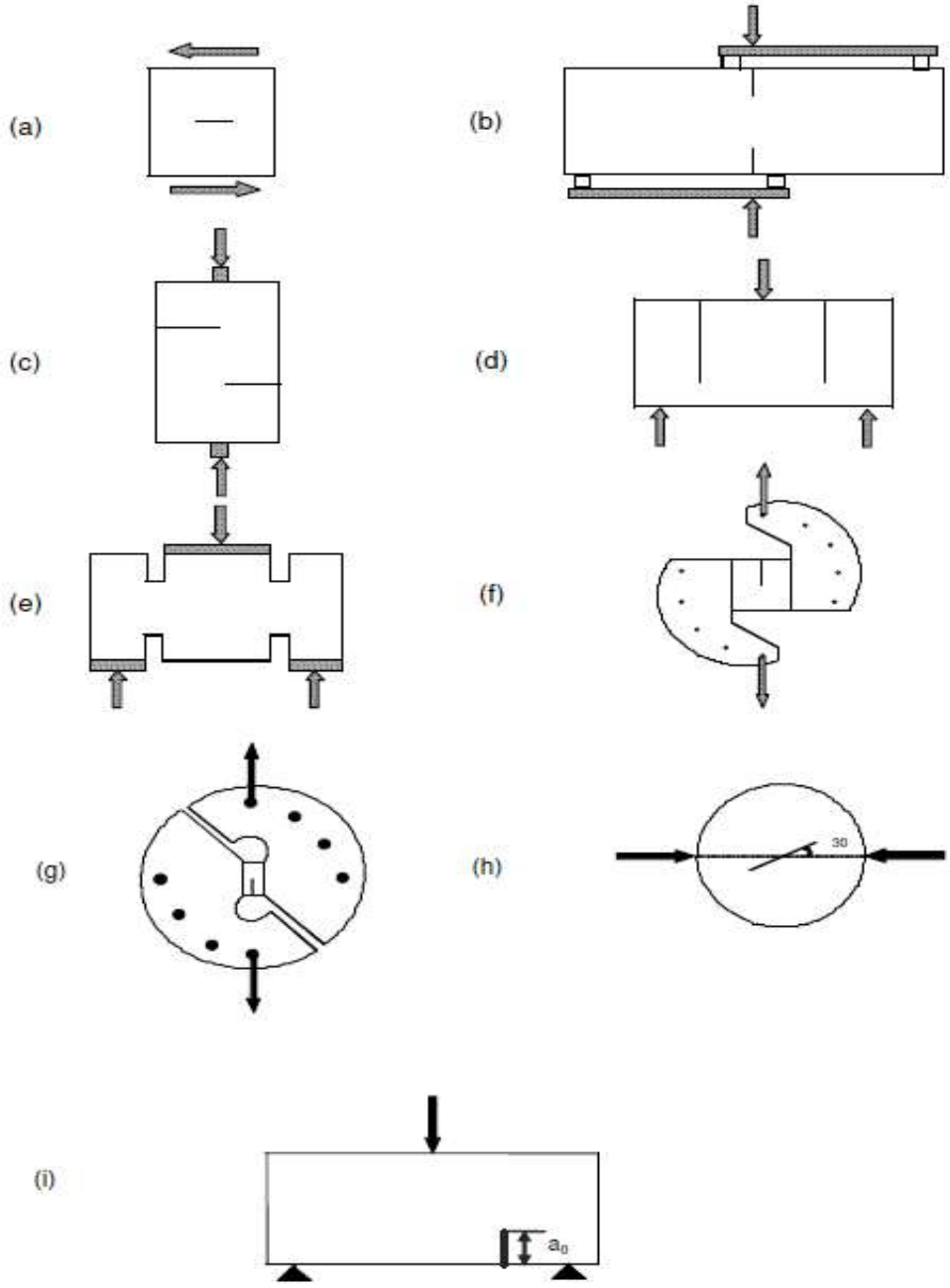

Figure 2.12: Different testing configurations to study shear (Xu and Reinhardt 2005)

Z-shape push-off specimens have been the subject of much research to study the transfer of shear across an interface (Mattock and Hawkins 1969, Walraven and

Reinhardt 1981, Foster et al. 2016). In conventional push-off tests, as depicted in Figure 2.13 (a), a failure plane concentric with and parallel to an applied load is considered to simulate the pure shear across an interface. Mattock and Hawkins (1969) modified the conventional push-off specimen geometry in such a way as to have a diagonal failure plane (at +ve angles θ varying from 0° to 75°). This diagonal failure plane is concentric with, but inclined to the applied load and its orientation is designed to create a slidding plane that is subjected to a combination of compression and shear stresses (Figure 2.13 (b)). With a further modification, Foster et al. (2016) also developed another push-off specimen to generate a failure plane (at -ve angles θ) subjected to combination of tension and shear stressess (Figure 2.13 (c)).

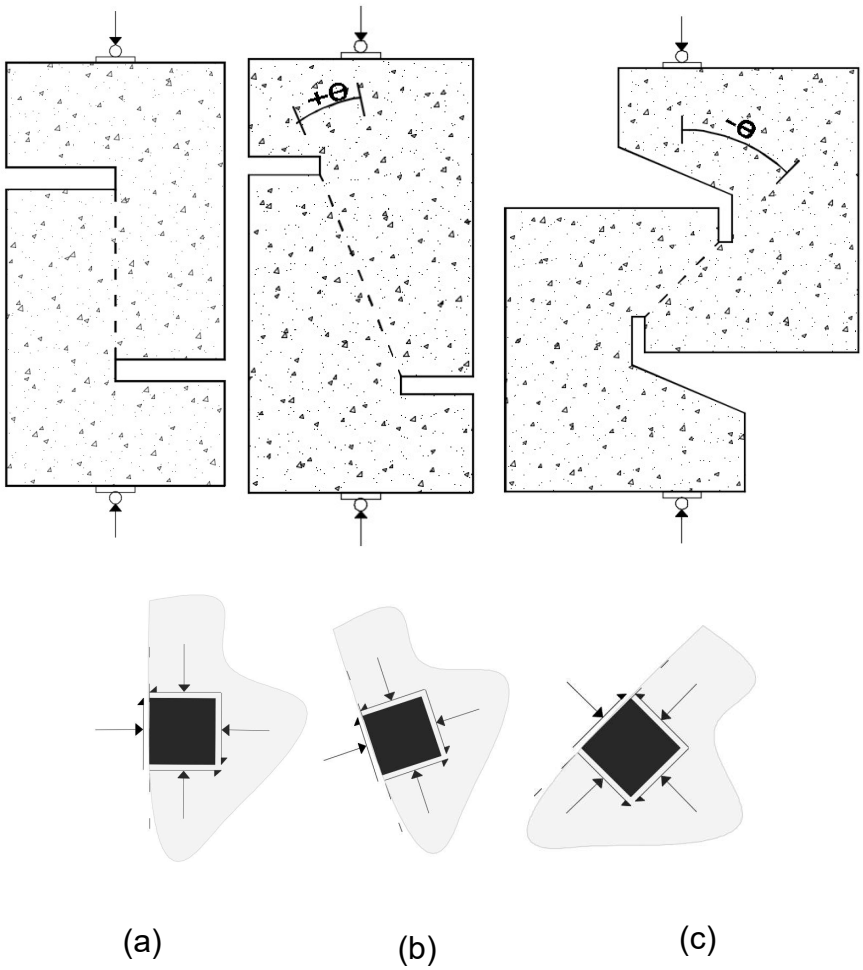

Figure 2.13: Push-off specimens: (a) Pure shear (b) Compression Shear (c) Tension Shear (adapted from Foster et al. 2016)

With the emergence and further development of ECC evaluating the contribution of this material to shear strength is a priority. Although some studies using push-off specimens have been conducted (Kang et al. 2017, Georgiou 2017), however, due to lack of sufficient and comprehensive experimental evidence, the shear resistance of ECC is simply taken using the same expression as for plain concrete in many of the design codes.

CHAPTER 3: ANALYSIS AND INVESTIGATION OF ACI-ASCE SHEAR DATABASE

3.1 Introduction

As was discussed in Chapter 2, ACI-ASCE Committee 445 (referred to hereon as C445) established a carefully controlled database of hundreds of concrete beam tests (Reineck et al. 2003, Belarbi et al. 2017). The database has been used to refine a variety of empirical design expressions and models for V_c. In 2014, C445 invited researchers to submit their new proposals for a safer and more reliable design expression and the litmus test for acceptance of any proposal was its performance against the ACI database. A total of 6 proposals reached the final stage which will be discussed in detail in this chapter.

3.2 Proposals for a Safer One-way Shear Strength Design Expression

A total of 10 proposals were submitted for V_c, which were eventually reduced to six, as listed in Table 3.1 along with the current (ACI 318-14) design expression for the "concrete contribution to shear strength", V_{ACI}.

Table 3.1: Competing Design Expressions for V_c after the recent campaign by C445*

Proposal ID	Concrete contribution to shear strength, V_c
ACI 318-14	$V_c = 2\lambda \sqrt{f_c'} b_w d$
(Bentz and Collins 2017) (for beams without stirrups and 3/4 in. aggregate size)	$V_c = \frac{100}{38 + s_x} \sqrt{f_c'}\, b_w d$ $s_x = 0.9\, d$
(Cladera et al. 2017) ***(note: the limit on c/d proposed by the authors has been neglected because it yielded***	$V_c = 6\lambda\xi \frac{c}{d} \sqrt{f_c'}\, b_{v,eff} d < 4\left(1.25\xi \frac{c}{d} + \frac{1}{d_0}\right) \sqrt{f_c'}\, b_w d$ $\xi = \frac{2}{\sqrt{1+{d_0}/{8}}} \left(\frac{d}{a}\right)^{0.2}$; $a = \frac{M_{u,max}}{V_{u,max}}$;

unrealistic strength estimates)	$d_0 = max\{d, 4in\};$ $\frac{c}{d} = 0.75\,(n\rho)^{1/3}, n = \frac{E_s}{E_c}, \rho = \frac{A_s}{b_w d}$
(Frosch et al. 2017)	$V_c = \left(5\lambda\sqrt{f_c'}\ b_w c\right)\gamma_d$ $c = d(\sqrt{2\rho n + (\rho n)^2} - \rho n)\ ;\ \rho = \frac{A_s}{b_w d}\ ;$ $n = \frac{E_s}{E_c};\ \ \gamma_d = 1.4/\sqrt{1 + {}^{d_t}/_{10}}$
(Li et al. 2017)	$V_c = 17\lambda\left(\frac{V_u d}{M_u}\right)^{0.7} \cdot \sqrt{f_c'}\ b_w c \cdot \frac{1}{\sqrt{1 + {}^{h}/_{11.8}}} < 10\lambda\sqrt{f_c'}\ b_w c$ $c = d\left(\sqrt{2\rho n + (\rho n)^2} - \rho n\right)\ ;\ \rho = \frac{A_s}{b_w d}\ ;\ n = \frac{E_s}{E_c}$
(Park and Choi 2017)	$V_c = k_s f_t b_w c\ cot\phi$ $k_s = \left(\frac{12}{d}\right)^{0.25} < 1.1 \quad ;\ \ f_t = 2.2\lambda\sqrt{f_c'}\ ;$ $cot\phi = \sqrt{1 + {}^{\sigma_{ct}}/_{f_t}}\ ;\ \sigma_{ct} = \frac{M_u}{b_w c\,(jd)}$
(Reineck 2017)	$V_c = \left[71\,\lambda\,\left(\rho\,\frac{f_c'}{d}\right)^{1/3}\right] b_w\, d \qquad \rho = \frac{A_s}{b_w\, d}$

* All equations are in U.S customary units (psi, in).

Table 3.2: Notation used in Table 3.1

$\boldsymbol{\lambda}$	Modification factor for light weight concrete
$\boldsymbol{f_c'}$	Specified compressive strength of concrete
$\boldsymbol{b_w}$	Web width
$\boldsymbol{d}$	Effective depth, distances from the outermost compressed concrete fiber to the centroids of the mild steel

s_x	Effective crack spacing in the longitudinal direction
ξ	Combined size and slenderness factor
c	Neutral axis depth
$b_{v,eff}$	Effective flange width for shear strength
d_0	Maximum of effective depth d or 4 in
a	Shear span
$M_{u,max}$ and $V_{u,max}$	Maximum absolute values of the internal forces in the region between the maximum bending moment and the zero-bending moment in which the considered section is located
E_s	Modulus of elasticity for deformed steel bar reinforcement
E_c	The modulus of elasticity for concrete
n	Elastic modulus ratio
ρ	Longitudinal reinforcement ratio
A_s	Reinforcement area
γ_d	Size effect factor
d_t	The distance from the extreme compression fiber of the member to the centroid of the reinforcement nearest the tension face.
h	Height of the cross section
$\left(\frac{V_u d}{M_u}\right)^{0.7}$	Arc action factor
M_u and V_u	Factored internal forces
k_s	Size effect factor
f_t	Concrete tensile strength
ϕ	Inclined crack angle
σ_{ct}	Average compressive normal stress developed by flexural moment
jd	Moment lever arm

3.3 Statistics and Analysis

The performance of ACI-318 design expression for one-way shear strength was examined against ACI database and was presented in Chapter 2. For the sake of comparison with the performance of the competing proposals, the graph is repeated here again (Figure 3.1). Figure 3.1 (a) plots the dispersion around the value of 1 (a standard deviation of 0.63), of the ratio of the experimental shear strength normalized by the ACI estimate. Also shown is the mean (=1.44), the median (=1.42), and the values with 5% and 95% probability of being exceeded above or below these limits respectively. In the Figure 3.1 (b) the experimental points (horizontal axis) are plotted against the estimated values using the ACI equation. Good performance would lead to clustering of the points along the equal value line. The advantage of this way of presenting the data is that larger specimens may be easily identified, so as to illustrate the size effect issue. Note that the discrepancy between analysis and test results increases in the range of larger forces measured (i.e. in larger beams, Figure 3.1(b)). Here in this section, to investigate the performance of four of the most prominent proposals, they are also examined against the ACI database (Figure 3.2).

The proposals by Bentz and Collins (2017), Frosch et al (2017), Park et al. (2017), and Reineck (2017) are tested against the database because after the extensive debate that followed the C445 solicitation, these proposals were considered as prominent solutions. Again, performance is assessed by comparing the experimental with the analytical values on an equal value plot. Specimens clustered along the 45^{o} line are successfully calculated by the respective model. In the following four plots it is seen that the data clouds deviate in the range of higher member sizes indicating a persistence of the size effect. However, clearly the scatter has been reduced as compared to the ACI expression.

In the effort to interpret the source of the persisting discrepancies between theory and experiment, the models were reviewed to identify possible sources of size effect. It was concluded that, in fact, several important parameters that affect the concrete-reinforcement interaction, such as bar diameter size, cover, and development length, have been neglected in the emerging shear strength proposals. All of these are parameters that control bond and development capacity of the main reinforcement in

flexural members. Considering that in the absence of stirrups shear failure by diagonal tension failure of concrete always finishes with splitting failures along longitudinal bar anchorages, this is an unexpected finding, as the authors of the database completely forego any attempt to calibrate the size effect with bond related parameters.

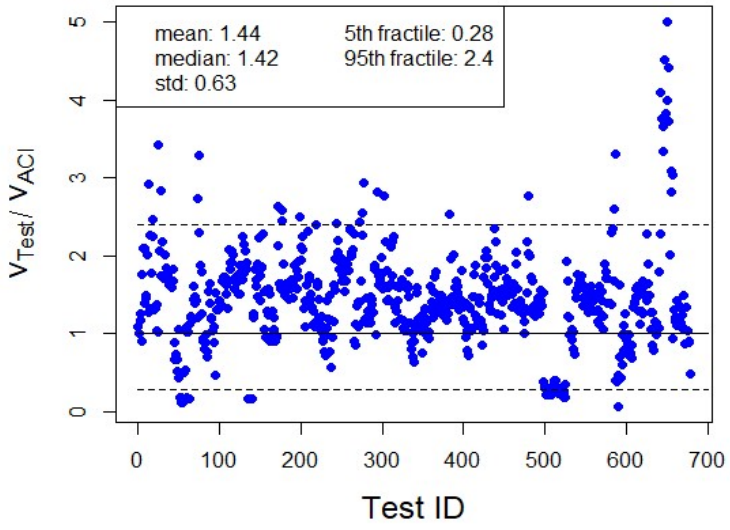

Figure 3.1: (a) Measured V_c value normalized with respect to V_{ACI};

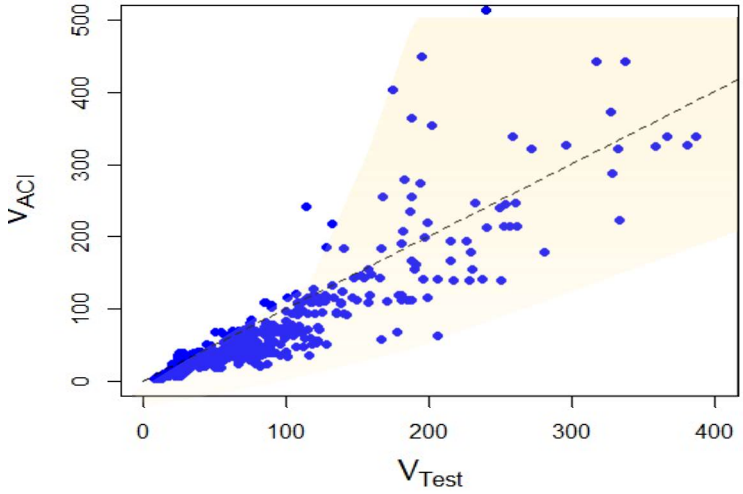

Figure 3.1 (b) V_c plotted against V_{ACI}: note that the discrepancy increases in the range of larger forces measured (i.e. in larger beams)

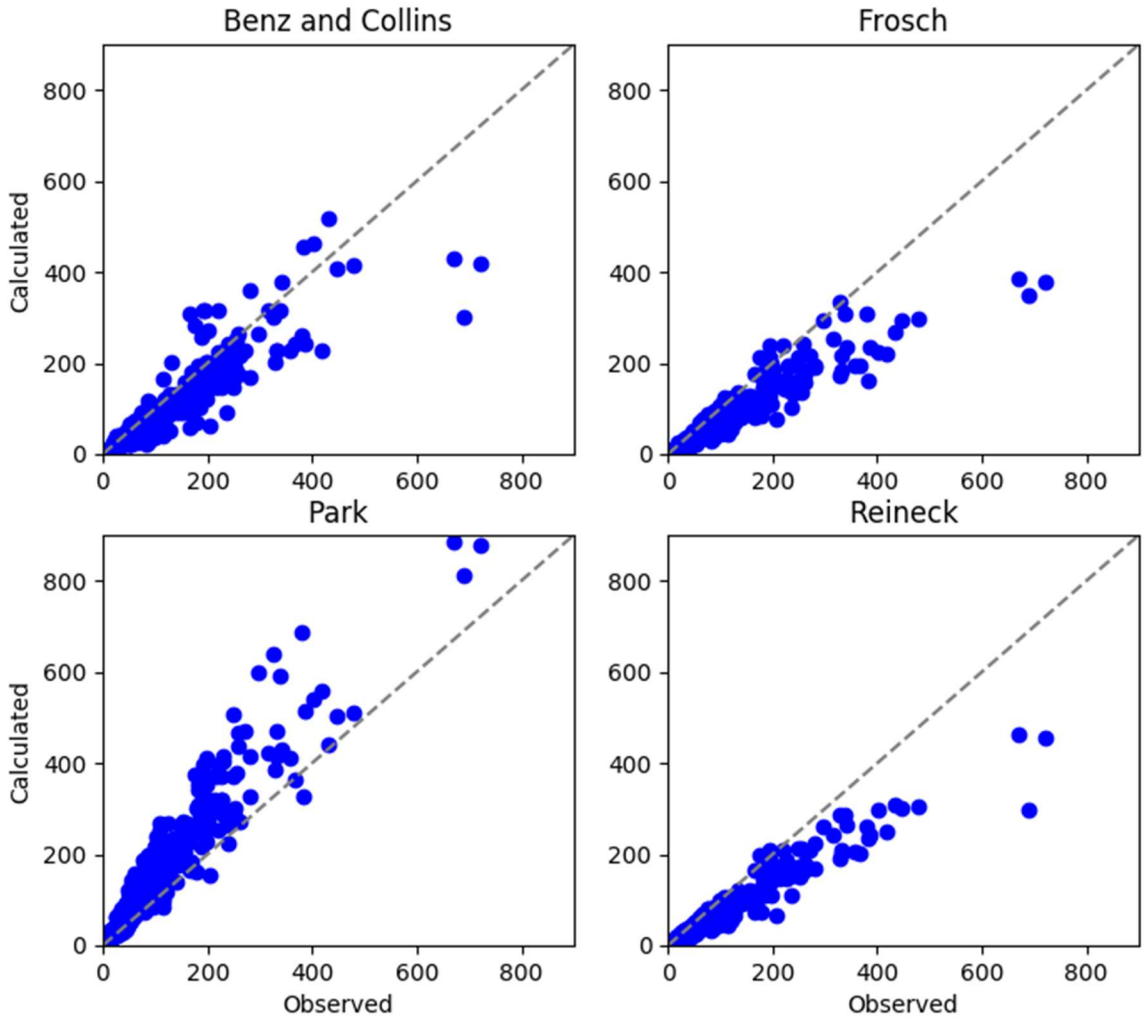

Figure 3.2: Performance of four different proposals against the C455 database

In fact, recent advances in the study of bond and anchorage have provided insights into a totally new interpretation of shear failure. It is shown in Chapter 4 that strain penetration over the unconfined length, which spreads further into the anchorage with increasing moment at midspan, may propagate over the entire length of available longitudinal reinforcement, perpetrating brittle failure and collapse at loads that are much lower than the nominal shear strength. With this approach it is possible to reproduce successfully the experimental trends and to provide an alternative interpretation to the size effect which seems to be owing to the reduced bond strength of larger size bars in unconfined

anchorages and the need for longer anchorage lengths - parameters that have not been accounted for in the past when calibrating shear models with test results. This model has been developed in this thesis and is discussed in detail in Chapter 4.

CHAPTER 4: AN ALTERNATIVE INTERPRETATION OF ONE-WAY SHEAR STRENGTH: STRAIN PENETRATION IN LONGITUDINAL BAR ANCHORAGE

4.1 Introduction

Significant effort has been vested over the years in quantifying the contribution of concrete to the shear strength of RC members. Chapter 3 reviewed design code expressions that have been calibrated against a carefully assembled database of tests, where success of each design proposal is tested from its concurrence with the experimental sensitivities for the range of the design parameters, including size-related phenomena which are attributed to the brittle fracture of concrete.

However, the issue of understanding the size effect from fundamentals so as to be able with safety to predict failures of larger members that are not already part of the database. In this front, recent developments in the effects of strain penetration on the shear span of laterally swaying columns have provided insights into a totally new interpretation of shear failure in the shear span of flexural members (Megalooikonomou et al. 2018). This finding ride on previous findings (Darwin et al. 2001, Tastani and Pantazopoulou 2007) according to which the fracture energy of concrete limits the strain development capacity of an anchorage; once the maximum sustainable strain is reached by the anchorage, cover splitting ensues, and it propagates precipitously leading to anchorage failure. This effect known as “unzipping” of the anchorage, may propagate over the entire length of available longitudinal reinforcement, perpetrating brittle failure and collapse at loads that are much lower than the nominal shear strength. By incorporating anchorage equilibrium considerations in the present study, it is possible to reproduce successfully the experimental trends and to provide an alternative interpretation to the size effect which seems to be owing to the reduced bond strength of larger size bars in unconfined anchorages and the need for longer anchorage lengths - parameters that have not been accounted for in the past when calibrating shear models with test results. In this Chapter, a detailed derivation of the proposed approach is presented. Examples from the experimental database of C445 are solved using the mechanistic model for strain

penetration in the shear span of a loaded beam; analytical estimates are calibrated against the test values.

4.2 A New Perspective of the Effect of Size on Concrete Contribution to Shear

The concern regarding “size effect” in concrete beams (i.e. the slower, non-proportional scaling-up of shear strength with increasing beam depth) is reflected in the models for shear by introducing what is considered the most critical variable in determining shear strength, i.e., the aspect ratio, or ratio of shear span-to-effective depth. By inspection of the proposed equations (listed in Table 3.1), it may be seen that longitudinal reinforcement is only considered as a ratio (percentage) over the cross section, to the extent that it controls either the depth of compression zone, c, or the reinforcement dowell action $(\rho_{sl})^{1/3}$ (see Eurocode 2, 2004). Note that the underlying assumption of those models where V_c depends on c is that shear transfer in concrete only occurs over the depth of compression zone. Therefore, none of the proposals makes any reference to longitudinal bar size (diameter) and its implications on the state of bond along the reinforcement, which however is essential for the composite action of the beam. Evidently several of the parameters that affect the concrete-reinforcement interaction, such as bar size, cover, and development length, have been neglected in the emerging shear strength proposals. The significance of the effect of bar size is illustrated clearly in experimental test results presented by Taylor (1972) and Daluga et al. (2017). While other researchers reported up to 68% reduction of mean unit shear strength by increase of section depth from 12 to 36 in. (305 to 914mm), Daluga et al. (2017) claimed that the reduction is much smaller (14%) for beam depth from 12 to 48in. (305 to 1219mm) and it is even smaller than the statistical error of experimental data. They surmised that that several crucial variables play a role in what is macroscopically observed as non-proportional increase of strength with member depth, such as maximum aggregate size, bar cover, bar diameter and spacing. They also argued that if tests conducted to quantify size effect are controlled in a way that variables change by the same proportion, the scatter of results are not more than standard experimental error. They also mention the variation in results in small and large beams might be due to the fact that casting and curing conditions are different for geometrically similar small and large size beams. Furthermore, in larger beams with

larger aggregate size and reinforcing bars, the concrete around aggregate and reinforcing bars is weakened due to more bleeding water that is trapped under aggregates and reinforcing bars, generally leading to a lower bond strength. They also suggested that although no clear correlation is reported between tensile strength of concrete and aggregate size, variation of concrete tensile strength might introduce an unintended variable that was not accounted for in the test programs.

It is worth noting here, that size effect is explicitly recognized in bond research (fib Bulletin 72, 2014): Larger bar sizes have lower bond strength, whereas cover splitting, and anchorage length are not proportional to the bar size (fib Model Code 2010):

$$f_{b,0} = \eta_1\eta_2\eta_3\eta_4({}^{f_{ck}}/_{20})^{0.5}/\gamma_c \quad (4.\ 1)$$

where, $f_{b,0}$ is the design bond strength; f_{ck} is the characteristic cylinder concrete compressive strength; η_1 accounts for the bar profile (η_1*=1.8* for ribbed vs. η_1*=0.9* smooth bars); η_2 accounts for the "top bar" effect (*=1* in the absence of top bar effect, i.e. in the lower part of a horizontally cast member or in the case of vertical bars); η_3 accounts for the bar diameter effect (*=1* for $D_b \leq 20mm$, $\eta_3=(20/D_b)^{0.3} < 1$ for $D_b > 20mm$); η_4 accounts for the characteristic strength of steel reinforcement (*=1.2, 1.0,* and *0.85* for f_y*=400, 500* and *600 MPa* respectively), and γ_c is the material safety factor (taken *equal to 1.5*). The ultimate bond strength, f_{bd}, is obtained also considering the effect of confinement:

$$f_{bd} = (\alpha_2 + \alpha_3)\, f_{b,0} + 2p_{tr} < 2f_{b,0} + 0.4p_{tr} < 2.5\sqrt{f_{ck}} \quad (4.\ 2)$$

where α_2, α_3 represent the influence of passive confinement from cover and from transverse reinforcement, respectively, and p_{tr} is the transverse pressure that engages frictional resistance at the splitting plane. Therefore, the concept that shear failure of beams without stirrups may be an indirect manifestation of bond failure has been qualitatively proposed before, but it is quantified through modeling in the present thesis.

4.3 Effect of Development Length on Shear Strength

Here in this section, considering the mechanics of bond, development of bar stresses in the shear span is studied (shear span is the length in which the applied moment decreases from its peak value to zero according to statics). It is shown that the governing mechanism behind the failure of many tests that are treated in the ACI database as “shear failures” are in fact bond failures along the longitudinal reinforcement which is very much affected by the bar size. Therefore, the problem referred to “size effect” in shear, is in fact much more related to the scaling-up of the bar size in larger size specimens.

Recently, the solution of the governing equations of bond of a bar developed under a moment gradient was established (Megaloeconomou et al. 2018). Formation of the disturbed region near a flexural/shear crack was illustrated from first principles, thereby verifying the long term standing conviction that near points of high shear demand and points of geometry change the hypothesis of plane sections remaining plane is not valid. In the disturbed regions the stresses in the reinforcing bar cannot be obtained from flexural analysis considering the moment acting in the cross section of interest, but rather, stresses are controlled by the solution of the bond equation. As the flexural moment in critical section increases, the disturbed region spreads towards the support and the end of the bar in the shear span. This process is referred to as strain penetration (Figure 4.1).

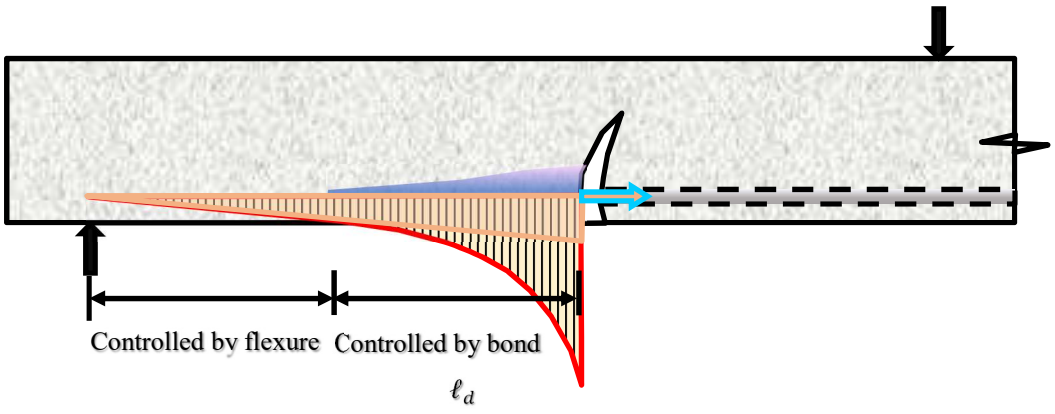

Figure 4.1: Strain Penetration in Tension Reinforcement

Before, inelastic strain penetration in the anchorage of a reinforcing bar had already been established in the absence of simultaneous moment (Tastani and Pantazopoulou 2013a, Tastani and Pantazopoulou 2013b). Megalooikonomou et al. (2018) used this solution to determine the plastic hinge length in the shear span of a laterally swaying column.

In the following section an analytical procedure is developed seeking the onset of shear failure and the associated strength of the failure mechanism in concrete beams. The basis of the algorithm is the solution of the bond equations over the segment of the shear span where a disturbed region is determined. Disturbance is considered to occur adjacent to a flexural crack. The reason is that exactly at the crack location the concrete and the reinforcement no longer share equal strains (compatibility), while it takes a non-trivial length from the crack for the two materials to regain compatibility – this distance is the disturbed length. An essential step in the algorithm is to first, localize the position of each new flexural crack until attainment of the stage known as “crack stabilization”. Location of primary flexural cracks is the starting point for calculating the disturbed region and for monitoring its propagation with increasing load. The last possible flexural crack location is critical, and it depends on the ratio of M_{cr}/M_{max} . If the residual development length from the last crack to the bar end is not sufficient in order to develop the bar force demand, bond failure occurs, manifested by splitting along the anchorage towards the bar end, and accompanied by beam failure, generally at a load that is much lower than the beam shear strength (Figure 4.2). A summary of the analytical steps of this derivation is presented in detail in the following sections.

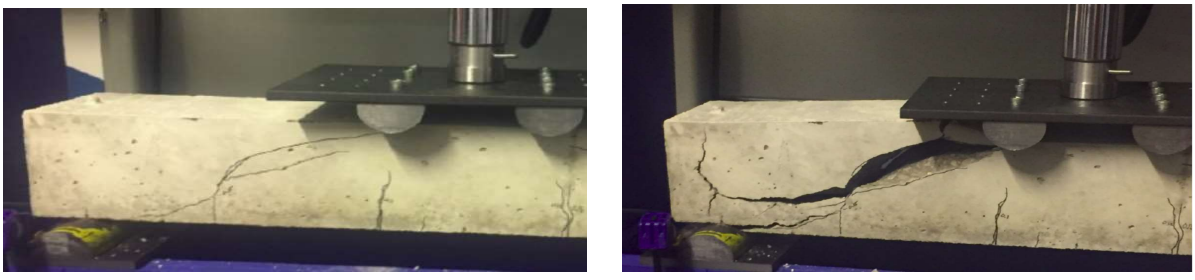

(a) (b)

Figure 4.2: Failure patterns in a beam without stirrups with longitudinal 3-10M bars at the onset of shear cracking (a) and at failure (b). Note the manifestation of anchorage failure preceding the brittle failure of the beam, despite the a/d ratio exceeding the limit of 2.

4.4 State of Stress in the Shear Span of a Beam

The moment distribution along the shear span of a beam, of length L_s, (Figure 4.3) follows Eq. (4.3a):

$$M\ (x) = M_0\ (1 - {}^{x}/_{L_s}) \qquad (4.3a)$$

Before cracking, the strain in the bar and concrete at the level of the reinforcement, $\varepsilon_{fl}(x)$, is given by Eq. (4.3b), where y_g is the distance of the reinforcement from the centroid of the cross section. With increasing load, and when peak moment at midspan exceeds the cracking moment M_{cr}, the first crack occurs in the critical region, usually under the point load; this location is used as point of reference hereon, and therefore $x_{cr1} = 0$ (i.e., first crack at x_{cr}). From flexural analysis, bar stain is estimated from:

$$\varepsilon_{fl}(x) = M\ (x).\, y_g / E_c.\, I_g \qquad (4.3b)$$

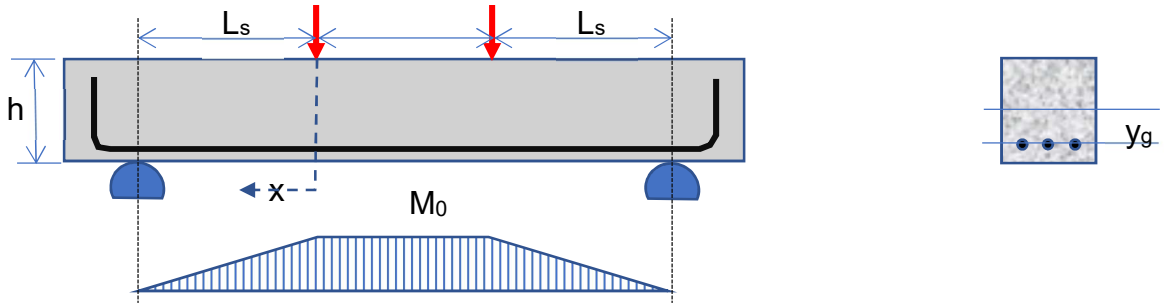

Figure 4.3: Moment distribution along the length of a beam: L_s is the shear span

In fact, a pre-requisite to the analysis that follows is the calculation of the moment-curvature relationship for the beam cross section; from this analysis it is also possible to draw (from the results) the relationship between moment and reinforcing bar strain: this diagram, which is calculated from standard sectional analysis described the relationship between moment and bar strain at the discrete crack locations (Figure (4.4a)). However, it does not represent accurately the corresponding moment-strain relationship between successive cracks. This aspect of the problem is referred to the state of bond that is engaged between cracks.

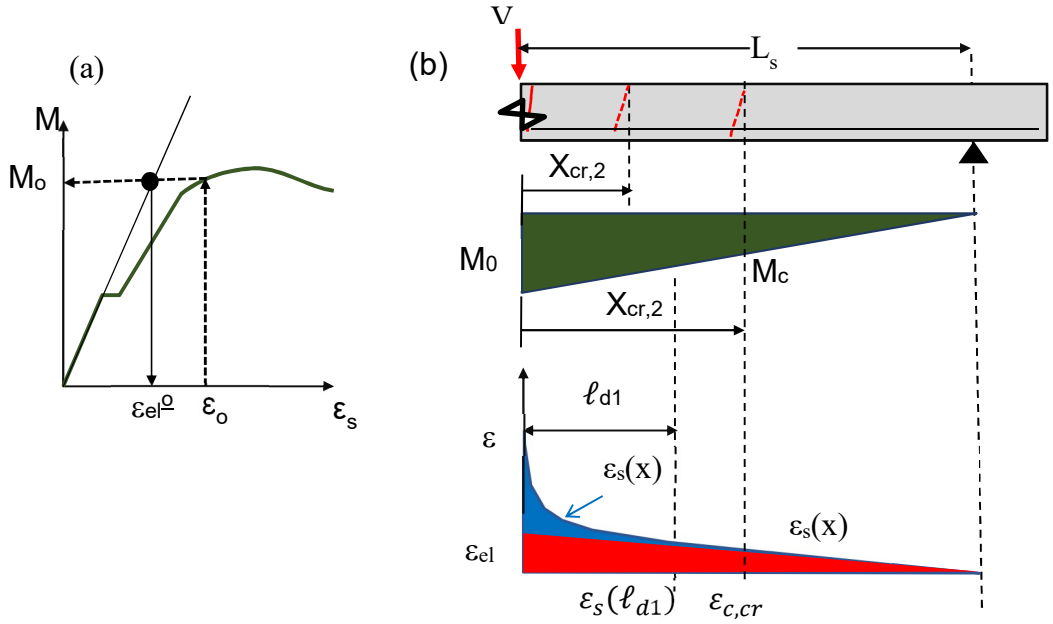

Figure 4.4: a) moment vs. steel strain $\varepsilon_s(x)$ obtained from sectional analysis. (b) Moment and steel strain distributions along the l_s. (Note: Red $\varepsilon_s(x)$: stage prior to cracking. Blue $\varepsilon_s(x)$: bar strains in cracked region (strain at the critical section experiences a significant jump upon cracking)).

Upon fist crack formation, the effective section stiffness is reduced drastically (e.g. around 1/3 of uncracked stiffness). Therefore, with an imperceptible increase of moment at the critical section to $M_{cr} + \delta$ the bar strain experiences a significant jump in order to maintain equilibrium. At the crack, the concrete strain at the bar level reduces to zero due to cracking whereas the reinforcement strain increases dramatically to ε_{so} $(x = 0)$, where it is assumed that the post-cracking relationship between flexural moment, curvature and bar strain has been computed from classical sectional analysis of the critical section. Once the compatibility between bar and concrete normal strain is violated by cracking, it ceases to be valid over a distance, l_{D1}, away from the crack (Figure (4.4b)). The resulting "disturbed region", l_{D1}, is a necessary development length for bar stresses before concrete may be fully engaged again through bond. Thus, Eq. (4.3a) is no longer valid over l_{D1}. Instead, the bar strain is calculated over l_{D1} from bond. Note that the governing equations that describe the transfer of force from bar to the surrounding concrete cover,

and the corresponding compatibility between bar slip s, concrete strain,ε_c, and bar strain, ε_s, are as follows:

$$\frac{df}{dx} = \left(-\frac{4}{D_b}\right) f_b \tag{4.4a}$$

$$\frac{ds}{dx} = -(\varepsilon_s - \varepsilon_c) \approx -\varepsilon_s \tag{4.4b}$$

Here it is assumed that ε_c is negligible in comparison with ε_s. Considering the stress-strain and bond-slip relationships for the reinforcement (ascending branch in Figure 4.3a): $f_s = f_s(\varepsilon_s)$ and $f_b = f_b\,(s)$, the bar strain, $\varepsilon_s(x)$, may be calculated for segment l_D from solution of Eq. (4.4a) and Eq. (4.4b). Here, the reinforcing bar stress-strain relationship, $f_s(\varepsilon_s)$, is considered elastic-plastic with hardening (Figure 4.4a) whereas the local bond-slip relationship $f_b\,(s)$ is assumed to be a linear elastic, perfectly plastic curve with zero residual bond (Figure 4.4b). Upon substitution in Eq. (4.4a) and Eq. (4.4b) of the ascending linear equations of $f_s(\varepsilon_s)$ and $f_b\,(s)$ the following differential equation of bond is obtained (Eq. (4.6)):

$$\frac{d^2\varepsilon_s}{dx^2} = \left(-\frac{4f_b^{max}}{s_1 E_s D_b}\right) \tag{4.5}$$

which is solved for the bar strain, $\varepsilon_s\,(x)$, over l_{D1}:

$$\varepsilon_s(x) = C_1 e^{-\omega} + C_2 e^{\omega x}\text{ , where, } \omega = \sqrt{4f_b^{max}/E_s\, D_b s_1} \tag{4.6}$$

And slip which is obtained from the integration of bar strain from $x = 0\ to\ x = l_{D1}$is calculated as follow:

$$s(x) = \frac{1}{\omega}(C_1 e^{-\omega x} - C_2 e^{\omega x}) + C \tag{4.7}$$

C the constant of the integration and is obtained considering the boundary condition at the end of the disturbed zone, $s(l_{D1}) =$0.

Thus, if slip remains below the value of s_1, (Figure (4.4b)) over the disturbed length, l_{D1}, the reinforcement strain is calculated by the solution of the bond equation. The end of the disturbed length l_{D1} is defined by the requirement that the bar strains obtained at $x = l_{D1}$

from bond (Eq. 4.4) and from flexural action (Eq. (4.3)) converge – so that at $x = l_{D1}$ the bar strain compatibility with the surrounding concrete cover is satisfied. This is expressed by the boundary conditions given by Eq. (4.8) and (4.9).

For this stage, the following conditions are solved for calculating l_{D1} :

1) Slope of the strain distribution obtained from bond solution and flexure are equal:

$$\omega\,(-C_1 e^{-\omega l_{D1}} + C_2 e^{\omega l_{D1}}) = M_0.y_g/E_c.I_g.L_s \tag{4.8}$$

2) Bar strain calculated from Eq. (4.6) and Eq. (4.3b) are equal:

$$C_1 e^{-\omega l_{D1}} + C_2 e^{\omega l_{D1}} = (M_0.y_g/E_c.I_g)\,(1 - {}^{l_{D1}}/_{L_s}) \tag{4.9}$$

To develop a step by step algorithm for the solution, the tension strain ε_{s0} at the critical cross section is chosen as the controlling variable; therefore at $x = 0$, the solution of the bond equation leads to:

$$\varepsilon_s\,(x = 0) = C_1 + C_2 = \varepsilon_{s0} \tag{4.10}$$

Equations (4.8), (4.9), and (4.10) have three unknowns, i.e., C_1 , C_2 , l_{D1}. The system is solved step by step, for any value of the controlling variable, ε_{s0}, in order to define the distribution of bar strains, slip values and the length of disturbed region, l_{D1}. The next crack is at $x_{cr,2}$: the crack may be either inside l_{D1} (governed by bond equation) or it may happen in the undisturbed region and will be evaluated based on the flexural theory. Specifically, if the next crack occurs:

a) inside the disturbed region: In this case, $x_{cr,2}$ can be found if the force transferred through bond to the concrete cover exceeds the tensile resistance of the effective area of concrete cover engaged in tension:

$$E_s A_{s1}(\varepsilon_0 - \varepsilon(x)) > f_{ct} A_{c,eff} \quad \text{where} \quad A_{c,eff} = b\,(2c_1 + D_b) - A_s \tag{4.11}$$

b) in the undisturbed region: Here, $x_{cr,2}$ is calculated from the following equation.

$$\varepsilon(x_{cr,2}) = \frac{M_0.y_g}{E_c.I_g}\left(1 - {}^{x_{cr,2}}/_{L_s}\right) = \varepsilon_{c,cr} \tag{4.12}$$

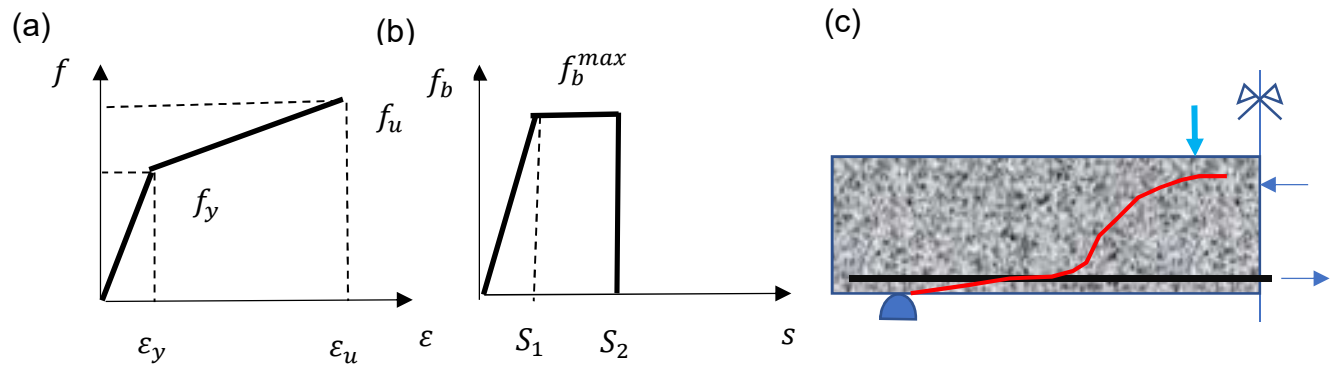

Figure 4.5: (a) General stress strain diagram for steel and (b) Bond-slip relationship; (c) Common shear failure crack pattern of beams without stirrups

After localization of the second crack, the new disturbed region, l_{D2}, which extends from the second crack location, $x_{cr,2}$, is calculated. The process is repeated until no additional primary cracks can form as the moment increases: this stage corresponds to stabilization of cracking. From this stage on, until failure, the anchorage solution (elaborated in detail in the following section) is used over the entire length, L_b, which is measured from the critical section to the end of the bar length (the boundary condition at the free end of the bar is, $\varepsilon(L_b) = 0$).

Failure occurs when either (a) the strain at the critical section ε_{s0} exhausts the ultimate strain of the M-ε diagram, or (b) the total disturbed length L_D exceeds the available development length of the bar in the shear span, taken here as $L_s + h_{hook}$. After creation of the last primary crack, it is necessary to check whether the bar force required for flexure at the last crack, $(A_s E_s \varepsilon_{s,cr})$ can be equilibrated by the bond force along the available development length of the bar, to be evaluated from the bond solution. If the remaining length is shorter than expected to carry the bar force through bond, failure will occur by splitting along the bar.

4.4.1 Anchorage Solution

The purpose here is to get the solution of field equation of the bond (Eq. (4.4a) and (4.4b)) for a bar anchorage. Considering the bond-slip relationship curve (Figure (4.4b)), the equation of bond should be solved for three different cases:

- Case (i): when bond developed in the bar is within the elastic range of the assumed bond-slip law ($s < s_1 = s_y$)
- Case (ii): when bond developed in the bar is within the plateau segment of the bond-slip law ($f = f_{b,max}, s_1 < s < s_2$)
- Case (iii): when bond developed in the bar is in the descending part of the bond-slip law (debonding stage, ($s > s_2$)
- Case (iv): when the main bar reaches yielding accompanied with bond degradation to its residual value

Table 4.1: Solving bond equation for different scenarios (Tastani and Pantazopoulou 2013a)

Case(i)	
$\varepsilon(x) = \frac{\varepsilon_0}{1-e^{-2\omega L_b}} (e^{-\omega x} - e^{\omega x - 2\omega L_b}) < \varepsilon_{sy}$	(4.13)
$s(x) = \frac{\varepsilon_0}{\omega (1-e^{-2\omega L_b})} (e^{-\omega} + e^{\omega x - 2\omega L_b}) < s_y$	(4.14)
$f_b(x) = \left(\frac{f_b^{max}}{s_1}\right).s(x) < f_b^{max}$	(4.15)
$\varepsilon_{el}^{(i)} = s_y \omega \frac{1-e^{-2\omega L_b}}{1+e^{-2\omega L_b}}$	(4.16)
ε_0 is bar strain at the critical section (under the point load), and L_b is the available anchorage length.	
Case (ii)	
$0 \le x \le l_p$ (l_p the length of bond plastification)	

$$\varepsilon\,(x) = \varepsilon_0 - \frac{4\,f_b^{max}}{E\,D_b}\,x \tag{4.17}$$

$$s(x) = s_1 + 0.5\,(l_p - x)(\varepsilon(x) + \varepsilon_{el}^{ii}) \tag{4.18}$$

$$f_b(x) = f_b^{max} \tag{4.19}$$

$l_p \le x \le L_b$

$$\varepsilon(x) = \frac{\varepsilon_{el}^{ii}}{1-e^{-2\omega(L_b - l_p)}}\left(e^{-\omega(x - l_p)} - e^{\omega(x - l_p) - 2\omega(L_b - l_p)}\right) \tag{4.20}$$

$$s(x) = \frac{\varepsilon_{el}^{ii}}{\omega\left(1-e^{-2\omega(L_b - l_p)}\right)}\left(e^{-\omega(x - l_p)} + e^{\omega(x - l_p) - 2\omega(L_b - l_p)}\right) \tag{4.21}$$

$$f_b(x) = \left(\frac{f_b^{max}}{s_1}\right).s(x) < f_b^{max} \tag{4.22}$$

Where:

$$\varepsilon_{el}^{(ii)} = \varepsilon_0 - \frac{4\,f_b^{max}}{E\,D_b}\,l_p \tag{4.23}$$

To find l_p, continuity of strain and slip ($s\left(x = l_p\right) = s_1$) should be satisfied at $x = l_p$. So, we must solve below equation iteratively.

$$s_1 - \left(\varepsilon_0 - \frac{4\,f_b^{max}}{E\,D_b}\,l_p\right)\frac{\left(1+e^{-2\omega(L_b - l_p)}\right)}{\omega\left(1-e^{-2\omega(L_b - l_p)}\right)} = 0 \tag{4.24}$$

Onset of debonding, corresponding to the end of bond plastification, is when we have $s\,(x = 0) = s_2$

Therefore, we have:

$$s_2 - \left(\varepsilon_0 - \frac{4\,f_b^{max}}{E\,D_b}\,l_p\right)\frac{\left(e^{\omega(l_p)} + e^{-\omega(l_p) - 2\omega(L_b - l_p)}\right)}{\omega\left(1-e^{-2\omega(L_b - l_p)}\right)} = 0 \tag{4.25}$$

The ultimate strain at the critical section, $\varepsilon_{0,u}$, is evaluated as

$$\varepsilon_{0,u} = 2\frac{s_2 - s_1}{l_p} - \varepsilon_{el}^{(ii)} \tag{4.26}$$

Case (iii)

Onset of Debonding

When debonding starts, the ultimate strain, $\varepsilon_{0,u}$, propagated over the debonded length, l_r.

Slip at the critical section is calculated as the integral of strain over the debonded length.

$$s_{deb} = s_2 + \varepsilon_{0,u} l_r \quad (4.27)$$

From Eq. (4.18), $s(l_r) = s_u$ should be satisfied. Therefore, a quadratic equation is created, and the solution would give us two values for l_p. The value that satisfies the requirement of

$l_p + l_r < L_b$ is the final answer.

$$s(l_r) = s_u = s_1 + 0.5\,(l_p)(\varepsilon_{0,u} + (\varepsilon_{0,u} - \frac{4 f_b^{max}}{E D_b} l_p)) \quad (4.28)$$

$$l_p = \left[\varepsilon_{0,u} \pm \sqrt{{\varepsilon_{0,u}}^2 - \frac{8 f_b^{max}}{E D_b}(s_2 - s_1)}\right] \Big/ \frac{4 f_b^{max}}{E D_b} \quad (4.29)$$

Also $s(l_r + l_p) = s_1$, therefore from Eq. (4.21) we have:

$$s_1 - (\varepsilon_0 - \frac{4 f_b^{max}}{E D_b} l_p) \frac{\left(1 + e^{-2\omega(L_b - l_p)}\right)}{\omega\left(1 - e^{-2\omega(L_b - l_p)}\right)} = 0 \quad (4.30)$$

Case (iv)

$$\varepsilon_0 > s_y \omega \frac{1 - e^{-2\omega L_b}}{1 + e^{-2\omega L_b}} \quad (4.31)$$

$0 \le x \le l_r$

$$\varepsilon(x) = \varepsilon_0 - \frac{4 f_b^{res}}{E_{sh} D_b} x \quad (4.32)$$

$$s(x) = s_u + 0.5\,(l_r - x)(\varepsilon(x) + \varepsilon_{sy}) \quad (4.33)$$

$$f_b(x) = f_b^{res} \quad (4.34)$$

$l_r \le x \le l_r + l_p$

$$\varepsilon(x) = \varepsilon_{sy} - \frac{4 f_b^{max}}{E_s D_b}(x - l_r) \quad (4.35)$$

$$s(x) = s_y + 0.5\,(l_r + l_p - x)(\varepsilon(x) + \varepsilon_{el}^{(iv)}) \quad (4.36)$$

$$f_b(x) = f_b^{max} \quad (4.37)$$

$l_r + l_p \le x \le L_b$

$$\varepsilon(x) = \frac{\varepsilon_{el}^{(iv)}}{1 - e^{-2\omega(L_b - l_p - l_r)}}\left(e^{-\omega(x - l_p - l_r)} - e^{\omega(x - l_p - l_r) - 2\omega(L_b - l_p - l_r)}\right) \quad (4.38)$$

$$s(x) = \frac{\varepsilon_{el}^{(iv)}}{\omega\left(1 - e^{-2\omega(L_b - l_p - l_r)}\right)}\left(e^{-\omega(x - l_p - l_r)} + e^{\omega(x - l_p - l_r) - 2\omega(L_b - l_p - l_r)}\right) \quad (4.39)$$

$$f_b(x) = \left(\frac{f_b^{max}}{s_1}\right).s(x) < f_b^{max} \quad (4.40)$$

Where

$$\varepsilon\left(l_r + l_p\right) = \varepsilon_{el}^{(iv)} = \varepsilon_{sy} - \frac{4 f_b^{max}}{E_s D_b}(l_p) \quad (4.41)$$

4.4.2 Accounting for Boundary Conditions

Tests are conducted with different construction details which may create different boundary conditions to the problem stated above. In order to approximate the distribution of bar strains over the disturbed length along the shear span, the proper boundary conditions should be selected. For example, if the tension reinforcement is anchored properly either by using stirrups beyond the supports or using forged headed bars, then the enhanced bond strength that may be mobilized in that segment could suffice to fully develop the bar. In this case the bond equation is solved considering that the available anchorage length provides for zero slip in the end – usually, these are cases where pure

shear failure has been observed, provided there is no local failure under the hook or head to pre-empt the development.

4.5 Application of the Proposed Model to Sample Cases from the ACI database

To illustrate the application of the proposed methodology, two examples have been considered. The first beam is specimen S_0 from the study of Islam et al.(1998). The second specimen is $PLS300$ from the study of Quach (2016). The program to conduct the iterative algorithm was written in R (R Core Team 2015), which is similar to MATLAB. A sample R Code is presented in Appendix A.

Specimen dimensions and loading setup for the two examples considered are shown in Figure (4.5). The moment-tension steel strain relationship calculated from flexural analysis using Response2000 (Bentz and Collins 1998) of the critical section is depicted in Figure (4.6). The peak bond strength was taken as $1.25\sqrt{f_c'}$ on account of the absence of confinement of the shear span. The detailed properties of the bond-slip law considered for the two examples of the study are listed in Table 4.2.

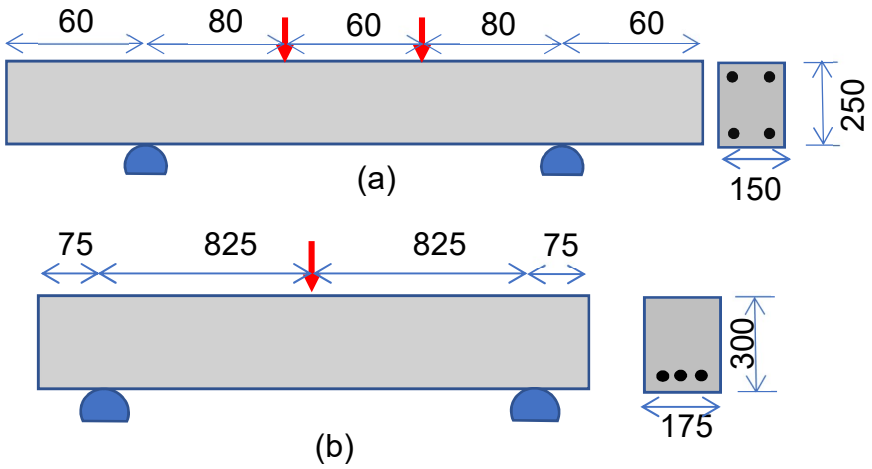

Figure 4.6: Details of (a) Specimen S0 (Islam et al. 1998) and (b) Specimen PLS300 (Quach 2016)

Table 4.2: Detail properties of specimens under study

	$f_c'\ (MPa)$	$f_y\ (MPa)$	$D_b (mm)$	$c\ (mm)$	$f_b (MPa)$	$s_1 (mm)$	$s_2 (mm)$
S0	24.6	350	20	33	6	0.1	0.25
PLS300	40	573	10	31	8	0.6	2.4

Discussion of Analysis Results: A moment-curvature analysis was conducted for the critical cross section (section under the point load) of the two specimens, and the resulting strains in the tension reinforcement were calculated (see plots of moment strain relationships in Figure (4.6a) and (4.6b) for the two specimens, respectively). Furthermore, the anticipated shear strengths were calculated using the models listed in Table 4.3.

Table 4.3: Calculated shear strength values for specimens considered in the study (values in KN)

Specimen ID	Experiment	ACI	Collins	Cladera	Frosch	Li	Park	Reineck
S0	47.5	25.9	28.6	35.31	30	28.14	59.77	31.75
PLS300	47.7	48.5	51.23	33.6	27.15	30	43.6	32.05

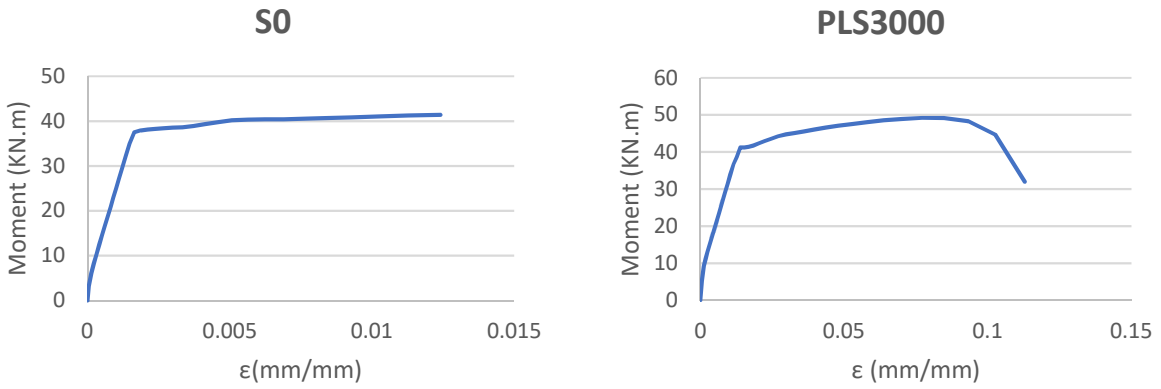

(a) (b)

Figure 4.7: Calculated moment – tension steel strain relationship at the critical crack (a) specimen S0 (b) specimen PLS300

Specimen S0: In applying the algorithm described in the preceding it was found that the first crack in the beam occurs at maximum moment of *2.36 KN.m* under the point load. This is the starting point in the x axis for the analysis below. Here the concrete cracking strain is, ε_{cr} = *0.00007*, assuming that the concrete modulus of elasticity is, E_c=4500√24.6MPa =23.2 GPa. Adjacent to the crack, the flexural theory is not valid and the disturbed length (l_{D1}) is estimated using the bond equation (Eq. (4.8), (4.9), and (4.10)). With increasing strain at the critical section (under the point load) in every step, the disturbed length is calculated and the possibility of the creation of a new crack is checked (Eq. (4.11) and (4.12)). In this example, the second crack happens at ε = 0.0002 outside the disturbed length of $l_{D1} = 115.83\ mm$ at $x_{cr2} = 554.01mm$ when the maximum moment is *7.67MPa*. By further increasing the strain in tension reinforcement, at ε = 0.0003, two different disturbed regions are created; $0\ to\ x_{cr2} = 554.01mm$ and $x_{cr2}\ to\ l_{D2} = 974.75mm$. In this example, after calculation of l_{D2}, it is evident that disturbed region extends beyond the support and therefore the entire length from x_{cr2} to the end of the bar length is behaving as an anchorage and the anchorage solution is implemented (Tastani and Pantazopoulou 2013a, 2013b). With further investigation of possibility of a crack forming between existing cracks and by increasing the strain up to ε = 0.0007, no new crack can be found. This is the stage of stabilization of cracks. At this stage, the bar slip reaches the elastic bond limit ($s(x) = S_1 = 0.1mm$) at the location of the first crack ($x = 0$). For the sake of simplicity of the mathematical problem, at this stage, the entire anchorage length from the critical section to the end of the bar will be treated as an anchorage. At the strain ε = 0.000775, solving the anchorage solution for entire length ($L_b = 1400$), the bar exceeds the elastic bond limit ($s(x) > s_1 = 0.1mm$). In this stage bond plasticisation begins. By further increasing of the strain, length of l_p , where the slip at the critical section (at the start of the anchorage solution) of the bar, exceeds s_2, is found to mark the onset of debonding. From the calculations, this occurs at a bar strain of $\varepsilon_s = 0.0016$ in the critical section corresponding to a bar stress of 320MPa; from Figure (4.6a), the moment at the center of the span is equal to *37 kN.m* (at a shear force = $V_c = 44.25\ KN$). Beyond attainment of the limiting slip, debonding begins

from the loading point towards the support (manifested by splitting along the cover), which limits the load carrying capacity of the beam, leading to failure. The shear force sustained according to the experimental report was 47.5 KN, which is very close to the calculated value. Note that this value does not correlate with the estimates obtained from the six candidate models of C445 (Table 3.1) as listed in Table 4.3. Distributions of strains as debonding propagates from the critical section towards the end of the available bonded length are given in Figure 4.7.

Specimen PLS300: Applying the same algorithm to the second example, it was found that the first crack occurs at maximum moment of *4.98 KN.m* (ε_{cr} = *0.000067*, assuming the modulus of elasticity E_c=4500√40MPa =28.5 GPa) under the point load. Adjacent to the crack, the associated disturbed region l_{D1} is calculated (Eq. (4.8), (4.9), and (4.10)) and the distribution of the strain in the tension bar will be estimated using Eq. 4.4. With increasing strain at the critical section (under the point load) in every step, at $\varepsilon = 0.001$, a disturbed length of $l_{D1} = 744.38mm$ is found and using Eq. (4.11) and (4.12), the second crack will be found inside the disturbed region at $x_{cr2} = 432.90mm$. By further increasing of the strain in tension reinforcement, at $\varepsilon_s = 0.002$, the second disturbed region, $l_{D2} = 661.62mm$, will be created and it is evident that the disturbed region extends beyond the support and therefore the entire length from x_{cr2} to the end of the bar length is behaving as an anchorage and the anchorage solution is implemented. With further investigation of possibility of crack inside the second disturbed region and increasing the strain up to ε = 0.0025, no new crack could be found. This is the stage of stabilization of cracks. At this stage the bar slip reaches the elastic bond limit ($s(x) = S_1 = 0.1mm$) at the location of the first crack ($x = 0$). For the sake of simplicity of the mathematical problem, at this stage, the entire anchorage length from the critical section to the end of the anchorage, $L_b = 1004mm$, will be treated as an anchorage. From the anchorage solution, at the strain ε = 0.003175, solving for the entire anchorage length ($L_b = 1004mm$), the bar exceeds the elastic bond limit ($s(x) > S_1 = 0.1mm$). In this stage bond plasticisation occurs and the length of l_p over which slip at the critical section (at the start of the anchorage solution) of the bar exceeds S_2, is found to mark the onset

of debonding. Based on the calculations, this occurs at a bar strain in the critical section, of $\varepsilon_s = 0.011$ corresponding to the moment at the center of the span equal to *37 kN-m* (at a shear force = $V_c = 44.85\ KN$). Beyond the attainment of the limiting slip, debonding begins from the loading point towards the support (manifested by splitting along the cover), which limits the load carrying capacity of the beam, leading to failure. The shear force sustained according to the experimental report was 47.7 KN, which is very close to the calculated value.

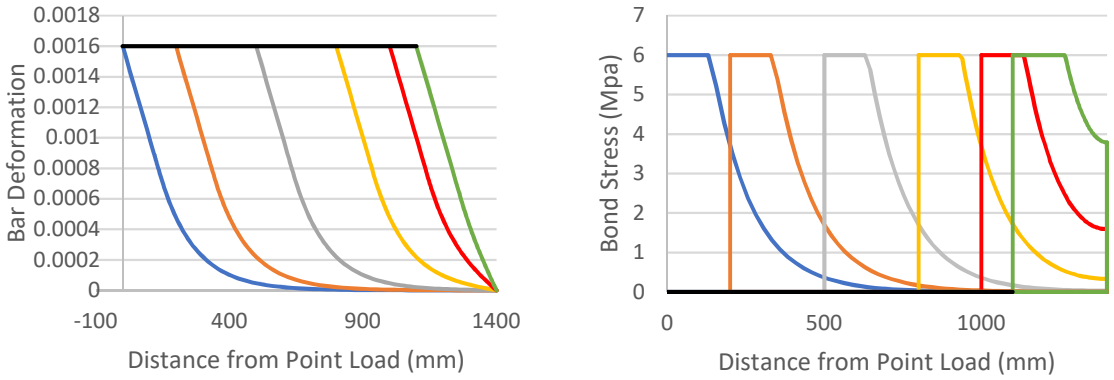

Figure 4.8: Distributions of bar strain and bond stress for beam S0 as debonding propagates from the critical section towards the end of the available bonded length

CHAPTER 5: EXPERIMENTAL PROGRAM

5.1 Introduction

Today, the state of the art is focused on self-consolidated strain hardening fiber-reinforced cementitious composites with fine aggregates demonstrating great crack control, high ductility and improved durability performance. However, few documented test evidences are available regarding the performance of Strain Hardening Fiber Reinforced Cementitious Composites (SHFRCC) when used in structural members. Most of the emphasis has been placed on Ultra High Performance Concrete (UHPC), a version of SHFRCC which is reinforced with steel fibers and exceeds the compressive strength limit of 120 MPa and a tensile strength in excess of 10 MPa (CSA-S8 ANNEX 2017). However, equally useful in construction – particularly for repair of structures, the use of synthetic-fiber SHFRCC, with compressive strengths in the range from 50-100 MPa and sustained tensile strength in the order of 5-10 MPa – this class of concrete is more immune to corrosion, is more sustainable and compatible with existing substrates. Since the technology of SHFRCC is a relatively recent development in the field of concrete materials, there are very few, under-correlated design expressions for its use in structural design. While in normal concrete the contribution of concrete in tension is neglected in all established design procedures, in the case of SHFRCC, promising results have been published indicating the effectiveness of fibers in bridging the cracks and showing post cracking resilience and remarkable tensile deformation capacity (Li 2003, Paegle and Fischer 2016, Georgiou and Pantazopoulou 2016). Thus, SHFRCC presents a great opportunity for substituting bar-type detailing reinforcement with this new type of material and therefore there is a need to quantify the strength of this material in shear, bond with steel, and flexure. Shear is the particular focus of this thesis, and towards this objective an experimental program is designed to provide a basis for development of design rules which are prerequisite for introduction of these novel materials in new construction.

Shear/Flexure combinations are the most common states of stress in reinforced concrete members. For this reason, the first part of the experimental program is dedicated to study of shear in SHFRCC using push-off specimens and the second part focuses on the

behavior of SHFRCC in combined shear and flexure in concrete beams. In order to cast the specimens, a SHFRCC material with synthetic fibers is developed in the structural laboratory of York University inspired by previous studies done by Li (2009) and Georgiou (2017).

In this chapter, a description of the experimental work performed to study the behaviour of SHFRCC fabricated in-house is presented. The work was done in two phases: A Preliminary and a Main phase. All of the tests were performed during a period of about 16 months starting from June 2017 up until October 2018 in the Structural Laboratories of Lassonde School of Engineering at York University.

This chapter touches on the selected mix design, material properties, and casting procedure. Section 5.6 and 5.7 include a discussion of the preliminary and main experimental program and all mechanical tests done to study the SHFRCC. Results of the experiments are covered in Chapter 6.

5.2 Mix Design Selection

At the onset of this work, it was decided to develop a SHFRCC mix at the Structures and Materials laboratory inspired from previous studies in this area. Lepech and Li (2009) designed concrete mixes for large scale casting of Engineered Cementitious Composites (ECC). Georgiou and Pantazopoulou (2016) reproduced this mix design with modifications in the materials used considering the availability of different material qualities in Europe (For example they used Cement EN 197-1 Cem II / A-M 53 (L-S) 42.5 R which contains silica fume and slag, and a special imported washed sand with predefined gradation and maximum grain size of 300μm); they obtained favorable results producing Strain Hardening Fiber Reinforced Cement Composites (SHFRCC) with dtex-39 PVA fibers (Kuralon K-II). In the present work we began with the ECC-M45 mix design (Lepech and Li 2009b), with the characteristic summarized in Table 5.1, however also requiring modifications on account of the availability of local materials, and the use of larger diameter PVA fiber (dtex-100 Kuralon K-II imported from Japan).

Table 5.1: Original ECC mixture proportions by weight for ECC M45 (Lepech and Li 2009b)

Mixture designation	Cement	Fly ash	Sand	Water	HRWR*	Fiber Volume %
M45	1	1.2	0.8	0.56	0.012	0.02

*High-Range Water Reducer

5.3 Materials

The goal of the experimental work in this research was to study the shear behaviour of a sustainable Self Consolidating Fiber Reinforced Concrete with strain hardening response under tension and to evaluate the improved performance of the concrete effected by addition of fibers. To find the best choice of local materials to make the mix, different types of cement, sand, and superplasticizer were used and tested.

- Cement

Two different types of cement, General Use (GU) and Portland-Limestone (GUL) cement, were used. The reason behind using the GUL was to increase the workability of the mix and to get a more impermeable and dense concrete. In order to get the desirable high strength concrete, silica fume (SF) and slag were also added to the GUL. The cement used in this project was donated by the CRH cement company.

- Fly Ash

Class F Fly Ash is a waste by-product resulting from combustion of anthracite or bituminous coal for the production of electricity. It may also be obtained from burning sub-bituminous coal and lignite, whereas in oil-producing countries where fossil fuel is burned to produce energy Fly-ash is also the by-product of the process, albeit it is not considered an equally effective cement replacement as common fly-ash (Georgiou 2017). Type F fly ash with particle size of less that 50 microns in size was used in present study. Fly-ash particles are spherical and glassy, and they do exhibit pozzolanic properties. Fly ash supplied by Lafarge was used for this program.

- Silica Fume

Silica fume is a by-product of the production of silicon and ferrosilicon alloy. It is an ultrafine powder with spherical shape particles (average particle diameter of 150nm) (Holland 2005). Dry densified silica fume was used here to create a ternary concrete mixture and get higher compressive strength. Silica fume supplied by BASF company was used for the project.

- Slag

Ground Granulated Blast Furnace Slag (GGBFS) is a by-product of iron and steel-making formed by rapidly chilling of the molten iron blast furnace slag in water and ground to Portland cement fineness (Pal et al. 2003). It was also used here as part of the cementitious admixture to get higher ultimate strength. GGBFS supplied by St. Mary's company was used for this project.

- Sand

Six different types of sand have been tried in the preliminary phase of the project in order to find the proper locally sourced sand so as to produce PVA-Strain Hardening Fiber Reinforced Cementitious Composite (SHFRCC). The grain size distribution is shown in Figure 5.1.

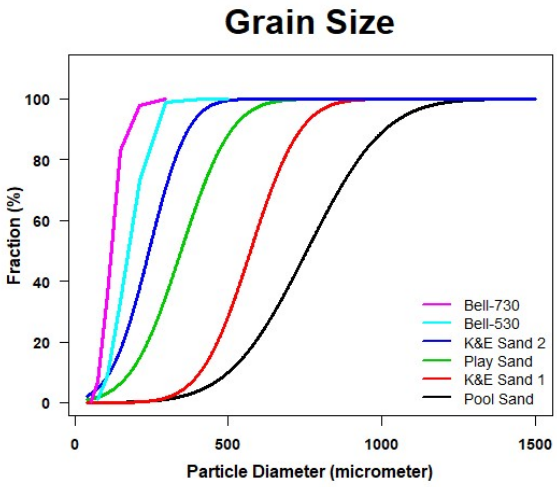

Figure 5.1: Grain Size distribution of 6 different sands used in the trial mixes. The sand that was kept for the study is the one denoted as Bell-730.

- Polyvinyl Alcohol fibers (PVA)

Polyvinyl Alcohol (PVA) synthetic fiber was used as mass reinforcement. The commercial type is Kuralon K-II RECS100 × 12 a product based on polyvinyl alcohol (PVOH) resin which was imported from Japan for the needs of the project. These synthetic fibers have a length of 12mm, a diameter of 100 dtex ($\sim 0.1\ mm$), density of 1100 $^{kg}/_{m^3}$, a tensile strength of 1235 MPa, and Young's Modulus of 29 GPa with elongation strain capacity of 12.5%.

- Reinforcing Steel

Steel reinforcement was only used in the full-scale beams. All other specimens did not have any conventional steel reinforcement. For both beam specimens, 3-15M steel bars were used with a nominal yield strength of 400 MPa.

- Fiber Reinforced Polymer (FRP)

For the needs of the tests, where possible premature failures were likely to occur outside the test region of the push off specimens, local jacketing with a unidirectional carbon fiber fabric (SikaWrap Hex- 230c supplied by Sika-Canada) was used to reinforce in tension the zones of concern. The fiber properties are shown in Table 5.2.

Table 5.2: Fiber properties of SikaWrap Hex-230c

Fiber Properties	
Tensile Strength (GPa)	5.45
Tensile E-modulus (GPa)	230
Elongation	1.5%
Density ($^{gr}/_{cm^3}$)	1.8
Area weight ($^{gr}/_{m^2}$)	228
Nominal fiber thickness (mm)	0.13

The carbon fiber fabric was used in conjunction with Sikadur-330 epoxy laminating resin which is a two-component epoxy resin.

- Superplasticizer

MasterGlenium 7700 and 3030 which is a high-range water-reducing admixture and is based on the next generation of the polycarboxylate technology were used in this experimental program. The superplasticizers were supplied by the BASF Company.

5.4 Coating of PVA Fibers

PVA fiber is a unique polymer with the molecules structure showed in Figure 5.2. As can be seen, these fibers have free hydroxyl groups (-OH) in their molecule chain which cause a strong bond with the hydrates of the surrounding cementitious matrix. One of the main design goals behind the production of Engineered Cementitious Composite (ECC) is to achieve higher ductility which is achievable through fiber pull-out situation rather than local rupturing of fibers at cracks. This objective is counteracted by the high chemical bond between fibers and surrounding matrix, leading to fiber rupture under high tensile stress which may lead to higher strength at a cost of significantly impaired ductility in concrete. To avoid the fiber rupturing due to the strong chemical bond, researchers suggested to coat the fibers' surface with surfactants or debonders (Li et al. 2002, Georgiou et al. 2016). Selection of the right type and amount of coating agent leads to an optimum composite behavior. Otherwise, either bond will be still too high which leads to fiber rupturing situation or it would become too low and cause significant loss of tensile strength past the onset of cracking.

In this research, wherever necessary, fibers are coated with a foaming agent that creates air around the fibers and reduce the bond between fibers and surrounding cementitious matrix following the procedure suggested by Georgiou (2017). To preclude production of excessively lightweight concrete with impaired mechanical strengths, a defoamer was added during mixing of the cementitious material so as to counteract any foamer material was diluted by the water of the mix during the addition of fibers.

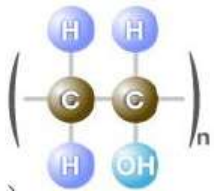

Figure 5.2: Molecular structure of PVA fibers

5.4.1 Types of Coating

Two different coating agents were used in this research: A Liquid Foamer (MasterCell30) and A Powder Foamer (MasterCell25). From observation of the coated fibers in Figure 5.3, it was concluded that in the case of liquid foamer the bond between fibers was effectively reduced and fibers were no longer bundled, whereas the powder foamer was not effective enough. Therefore, it was decided that only the liquid foamer would be used in the forthcoming experiments.

5.4.2 Coating Procedure

Fibers were coated several days prior to the casting to let them dry completely. The coating agent and a small percentage of water were mixed together for 2-3 minutes until a thick foaming paste is created. Then the fibers and the thick mixture were mixed together in a mixer for 30 minutes. As reported by Georgiou (2017), for 1000gr of fiber, 100ml of water and 66gr of foamer was used. The exact quantity of the material used is reported in Table 5.5.

(a) (b)

Figure 5.3: a) PVA fibers after coating with powder foamer (left picture) and liquid foamer (right picture) b) mixer while coating PVA fibers

5.5 Mixing Procedure

The full process of concrete mixing takes about 30 minutes in total. To prepare the mix, all dry powders (cement, silica fume, slag, fly ash, and sand) were mixed together for 1-2 minutes. Then the weighted superplasticizer (MasterGlenium 7700 or 3030) was diluted into half of the water and the fluid was added slowly to the mixer (2-3 minutes) – mixing continued until no clumps were visible. After complete change of color of the powder, fibers were dispersed slowly to the mix while the mixer was working (5-10 minutes). Lastly, the other half of water was added to the mixer slowly until all fibers were distributed evenly. In case of using coated fiber, a small amount of defoamer must be diluted to the second half of the water before adding to the mix. The resulting self-consolidating cementitious composite (SCC) was poured into specified molds without using any vibrator and the surface was covered with either plastic bag or plexiglass sheets. Specimens without reinforcements were kept under water until the day of test and those with reinforcement were wrapped under wet burlap that was rewetted regularly during curing and until the time of testing.

5.6 Preliminary Experiments

The main goal of the preliminary experimental program was to develop and proof-test a strain hardening fiber reinforced cementitious composite (SHFRCC) in the structural lab of Lassonde School of Engineering and to finalize the mix design for the main phase of the experimental study. All different variables that might affect the composite were considered and studied in the preliminary phase of experimental work.

5.6.1 Experimental Parameters

At the outset of this work, it was determined that there are a number of parameters that would affect the mix, but no adequate literature was found documenting this effect specifically on PVA-SHFRCC. The list of variables is presented here in Table 5.3. Regarding the content ratio of slag and silica fume, two different percentages were considered in order to emulate the European type CEM42.5, namely (4% & 8%), or (8% &20%), respectively. Six different types of sand were tested as listed in Table 5.4.

The effect of all variables was investigated through casting of 39 different mixes. Table 5.5 shows mix designs for a representative number of tests. The complete mix design table is given in Appendix B.

Figure 5.4: Planetary mixer, fixed concrete mixer machine, and concrete molds used in the experiment

Table 5.3: Effective variables

#	Variables
1	Types of cement
2	Types of sand
3	Combination of different sands
4	Presence/ Percentage of Slag and Silica Fume
5	Deduction of Silica fume and Slag from Cement or Fly ash
6	Coated or uncoated fiber
7	Amount of Defoamer
8	Types of superplasticizer

Table 5.4: Different types of sand used in this research

Sand Type Number	Sand Name	Max. grain size (mm)
1	Play Sand	1.3
2	Pool Sand	1.5
3	K&E-big	1
4	K&E- small	0.9
5	McKenzie 530	0.4
6	McKenzie 730	0.3

Table 5.5: Mix Design for Representative Preliminary Tests

Series Name	Date	Fiber (gr)	Defoamer (gr)	Cement		Sand		Fly Ash (Kg)	Slag (gr)	Silica Fume (gr)	W/C	SP (gr)
				Type	Weigh (Kg)	Type	Weigh (Kg)					
B27	Jan. 17th	22.75	10	GUL	0.350	4	0.389	0.583	39.2	98	0.25	18
B28	Jan. 26th	22.75	-	GUL	0.350	5	0.389	0.583	39.2	98	0.25	18
B29	Jan. 26th	22.75	-	GUL	0.350	5	0.389	0.583	39.2	98	0.25	5.85
B30	Jan. 26th	22.75	-	GUL	0.350	4	0.389	0.583	39.2	98	0.25	18
B31	Jan. 26th	22.75	-	GUL	0.350	4	0.389	0.583	39.2	98	0.25	5.85
B32	Jan. 29th	22.75	-	GUL	0.350	5	0.389	0.583	39.2	98	0.25	11.7*
B33	Jan. 29th	22.75	-	GUL	0.350	5	0.389	0.583	39.2	98	0.25	5.85*
B34	Feb. 12th	22.75	-	GUL	0.350	5	0.389	0.583	39.2	98	0.25	8.7
B35	Feb. 12th	22.75	-	GUL	0.487	5	0.389	0.583	-	-	0.25	8.7
B36	Feb. 23rd	22.75	2.26	GUL	0.350	5	0.389	0.583	39.2	98	0.25	8.3
B37	Mar. 2nd	22.75	4.67	GUL	0.350	5	0.389	0.583	39.2	98	0.25	8.3
B38	Mar. 5th	22.75	4.67	GUL	0.350	6	0.389	0.583	39.2	98	0.25	8.3
B39	Mar. 5th	22.75	-	GUL	0.350	6	0.389	0.583	39.2	98	0.25	8.3

5.6.2 Experimental Tests Performed on Fresh Cementitious Composites

5.6.2.1 Flow Test

According to ASTM C1856/C1856M, Fabricating and Testing Specimens of Ultra-High-Performance Concrete, to test the flowability of the fresh concrete a flow table which meets the requirements of the ASTM C230/C230M shown in (Figure 5.5) was used. The mold was filled in a single layer. Then it was lifted, and the fresh concrete was let to flow laterally on the table for 2 minutes. The diameter of concrete was measured along the line of the maximum and minimum diameter. The flow value would be the average diameter. The results are presented in Chapter 6.

Figure 5.5: Flow table

5.6.3 Experimental Tests Performed on Hardened Cementitious Composites

5.6.3.1 Specimen Preparation and Casting

For preliminary experiments, prisms, cubes and cylinder specimens with dimensions specified in Table 5.6 were used. After a mixing time of about 30 minutes, the resulting Self Consolidating Concrete (SCC) fresh mix was poured into molds in one layer without using any vibration. Specimens were kept under plastic or plexiglass sheets for 24-48 hours and then demolded and cured under water until the day of the mechanical tests.

Table 5.6: Specimen Size

Specimens	Dimensions (mm)
Cube	50×50×50
Cylinder	100×200
Prism	50×50×280

5.6.3.1.1 Uniaxial Compression Test

Cube specimens with size of 50×50×50 mm and 100mm-diameter by 200mm-high cylinders were tested under uniaxial compression with a test rate of 0.259 MPa/s in a 3000 KN capacity compression tester for cubes and cylinders (PILOT Frame, Figure 5.6) to evaluate the compression strength of the different batches.

Figure 5.6: Compression Machine-Controls Group

5.6.3.1.2 Flexural Beam Tests

Three-point and four-point bending tests were conducted using the 600KN MTS universal Testing Machine (Figure 5.7). The results of all preliminary tests are reported in Chapter 6. In the case of specimens comprising the same matrix as the FRC specimens but with no fibers, failure was sudden, and the specimen was broken down in two pieces.

However, fiber-reinforced specimens showed very good ductility maintaining their integrity after removal from the test frame.

Figure 5.7: 600 KN MTS universal Testing Machine and a 3-point bending test for a prism

5.7 The Main Experiment

Comparing the results of all different mixes (B1-B39) in the preliminary phase of experimental program the best result was achieved for the case where the #730 McKenzie sand was used (this sand contained the smallest maximum grain size, of 300μm). In this case (mix B39 in Table 5.5), even without coating of fibers, fibers pulled out (rather than rupturing) and multiple cracking and strain hardening behaviour was evident. However, for all other types of sand, without coating of the fibers, strain softening, and localization of deformation occurred in a single crack in the middle span and fibers bridged the crack until they ruptured while the load was increasing. Although with the coating of fibers it was possible to affect the behaviour inducing multiple cracking and strain hardening in tension even when other types of sand were used, yet, for sake of simplicity, the preference was to avoid the coating procedure.

5.7.1 Main Concrete Casting

Casting of specimens for the main experimental phase was done in two different days. In the first day three different batches (M1-M3) were mixed, each 40 L, and in the second day two batches (M4-M5) of 40 L were cast as specified in Table 5.7.

Table 5.7: Mix design for the main phase of the experiment

Series Name	Fiber (Kg)	Cement (Kg)	Fly Ash (Kg)	Silica Fume (Kg)	Slag (Kg)	Sand (Kg)	Water (Kg)	SP (Kg)	Total Volume (L)
M1-M5	1	16	26.7	4.4	1.8	17.8	12.44	0.4	40

As explained previously, to prepare the mix, all dry powders (cement, silica fume, slag, fly ash, and sand) were mixed together for 1-2 minutes. Then the pre-weighted amount of superplasticizer was diluted into half of the water and was added slowly to the mixer (2-3 minutes) and mixing continued until no clumps were visible. After complete change of color of the mixed powders, fibers were dispersed slowly to the mix while the mixer was working (5-10 minutes). Lastly, the remaining half of the water amount was added to the mixer slowly until all fibers were distributed evenly. The resulting self-consolidating cementitious composite was poured into specified molds (Figure 5.8). All fresh specimens were covered with plastic sheets and after two days they were demolded and those without internal reinforcements were kept inside water whereas those with reinforcing steel were kept under wet burlap (Figure 5.9).

Figure 5.8: Mixing sequence of the Strain Hardening Cementitious Composite

Figure 5.9: Curing of the specimens under water

5.7.2 Digital Image Correlation (DIC) Analysis

A measuring technique known as Digital Image Correlation (DIC) was used to record the deformations of different specimens through processing of images captured on the specimen's surface (for this purpose a speckle-pattern coloring was applied to all visible surfaces). A remotely-controlled camera system was placed taking pictures every 5 seconds while the Data Acquisition (DAQ) System was recording the load-displacement data with a 10 Hz frequency (10 data per second). The camera and Data Acquisition System were synchronized, and they were both started at the same time. Collecting all pictures and having the load-time data from DAQ, a selection of pictures for each specimen (10-20 pictures representing 10-20 points along the load- displacement curve) were analysed using the GeoPIV-RG (2015) software which involves using MATLAB to process the images. The results of GeoPIV analysis and the ones obtained from Linear Potentiometers (LPs) were compared for the specimens.

5.7.3 Experimental Test Performed on Fresh Cementitious Composite

5.7.3.1 Flow Test

According to ASTM C1856/C1856M, Fabricating and Testing Specimens of Ultra-High-Performance Concrete, to test the flowability of the fresh concrete, the flow table shown in Figure 5.5 was used, which meets the requirements of the ASTM C230/C230M. The mold was filled in a single layer. Then it was lifted and let the fresh concrete was let to spread laterally on the table for 2 minutes. The diameter of concrete was measured along the line of the maximum and minimum diameter. The flow value would be the average diameter. The results are presented in Chapter 6.

5.7.4 Experimental Test Performed on Hardened Cementitious Composites

5.7.4.1 Compression Tests

5.7.4.1.1 Cube Specimens

Uniaxial compression tests were performed using small FRCC cubes with dimension of 50mm. The load was applied under force control at a constant rate of 0.259 MPa/s (Figure 5.6). Typically, the peak strength was attained in 10-15 minutes.

5.7.4.1.2 Prismatic Specimens

Additional compression tests were carried out on small prisms with an aspect ratio of two, with dimension of $50 \times 50 \times 100$ mm. Tests were performed under displacement control using a rate of 0.005 mm/s in the 600KN MTS universal Testing Machine. Photographs were taken periodically in every 5 seconds and Digital Image Correlation (DIC) using GeoPIV-RG (2015) were used to analyse the results and measure vertical and lateral strain of specimens.

5.7.4.2 Flexural Tests

Four-point bending beam tests were performed on unreinforced SHFRCC prisms. The advantage of four-point bending test is that there is a constant moment region (pure flexure with no simultaneous shear) in the center of the span and therefore the state of stresses in the middle region can be analysed easily. Prisms with sizes of 500×75×75mm and 280×75×75mm were tested to evaluate the behaviour of concrete under flexure/shear. For longer prisms, the distance between the intermediate load points (shown as “e” in Figure 5.10) was 100mm and for shorter prisms it was 75mm. Shear span ratios were a/h = 2 or 1 for the two prism lengths respectively, whereas prisms extended (shown as “f” in Figure 5.10) by 50 and 28.5mm respectively beyond the supports. The intention of testing two different aspect ratios was so as to establish whether the tensile strength was affected by this parameter as was seen in previous relevant research (Georgiou 2017). Tests were performed under displacement control with a test rate of 0.005 mm/s. Mid-span vertical deflection was measured using a Linear Potentiometer (LP) with a stroke of 50mm mounted in the midspan and at the mid-height

of the prism. A camera system was also placed taking pictures every 5 seconds to correlate the pictures with the results of the LP. The jig and the frame to hold the Linear Potentiometer in the mid span of the prisms are shown in Figure 5.11.

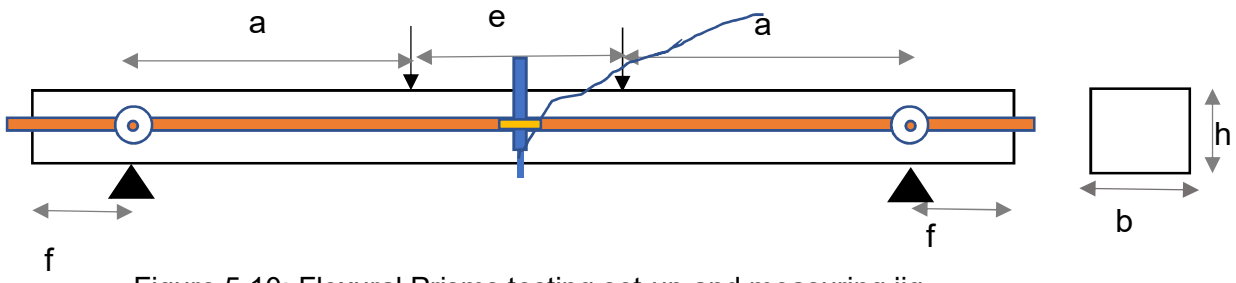

Figure 5.10: Flexural Prisms testing set-up and measuring jig

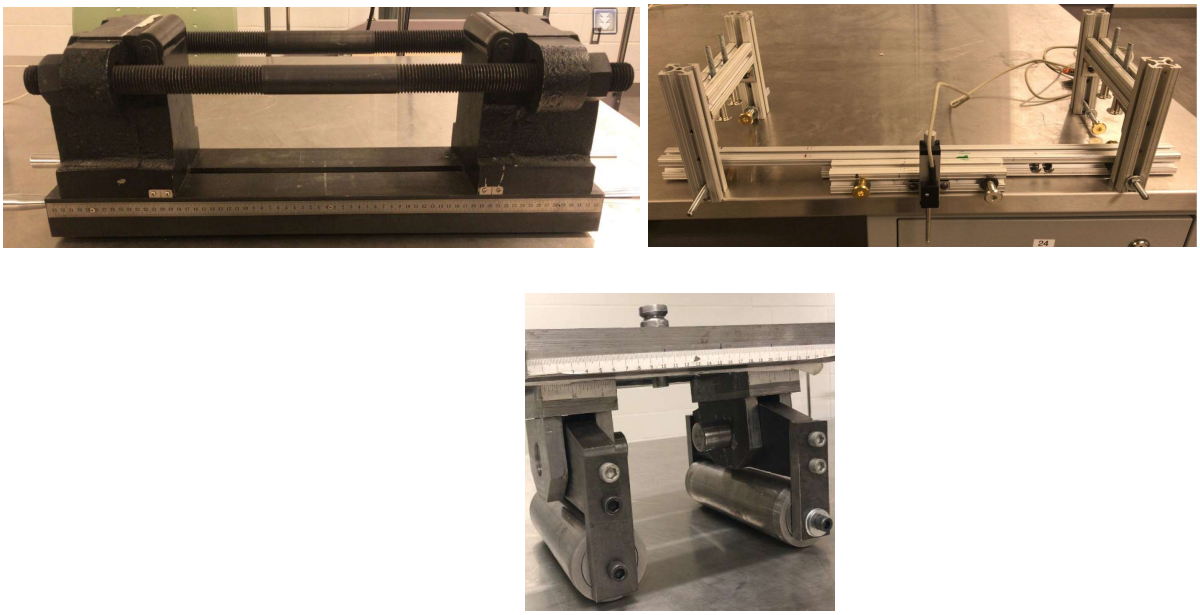

Figure 5.11: The jig and LP frame for flexural tests

5.7.4.3 Shear Push-off Tests

As was discussed in Section 2.4, a direct shear test may be conducted using a push-off test setup. This test reproduces the basic transfer mechanics of pure shear with combined normal stress, without the simultaneous action of flexure as would occur in beams which are more suitable to study the behaviour of concrete under flexure-shear. The exact

dimension of the selected four different types of the push-off specimens are given in Figure 5.12. Half-scale pure shear and compression shear specimens (similar to the ones shown in the Figure 5.12 but at 1:2 scale) were also considered.

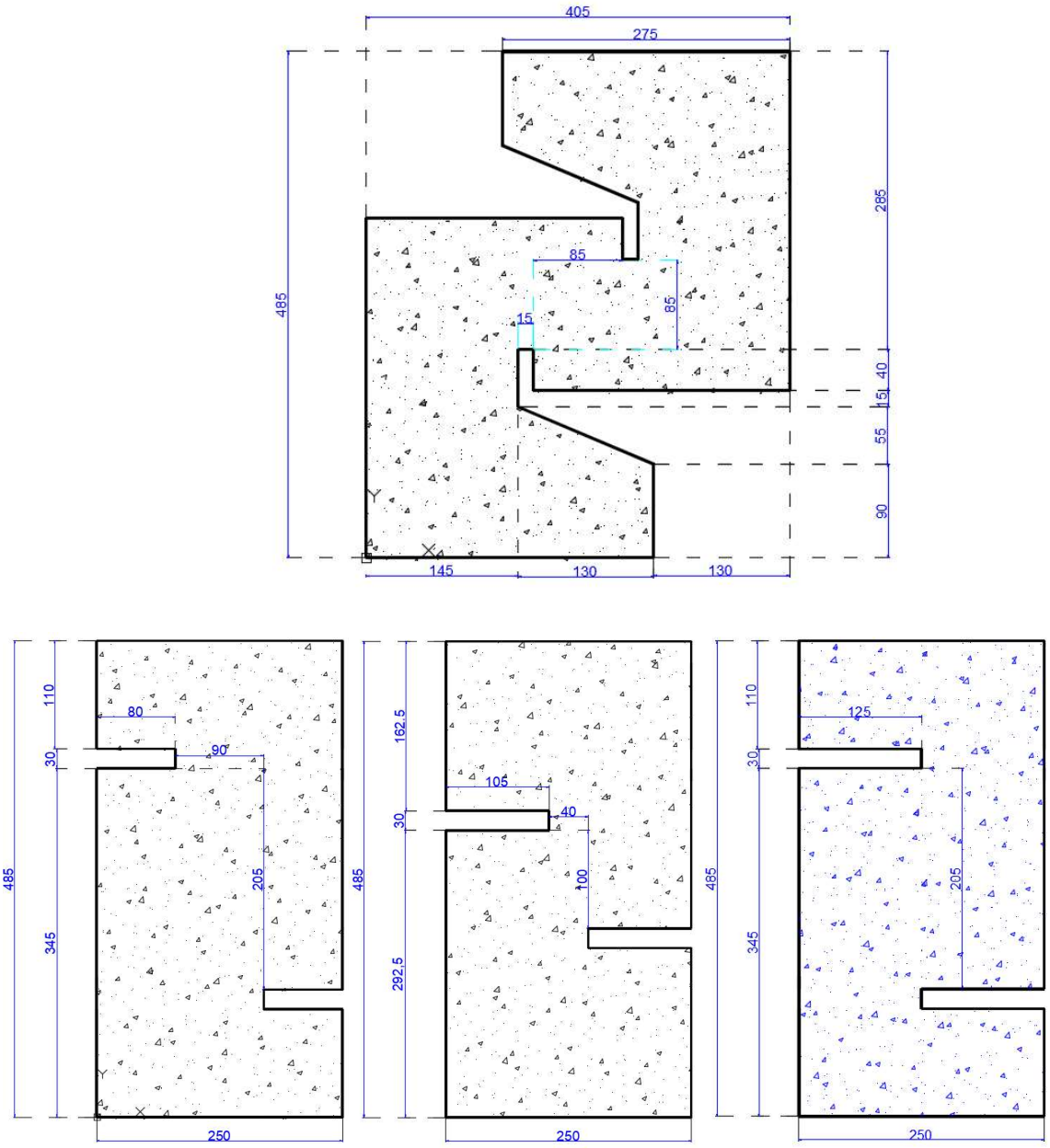

Figure 5.12: Push-off specimens and dimensions (the thickness of all specimens are 100mm)

Specimen geometries were chosen so as to yield specific combinations of shear and normal stress at the plane of failure so as to support derivations of the Mohr-Coulomb

failure envelope of the Strain Hardening Fiber Reinforced Cementitious Composite (SHFRCC) and thereby calculate the maximum shear strength of the material, a topic that will be discussed in more detail in the following section.

5.7.4.3.1 Mohr-Coulomb Failure Envelope

An infinite number of normal and tangential (shear) stress combinations acting on a plane of failure of concrete can lead the material to failure (Figure 5.13). Rather than conducting a very large number of tests, the Mohr-Coulomb criterion is actually a mathematical relationship between σ_n and τ, that describes the experimental trends and approximates the values of all possible combinations. Figure 5.13 depicts an element at failure with the principal stresses (σ_{1f}, σ_{3f}) that caused failure and the resulting normal (σ_{ff}) and shear stresses (τ_{ff}) on the failure plane.

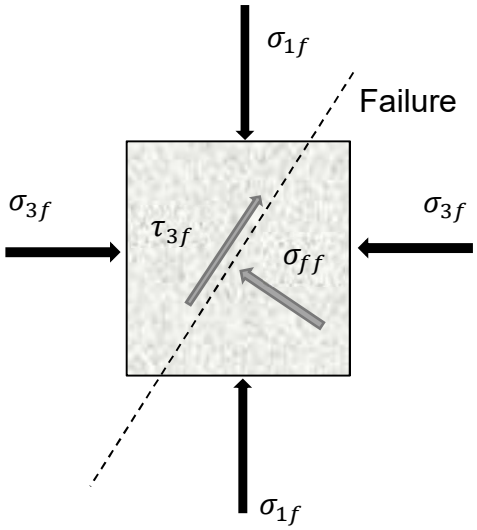

Figure 5.13: An element at failure with principal stresses

Clearly, if we know the principal stresses, we can draw the Mohr circles and having at least two Mohr circles we can draw the Mohr-Coulomb failure envelope which is the closest line tangent to circles (Figure 5.14). The Mohr-Coulomb failure envelope is defined with a linear function:

$$\tau_f = c + \sigma_f tan\phi \quad (5.1)$$

Where τ_f is maximum shear stress the concrete can attain just before failure, under normal stress of σ_f with a failure plane inclination of $tan\phi$.

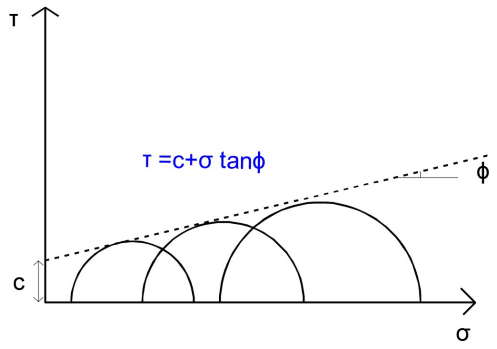

Figure 5.14: Mohr-Coulomb envelope

Here, in this part of the experimental program, it was decided to cast six different pairs of push-off specimens:

- Pure shear (PS)
- Compression shear type 1 (CS)
- Compression shear type 2 (CS')
- Tension shear (TS)
- Half-scale pure shear (SPS) (the 1:2 scale refers to the previous set listed above which in the context of this discussion are the 1:1 scale specimens)
- Half-scale compression shear (SCS)

Figure 5.15 shows the principal stresses of the shear plane under study. To get different points along the Mohr-Coulomb failure envelope and be able to estimate the maximum shear stress that concrete will carry, at least three different types of push-off specimens are needed. The intent of the 1:2 scale specimens was to collect data so as to assess the possible size effect in SHFRCC. The design of push-off specimens to meet the objective of the experimental study, as well as, the specimen preparation (including FRP wrapping and Finite Element Modelling) and the test procedure are discussed in detail.

5.7.4.4.2 Design of Specimens

To confirm the existence of a uniform shear stress distribution in the failure plane of the tension shear specimen, the specimen forms illustrated in Figure 5.12 underwent several cycles of refinement assisted by Finite Element Modeling (FEM). To this end, 3D Analysis was performed using SAP2000, CSI (2017). Solid elements were used to resemble the concrete meshes. Figure 5.16 depicts the procedure for the Tension- Shear specimen. The global coordinate system is as demonstrated in Figure 5.16; the local coordinate axes of each solid element are denoted 1, 2, 3 and are identical to global X, Y, Z, respectively. Regarding the applied restraints on nodes, out of plane displacement (D2) and out of plane moment (M1) is restricted for all nodes of the middle plane (Y=0) and for none of the nodes in the 3D model torsion is allowed (M3=0).

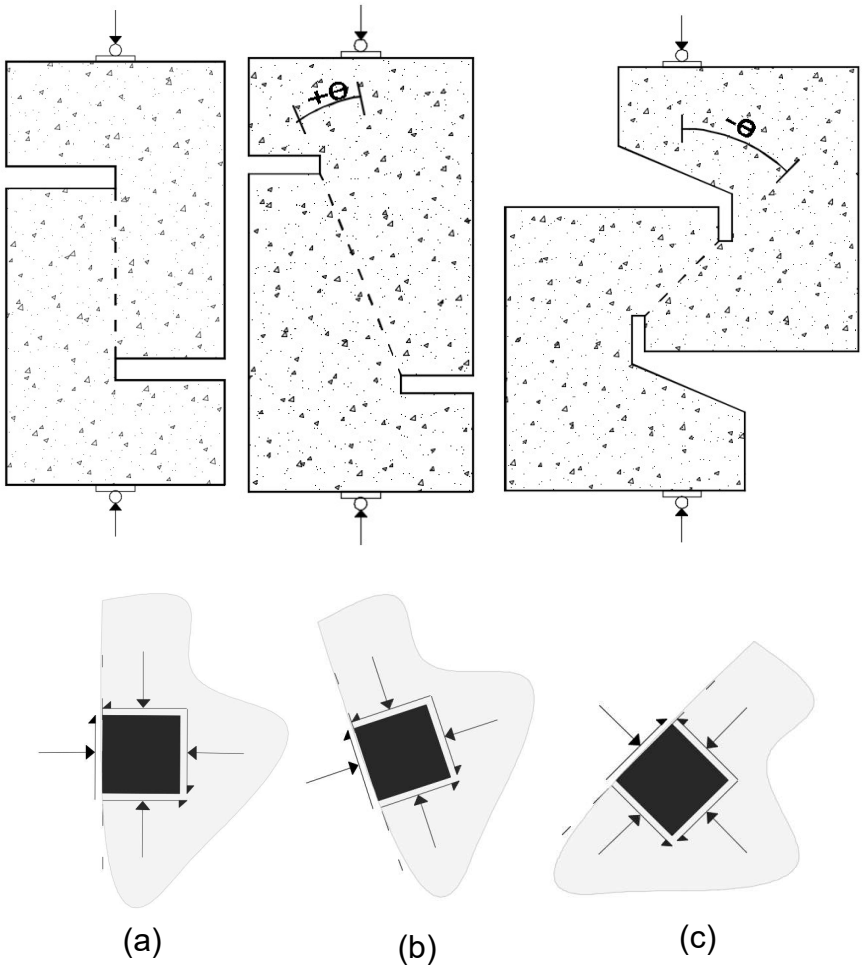

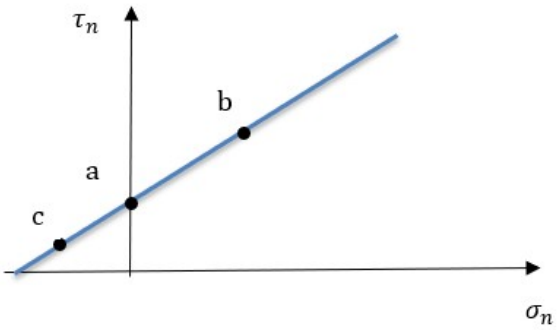

(d)

Figure 5.15: Principal stresses along the shear plane of the push-off specimens (a) pure shear, (b) compression shear and (c) tension shear. (d): corresponding Mohr-Coulomb envelope.

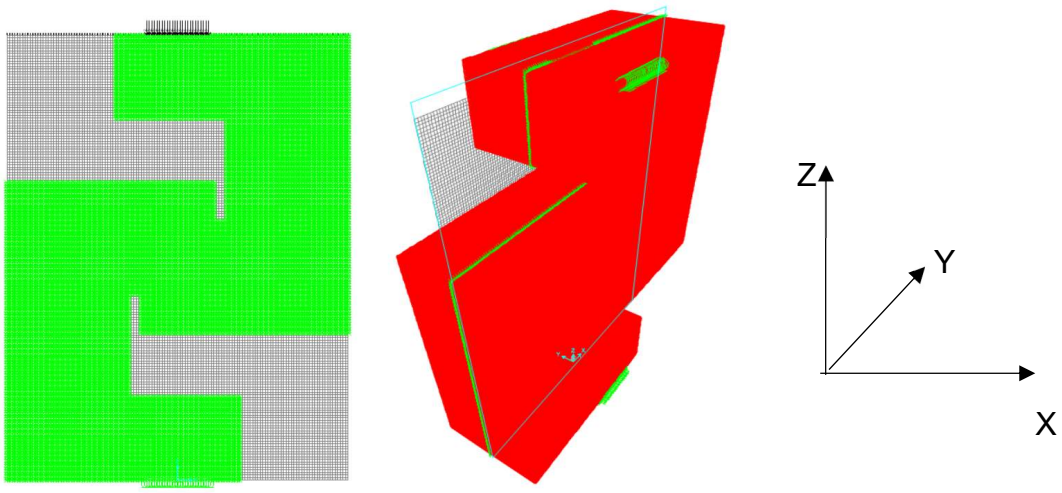

Figure 5.16: Finite Element Modeling of tensile shear push-off specimen in SAP2000

Analysis has been done under displacement control condition (unit displacement has been applied on top of the specimen). Figure 5.18 demonstrates the stress distributions along the critical section in tensile shear push-off specimen. S11 is the direct stress (in the context of this investigation stress is defined as force per unit area) acting on the positive (or negative) 1-face (i.e. on the face whose normal unit vector is along axis 1) and oriented in the 1-axis direction. Similarly, S22 is the direct stress acting on the positive

(or negative) 2-face in the 2-axis direction. S13 is the shearing stress acting on the positive (or negative) 1-face in the 3-axis direction (Figure 5.17). As can be seen in Figure 5.18, neglecting the effect of stress concentration near edges, an approximately uniform shear stress field is observed in the critical cross section which, in this type of specimen, is defined by the ends of the notches (S13).

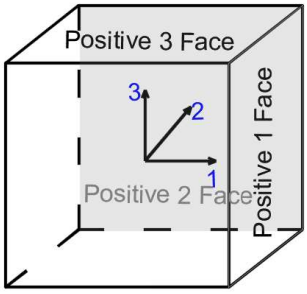

Figure 5.17: An internal solid element and the local coordinate axes

S11 S22

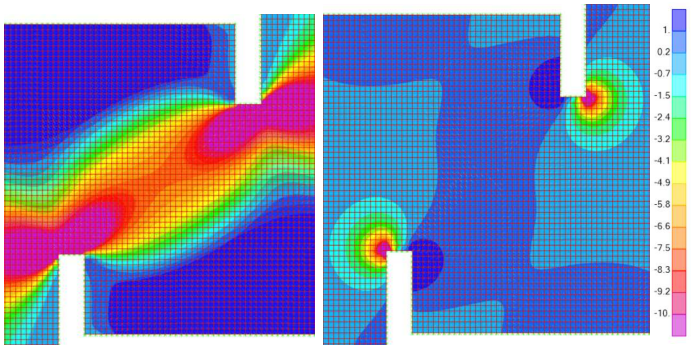

S33 S13

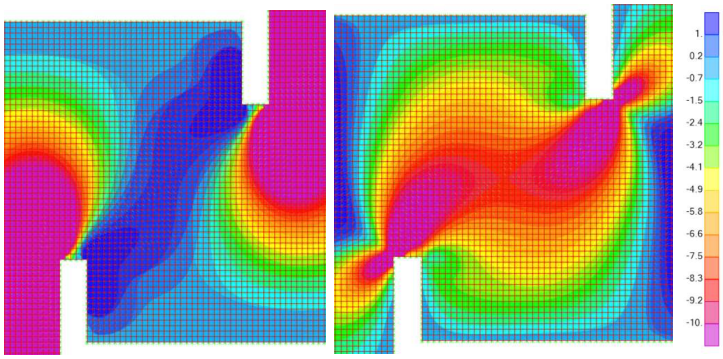

Figure 5.18: Stress distributions along the critical section in tensile shear push-off specimen

5.7.4.3.2 Specimen Preparation

A total of 12 push-off specimens were cast using four mixes (due to the limitation of volume and shear capacity of the concrete mixer) which was performed using the same mix in two days. The following steps were taken to prepare and test specimens:

a: Wooden molds were built from plywood in the required sizes and were oiled repeatedly several days in advance before casting.

b: Notches were cut from firm foams and were placed in the molds and glued firmly in order to avoid any movement during casting.

c: Specimens were cast without using any vibrator since the developed concrete was self-compacting.

d: The top of specimens was covered with plastic sheets. Specimens were left in molds for two days.

e: Specimens were demolded after 48hours and placed in water.

f: Specimens were taken off the water few weeks before the tests and they were reinforced using Carbon Fiber Reinforced Polymer (CFRP) in the regions where tension was identified from the Finite Element analysis results, outside the anticipated failure plane defined by notches (Figure (5.19)). Objective was to arrest catastrophic tension crack propagation prior to development of failure in the study region. The procedure is explained in detail in the following sections.

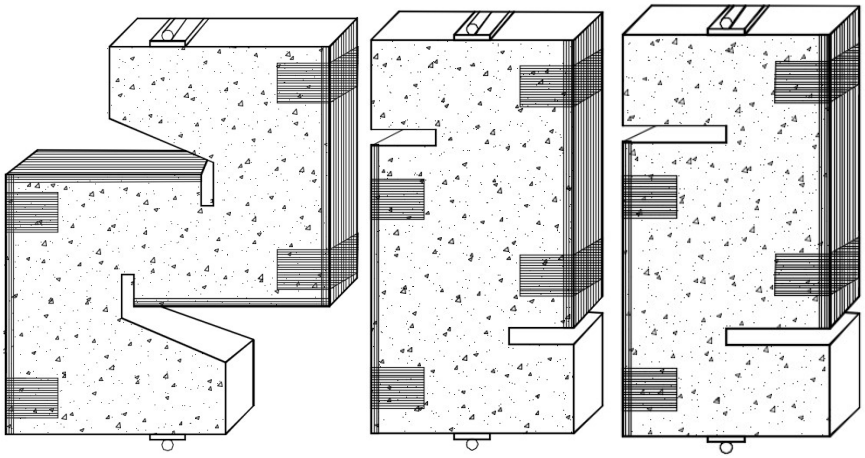

Figure 5.19: Direction of FRP wrapping of push-off specimens

g: In order to have flat and parallel loading surfaces, gypsum cement and fine sand was used to make flat capping for all specimens.

h: Linear Potentiometers (LPs) with a stroke of 50mm were installed to record the vertical and lateral displacement of the shear plane (Figure 5.20). Instrumentation mounting locations were marked off on the specimens using a ruler and square and a bow compass in the center of the back face of specimen, with a gauge length of $130\ mm$ and $180\ mm$ for horizontal and diagonal LPs for the 1:1 size specimens, respectively, and $80mm$ gauze length for the 1:2 specimens.

i: Splatter painting was used to paint the front side of specimens with white and black color speckles (to have 1-5-pixel size dots) and a camera system was placed taking pictures every 5 seconds to correlate the pictures with the results of the LPs using the DIC software, GeoPIV-RG (2015).

f: Specimens were tested under displacement control with a rate of 0.005 mm/s at the age of more than 100 days to study the long term mechanical properties of the composites.

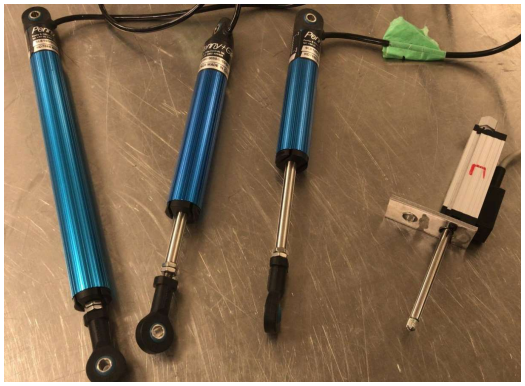

Figure 5.20: Two different Linear Potentiometers were used to record the vertical and horizontal displacements

5.7.4.3.3 Reinforcing with FRP

No internal steel reinforcement was used in the push-off specimens. However, in order to avoid the failure of specimens in any cross section other that the desired plane that is defined by the notches, specimens were wrapped with Carbon FRPs as depicted in

Figure 5.21 (SikaWrap Hex-230 C). The properties of the FRP sheets are presented in Table 5.2. They have been provided by Sika company in a 610 mm width roll. FRP sheets were cut in required sizes with an 20-30 mm extra length in each side to provide required anchorage. Furthermore, FRPs were anchored in both sides using strips of 50 mm thickness (Figure 5.21). A two-part epoxy-based laminating resin (Sikadur-330) was used to provide a strengthening composite system.

Figure 5.21: Push-off specimens wrapped with Carbon FRPs

5.7.4.3.4 Test Procedure

The specimens were loaded using the 600KN MTS Universal Testing Machine at York University. Linear Potentiometers (LPs) with a stroke of 50mm were attached to mounts and set to a small pre-tensioning displacement and then were set to zero in the Catman Data Acquisition software. A camera system was also placed taking pictures in every 5 seconds to correlate the pictures with the results of the LP using Digital Image Correlation System (DIC). Tests were performed under displacement control with rate of 0.005 mm/s. All specimens maintained their integrity and no collapse or deterioration of form was observed even after loss of strength. At a residual load of around 20% of maximum, the LPs were removed, and the displacement rate was increased to up to 0.05 mm/s to split the specimens into two pieces.

With the fibers with dtex 100, the anticipated number of fibers crossing per unit area of a cross section of the material is estimated from the following expression (Naaman 1972):

$$N_f = {4\alpha\rho_f}\Big/{(\pi {d_f}^2)} \quad (5.2)$$

α fiber orientating factor taken as 0.5

ρ_f volumetric ratio of fiber (here 2% for all mixes)

d_f fiber diameter (here $100\ dtex \approx 0.108\ mm$)

From the equation, for this study, the estimated number of fibers crossing a plane are, $N_f = 100$ per cm^2. According to Archontas and Pantazopoulou (2012), a factor to account for the angle of inclination of fibers crossing the cracks should be also considered ($\lambda_{eff} = 0.5$). Therefore, $N_f^{eff} = 50$ per cm^2.

This result is very close to the results obtained from counting the number of fibers from the failed specimens cross section (the pictures are given in Appendix B), which are approximately 30 fibers per cm^2. This information is critical to establish the tensile strength of the material after cracking and to correlate with the principal tensile stresses obtained from the tests.

5.7.4.4 Beam Tests

Two full-scale SHFRCC reinforced beams with dimensions of 915×150×150 mm were cast from Mix 3 (M3). Specimens were wrapped in wet burlap and covered with plastic sheets for 170 days and then were tested at age of 185 days due to limitted availability of laboratory equipment.

5.7.4.4.1 Design of Specimens

Beams were tested as shown in Figure 5.22. The intention was to avoid flexural failure and to force web shear failure in the beams so as to assess the shear strength of the SHFRCC. Therefore, three 15M steel bars were used to create a large shear force demand over a shear span of 1.87 of the effective beam depth d (d = 112 mm) with a 30 mm and 20mm vertical and horizontal cover, respectively. The estimated flexural shear strength ($M_n = A_s f_y (d - \frac{1}{2}(\frac{A_s f_y}{0.85\ f_c' b})$) and flexural shear demand ($V = {M_n}\Big/{a}$) to develop

yielding at midspan were 23.2 KN.m and 110.5 KN. To test the hypothesis of the models of Chapter 4, that shear failure is a manifestation of bond failure when strain penetration is possible, in the case of SHFRCC, beams were tested as such to have different anchorage length (9.5 D_b and 4.8 D_b) beyond the support points, while the shear span is constant.

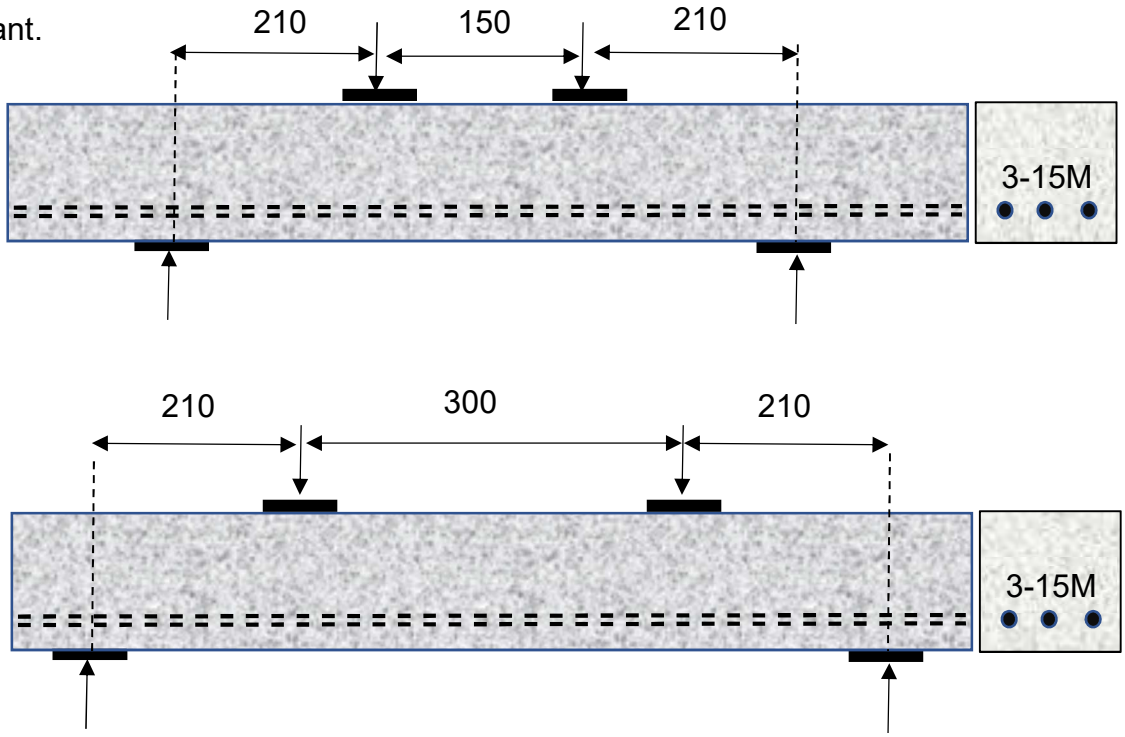

Figure 5.22: Test set-up of full-scale SHFRCC beams

5.7.4.4.2 Test Instrumentation

The mid-deflection of the beams was measured using a Linear Potentiometer (LP) with a stroke of 50mm and the data was collected using a Data Acquisition (DAQ) system. The resulting load-displacement curve for each beam is presented in Chapter 6.

5.7.4.4.3 Test Procedure

The specimens were loaded in the aforementioned 600KN MTS Universal Testing Frame at York University. A jig for measuring deflections of the midpoint of the beam was installed on the specimen (Figure 5.23). An LP with a stroke of 50 mm was placed in the middle of the beam. Tests were performed in a displacement control system with a rate of 0.005 mm/s. Photographs were also taken from the shear span of the beams in every 5 seconds for DIC analysis.

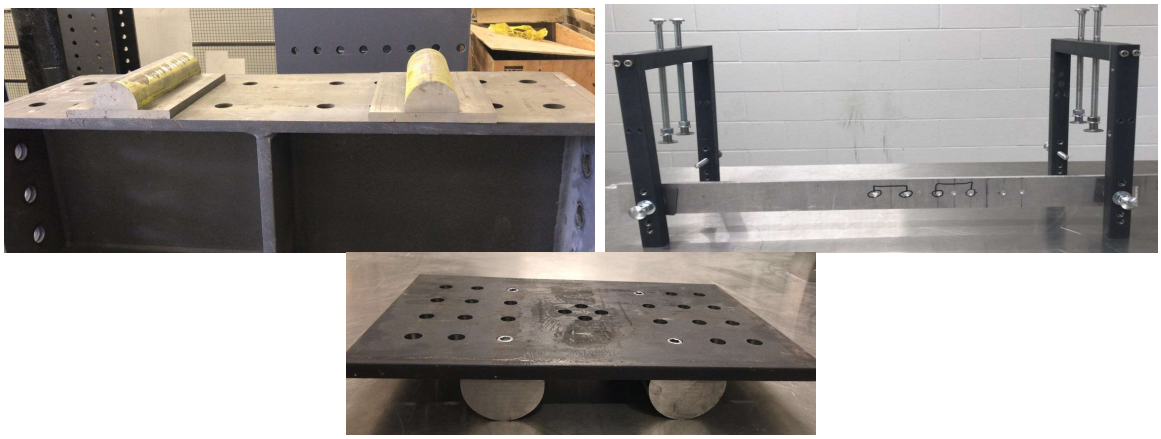

Figure 5.23: The jig and frame for flexural full-scale beam tests

CHAPTER 6: EXPERIMENTAL RESULTS

6.1 Introduction

Test results for both preliminary and main phases of the experimental program are presented in this Chapter. Results of compression tests on cylinders and cubes, and flexural (three-point and four-point bending) tests on small unreinforced prisms tested in the preliminary stage, are summarized in a tabulated format following with a representative set of pictures of the failure state of specimens while a more complete set of plots and pictures is presented in Appendix B. Results of tests conducted for the main phase of the experimental program are also presented in detail. Stress-strain plots of unreinforced prisms, push-off specimens, and full-scale beams obtained from both Linear Potentiometers (LPs) and Digital Image Correlation (DIC) followed by a calculation procedure to process and reduce the data are also included in this Chapter.

6.2 Preliminary Test Results

In this section, the compression strength of different mixes (f_c') and the maximum force undertaken in flexural tests (F_{max}) for representative specimens are presented in Table 6.1. The complete data are presented in Appendix B.

Figure 6.1 shows representative photographs of the cylinders, cubes and prisms at failure for different mixes. A whole set of pictures can be found in Appendix B. As can be seen from Figure 6.1, because of the confining effect of the fibers, no evidence of spalling or deterioration of the compression specimens is visible, and cracks are mostly parallel to the loading direction. For cubes, some inclined cracks near the edges exist which can be due to the small friction between loading plates and top and bottom of the specimens and the small aspect ratio of the specimens.

In the case of flexural specimens, the effect of fibers was evident in all specimens and no collapse or deterioration occurred. In the case of all mixes - except the one with coated fibers or mixes with the finest sand size (Bell & McKenzie #530 and #730) - fibers ruptured and a single localized crack was observed. For those mixes that showed a different response, multiple cracking with a fine crack width was observed for a prolonged range

of nonlinear, hardening response. Near failure (past the peak), one of the cracks localized and fibers were pulled out or some ruptured in the localized crack. Since coating is a time-consuming procedure and there is a risk of entraining two much air into the mix, it was decided to choose the B39 mix (uncoated fiber and Bell & McKenzie #730 sand) for large scale casting of the main phase of the experiment. The load- actuator displacement curves of all specimens are presented in Appendix B.

Table 6.1: Age of specimens and results of compression and flexural tests

Mix ID	Age (days)	f'_c (MPa)	F_{max} (KN)
B27	35 37	72.61	 6.45
B29	28		5.96
B32	28	70.68	6.42
B33	- 28	-	 6.98
B34	28	66.5	6.96
B35	28	65.31	3.87
B36	28	40	3.76
B37	28	56.46	5.99
B38	28	58.24	6.65
B39	28	70.95	5.63

B1 B2 B3 B6

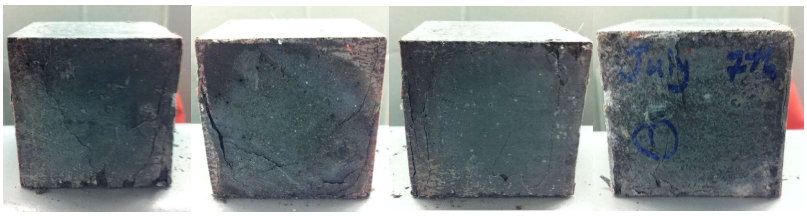

B17

B16

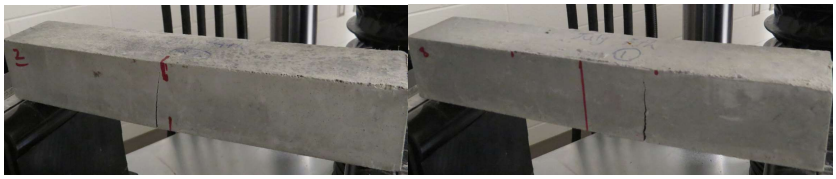

B16 B17

B38 B39

Figure 6.1: Representative cylinder and cube compression specimens and prisms flexural specimens

6.3 Main Phase Test Results

In this section, the workability data from the flow tests, compression test results, four-point bending test results on long (75 × 75 × 500 mm) and short (75 × 75 × 280 mm) prisms, shear push-off specimens test results, and four-point bending test results on full-scale beams (915 × 150 × 150 mm) are detailed. The specimens were tested at various ages (58 - 148 days) based on availability of laboratory machinery and equipment and preparation lead time.

6.3.1 Flowability Tests

As previously mentioned, a flow table was used to make sure the concrete was adequately self-consolidating without being excessively fluid which could lead to fiber floating and sand segregation. The first two mixes were the most flowable and they spread all around the table. For the three last mixes, 2 minutes after the mold was lifted the spread diameter was measured (the first value listed in the Table 6.2), and then the table was tamped 20 times and the second value was measured.

Table 6.2: Workability data for main batches

Mix	**Flow Value (mm)**
M1	254
M2	254
M3	125-190
M4	180-210
M5	210-240

6.3.2 Compression Tests

As explained in Chapter 3, cubes (50 × 50 × 50 mm) and prisms (100 × 50 × 50 mm) were tested under compression to estimate the compressive strength of the different mixes by dividing the maximum carried load over the cross-section area ($\sigma = {}^{F}/_{A}$). The results are presented in Table 6.3. While cubes were tested under load control system at a rate of 0.259 MPa/s, prisms were tested under displacement control at a rate of 0.005 mm/s. The failure crack compression prisms can be seen in Figure 6.2. Digital Image Correlation (DIC) system was used to get the load-displacement response of specimens as given in Figure 6.3.

Table 6.3: Test Results of specimens under compression

Mix	Type	Age (Days)	$f'_c\ (MPa)$
M1	Cube	148	81.82
M2	Cube	93	77.57
M3	Cube	185	73.79
M4	Cube	145	78.15
M5	Cube	145	76.97
M1	Prism	149	56.88
M2	Prism	149	55.04
M4	Prism	146	57
M5	Prism	146	65.44

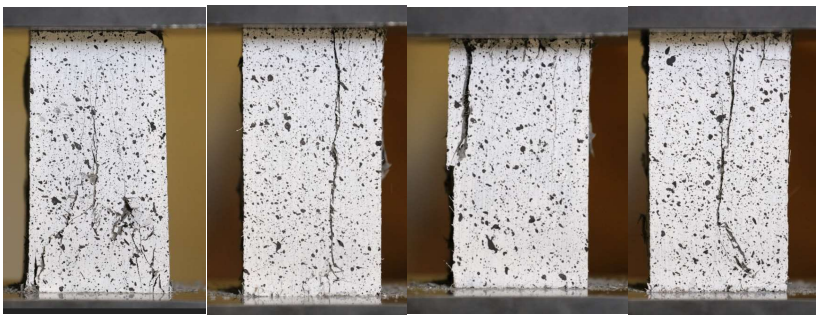

Figure 6.2: Prims tested under compression (From left M1-M2-M4-M5)

6.3.2.1 Digital Image Correlation (DIC) Analysis

The results of DIC analysis of all compression prisms are presented in Figure 6.3.

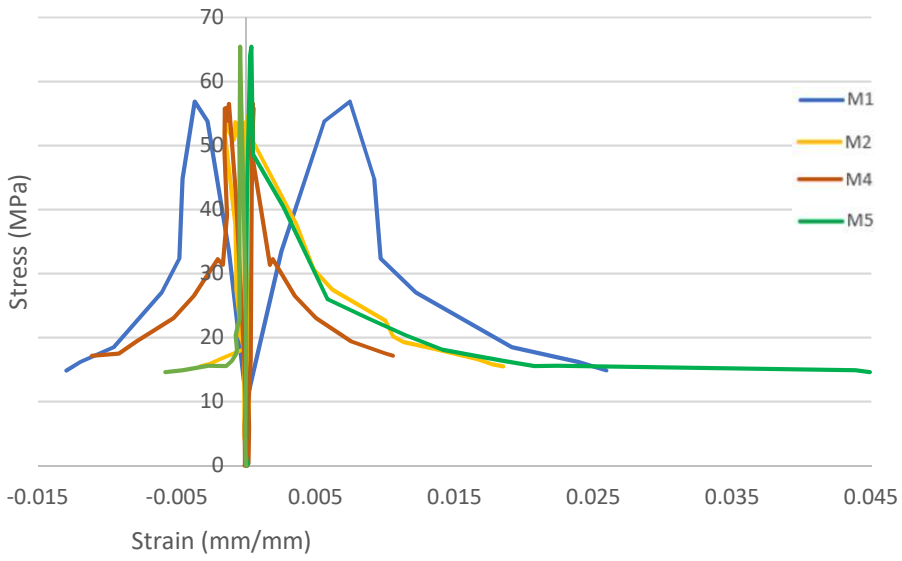

Figure 6.3: Load-displacement response of prisms under compression taken from DIC analysis

6.3.3 Flexural Tests

The failure crack of two representative flexural prisms can be seen in Figure 6.4. A full set of pictures can be found in Appendix B. The load-displacement curves of the long and short prisms tested to measure the tensile strength of the material through flexure are presented in Figure 6.5.

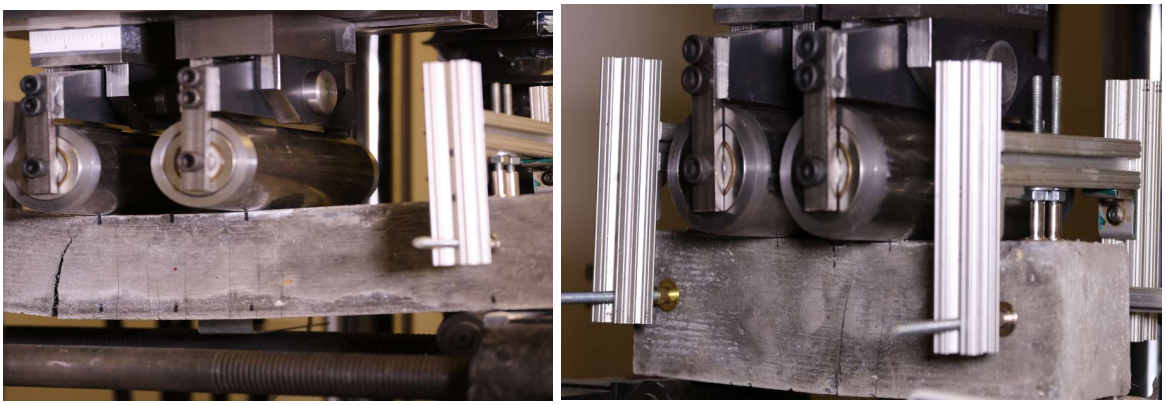

(a) (b)

Figure 6.4: Failure Cracks of (a) Long Flexural Prism specimen S4 (b) Short Flexural Prism specimen S2

6.3.3.1 Test Observation

A total of four long prisms were tested under four-point bending system. The first two specimens (S1 and S2) were cast from Mix 2 (M2) and were tested at 58 days whereas the last two specimens were cast from Mix 5 (M5) and were tested at 55 days. All prisms showed high ductility, multiple cracking and strain hardening behaviour. Load mid-span displacement curves are presented in Figure 6.5(a). The maximum load capacity of specimens for S1 to S4 were 9.88, 9.57, 8.57, 9.32 KN, respectively.

Two short prisms were also tested under four-point bending. They were cast from Mix 5 (M5) and were tested at 84 days. They also showed multiple cracking and strain hardening behaviour as depicted in the load mid-span displacement curves shown in Fig. 6.5(b). Peak loads attained for S1 and S2 were 21.86 and 19.88 KN, respectively.

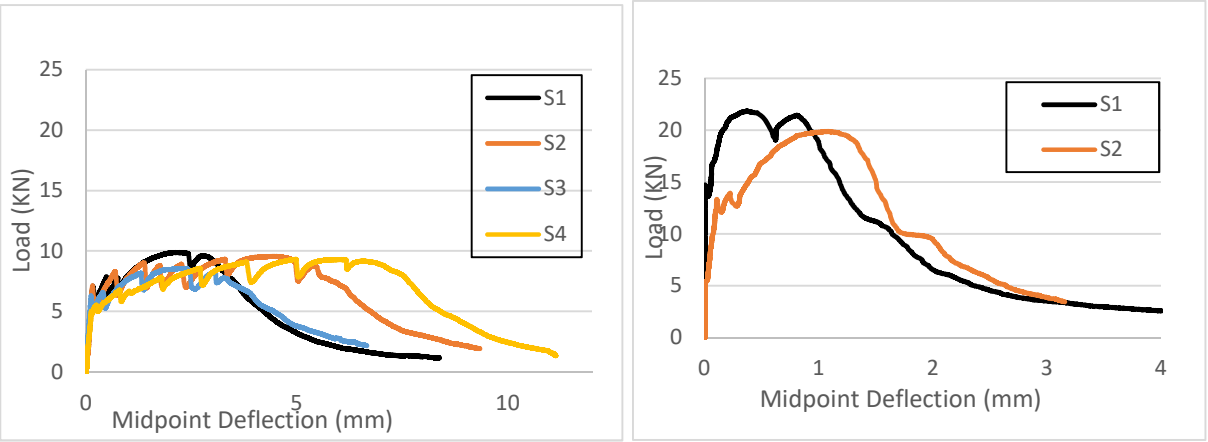

(a) (b)

Figure 6.5: Load- displacement of flexural prisms under four-point bending loading (a) Long Prisms and (b) Short Prisms

6.3.3.2 Digital Image Correlation (DIC) Analysis

Using DIC, the load-displacement curves were obtained as shown in Figure 6.6 and Figure 6.7. In the case of short prisms, there is a shift between results of DIC analysis and results of LPs. This is expected as the LP measures the displacement of the midpoint relative to the supports whereas DIC gives the absolute displacement of the speckles

from their original undeformed position. Yet, the difference is negligible for the long prisms, and within experimental error. For the shorter prisms the difference is significant in the initial ascending branch causing a constant shift of the curves from that point onwards.

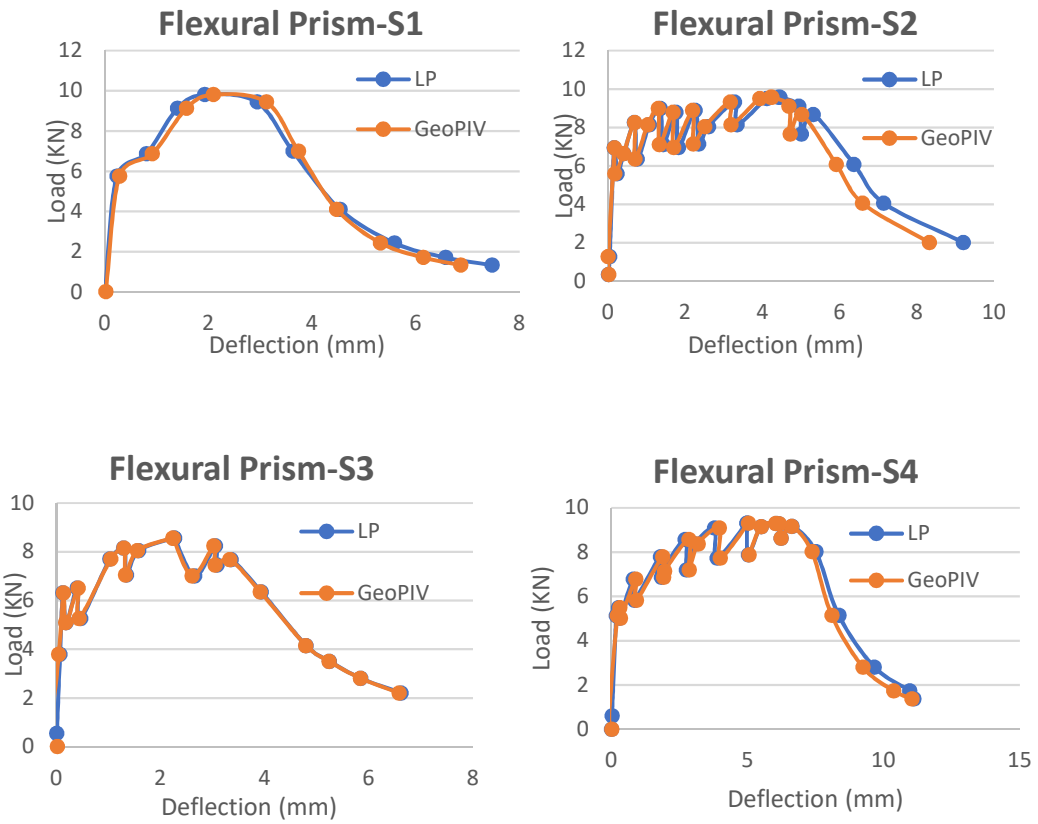

Figure 6.6: Load-displacement curves of long flexural prisms taken from LPs and DIC analysis

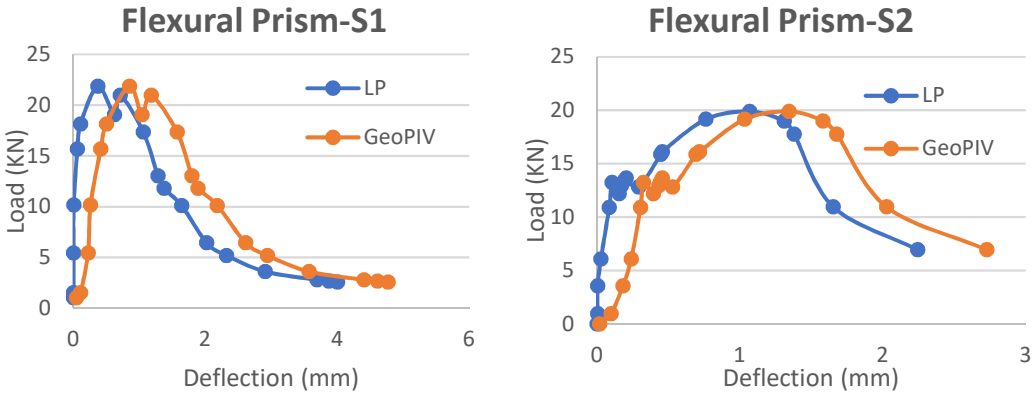

Figure 6.7: Load-displacement curves of short flexural prisms taken from LPs and DIC analysis

6.3.3.3 Data Analysis

Ultimate tensile strength of the PVA-SHFRCC ($f_{t,u}$) is calculated using the data obtained from DIC analysis of ***short*** prisms based on recommendation of ANNEX to section 8 of CSA S6 (CSA-S8 ANNEX 2017). $f_{t,u}$ is presented in Table 6.4.

Table 6.4: Calculation of elastic tensile strength and post-cracking behaviour of SHFRC by indirect tensile testing for fibers length $l_f \leq 20\ mm$ (CSA-S8 ANNEX 2017)

$\boldsymbol{E}$	$2{,}40\ h\ m$
$\boldsymbol{f_{crm}}$	$\frac{\sigma_1}{1.63}\left(\frac{\sigma_1}{\sigma_2}\right)^{0.19}$
$\boldsymbol{\varepsilon_{t,u}}$	$\frac{f_{crm}}{E}\left(7.65\frac{\delta_3}{\delta_1}-10.53\right);$ $\varepsilon_{t,el}={f_{crm}}/{E}$
$\boldsymbol{f_{t,u}}$	$\alpha^{-0.18}\left(2.46\frac{\sigma_3}{\sigma_1}-1.76\right)f_{crm}$ $\alpha={\varepsilon_{t,u}}/{\varepsilon_{t,el}}$
$\boldsymbol{\varepsilon_{t,0}}$	$\gamma^{-0.37}\alpha^{0.88}\left(3.00\frac{\delta_4^{\ *}}{\delta_3}-1.80\right)\frac{f_{crm}}{E}$ $\gamma={f_{t,u}}/{f_{crm}}$
$\boldsymbol{w_0}$	$\left(\varepsilon_{t,0}-\varepsilon_{t,u}+\frac{10f_{t,u}}{3E}\right)\frac{3h}{2}$

where,

m is the initial slope of the load-deflection curve

σ is the equivalent tensile stress calculated as follows: $\sigma=\frac{FL}{bh^2}$

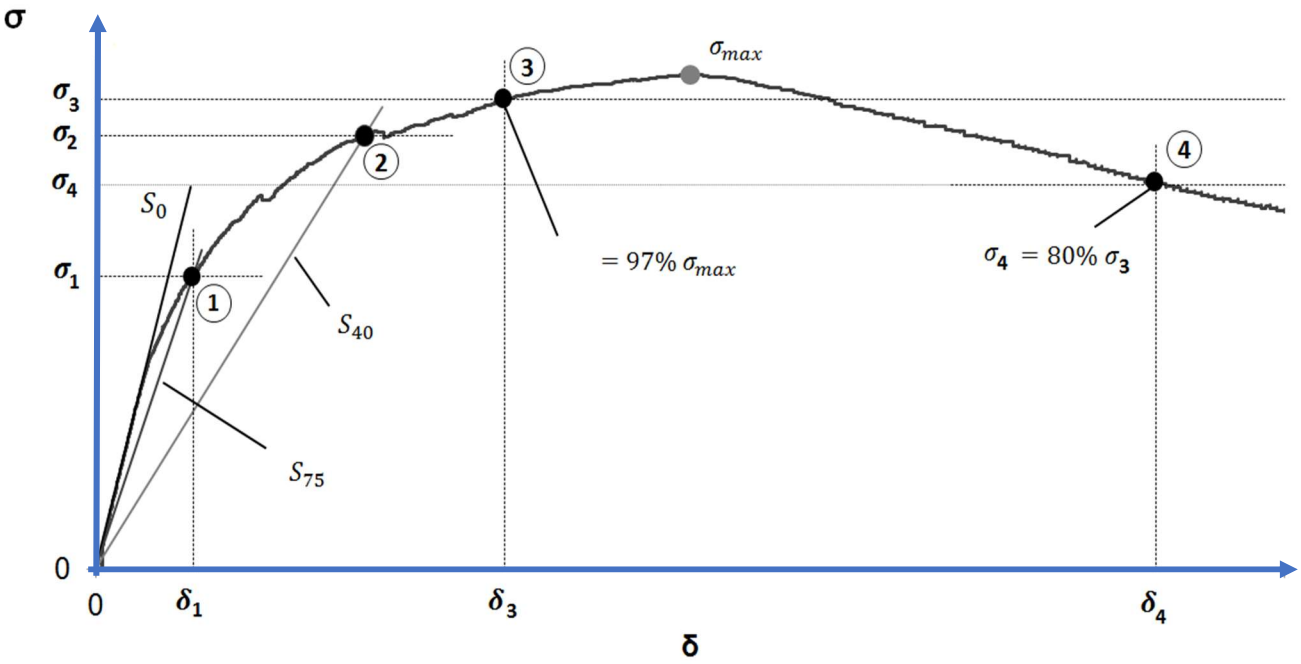

Figure 6.8: Typical four-point bending test results (CSA-S8 ANNEX 2017)

As may be seen in Figure 6.8, σ_i is the equivalent tensile stress defined at the intersection of a straight line from the origin with a slope corresponding to a fraction of i% of the initial slope and the load-deflection curve. For each prism, σ_i and corresponding δ_i is calculated (Figure 6.9). The results of ultimate tensile strength of specimens are as shown in Table 6.5.

Table 6.5: Calculated ultimate tensile strength of specimens

	$f_{t,u}\ (MPa)$	$\sigma_{max}\ (MPa)$
S1	6.54	11.66
S2	5.24	10.6
Average tensile strength	5.9	11.3

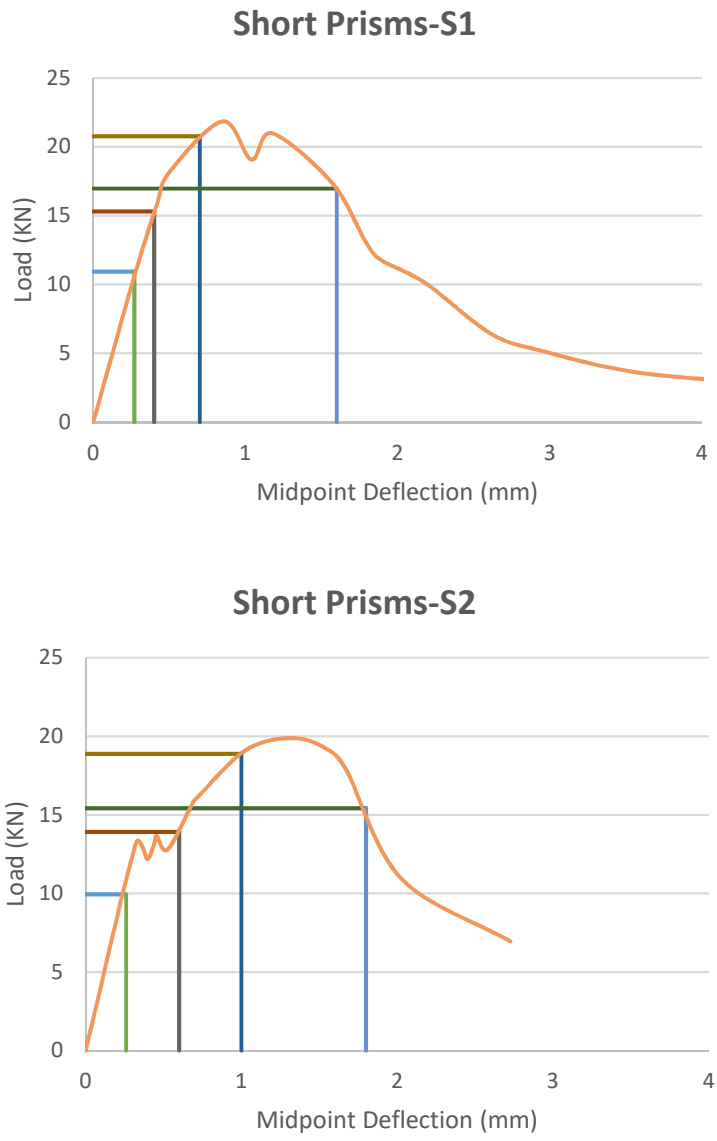

Figure 6.9: Calculation of ultimate tensile strength from the load-displacement curves of short prisms

To calculate the equivalent stresses before the peak, in Figure 6.9, 0.50%, 70%, and 95% of the peak load are selected. By comparing the maximum equivalent tensile strength ($\sigma_{max} = 11.3\ MPa$) and the ultimate tensile strength ($f_{t,u} = 5.9\ Mpa$) it is evident that since the formulas to get $f_{t,u}$ are calibrated based on steel fibers, this value is not reliable for PVA fibers.

6.3.4 Shear Push-off Tests

As explained in detail in Chapter 5, six pairs of push-off specimens (12 specimens in total) were cast as follows:

- Pure shear (PS), height = 480mm
- Compression shear type 1 (CS), height =480mm
- Compression shear type 2 (CS'), height =480 mm
- Tension shear (TS), height =480 mm
- Half-Scale Pure shear (SPS), height = 240mm
- Half-Scale Compression shear (SCS), height = 240mm

In each pair, the first specimen (S1) was cast from Mix 1 (M1) and the second specimen (S2) was cast from Mix 4 (M4) except for the tension specimens, S1 and S2, which they were cast from Mix 2 (M2) and Mix 5 (M5), respectively.

Horizontal and vertical displacements were calculated using combination of Linear Potentiometers and the DIC system. The exact locations of the selected points to extract displacements from the DIC software (GeoPIV-RG (2015)) are shown in Appendix B. Figure 6.10– 6.15 shows the load-displacement of all different types of specimens from the collected data from Linear Potentiometer (LP).

6.3.4.1 Test Observations

As was reported in Section 6.3.2 (compression tests) Mix 1 reached a higher compressive strength as compared to the other mixes. This increased strength led to stronger bond between fibers and cementitious material and most of fibers ruptured rather than showing pull out behaviour. This was evident by the less ductile behaviour observed in all specimens that were cast from Mix 1. Furthermore, as was reported in Section 6.3.1 (flowability tests), Mix 1 was the most flowable mix leading to smaller resistance to flow due to internal friction - therefore fibers tend to move upward being lighter than the cementitious fluid, and this reverse segregation was evident in the cross section of the corresponding failed specimens. There were more fibers on the front face (top face during casting) of specimens as compared to the back face (the face in contact with the mold).

It is noteworthy that because of use of a spherical seat as the bottom loading plate minor twisting was observed in some of the specimens therefore in the subsequent compression tests, a fixed steel plate was used to prevent this effect. In the following section the behaviour of each specimen will be discussed in detail:

- Pure Shear Specimens (PS)

For PS-S1, the maximum load attained was 135.4 KN with a horizontal displacement (δ) at the failure plane between notches of 0.1mm. A significant degradation in load-carrying capacity followed immediately after cracking in the shear plane. However, in case of PS-S2, multiple cracking was observed and after a strength loss from maximum load of 175.1 KN (at $\delta = 0.2mm$) to about 100 KN, which occurred gradually, no further strength reduction occurred as may be seen in Figure 6.10. An almost horizontal plateau in the load-displacement curve was seen at the end of the experiment for S2.

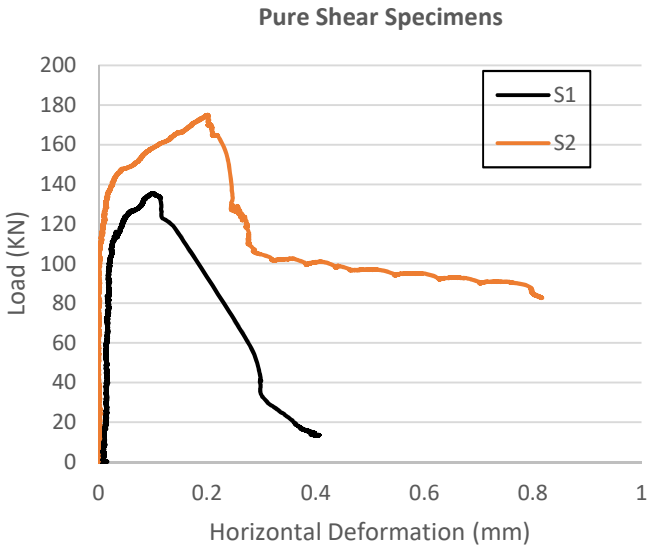

Figure 6.10: Load-displacement curves of pure shear push-off specimens

- Compression Shear Specimens (CS)

For the CS pair, the MTS machine was set to a maximum load of 400 KN while until 340.7 KN no crack was observed. Therefore, the test was stopped, and the specimen was unloaded, the MTS limit was changed, and the test was run for the second time. Although

the MTS was supposed to be set at maximum load of 600 KN, another unknown internal limitation inside the programming limited the loading protocol to be below 500 KN. CS-S1 reached the maximum of 484.7 KN (and $\delta = 0.23mm$) and 37 seconds later the load dropped quickly to 33 KN with a loud sound.

In case of CS-S2, since this specimen was built from mix 4, it was expected to exceed 500 KN and to show a more ductile behaviour. However, as explained before, there was an unknown limitation which caused the test to stop at 500 KN (and $\delta = 0.28mm$) and the system started to unload for 110.8 seconds (1.85 minutes) and reached 477.1 KN but then it was loaded again for 16.8 seconds to reach 500 KN; then there was again an unloading for 27.5 seconds and it reached 490.3 KN. Upon further loading the specimen failed with a loud sound.

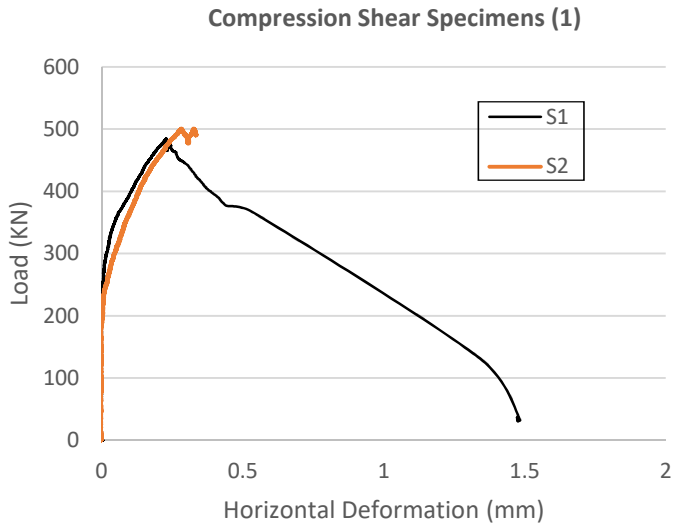

Figure 6.11: Load-displacement curves of compression shear (type 1) push-off specimens

- Compression Shear Specimens-Type2 (CS')

Specimen CS'-S1, reached a maximum of 415.4 KN (and $\delta = 0.36mm$) but the load dropped quickly with a loud sound. A stress concentration at the edge of the bottom loading plate to the inside edge of the bottom notch characterized the specimen failure.

Specimen CS'-S2 reached a maximum load of 551.85 KN (and $\delta = 0.25mm$) and very quickly after maximum it dropped and failed with a loud sound.

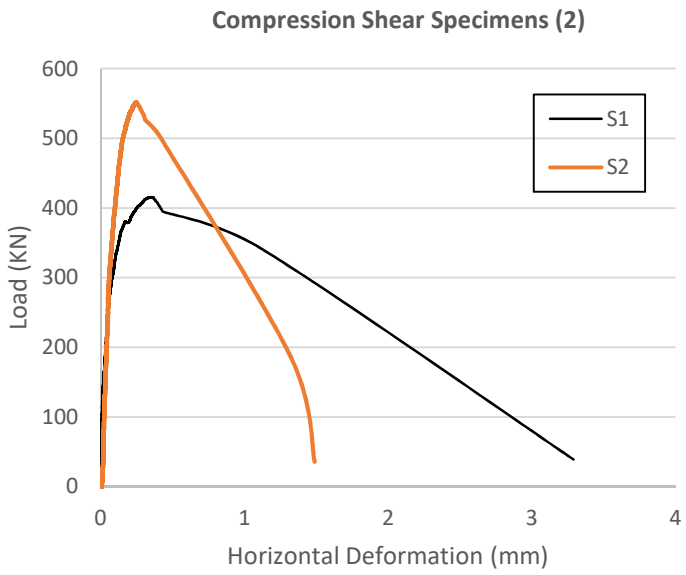

Figure 6.12: Load-displacement curves of compression shear (type 2) push-off specimens

- Tension Shear Specimens (TS)

In the case of tension shear specimens, spherical seats were used. TS-S1 reached the maximum of 31.54 KN (with $\delta = 0.84mm$) and showed very ductile behavior marked by multiple cracking. Fibers pulled out slowly as the main crack was widened and the load dropped gradually. For TS-S2, the maximum load attained was 22.34KN (with $\delta = 0.13mm$) and also demonstrated ductile behaviour. However, the crack in the front side of the specimen was started from the top part of the top notch but in the back side of the specimen, the crack was formed between two notches.

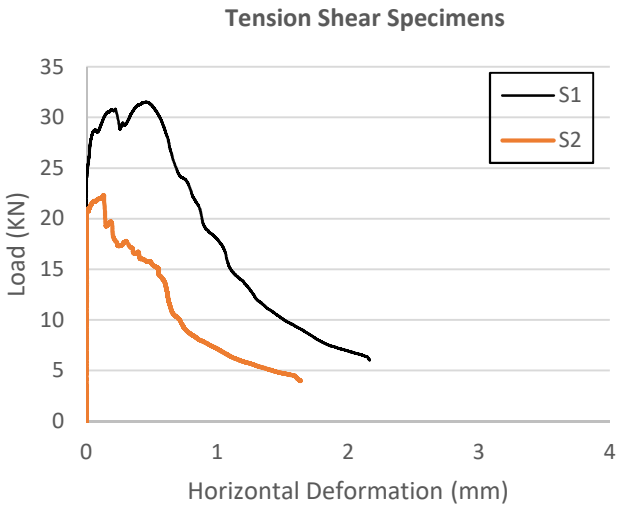

Figure 6.13: Load-displacement curves of tension shear push-off specimens

- Half-Scale Pure Shear Specimens (SPS)

Specimen SPS-S1, reached a maximum of 73.97 KN (and $\delta = 0.59mm$). Upon further loading under displacement control, the load dropped gradually to a 20% residual load and then the test was stopped. SPS-S2, however, failed spuriously in the upper horizontal branch by flexure. This specimen was casted from mix 4 and was expected to be stronger and more ductile. However, the flexural strength of the top part of specimen (above the notch) was not enough to hold that additional force demand at 75.85 kN (at $\delta = 0.27\ mm$) before any signs of shear failure settling in the plane defined by the two notches. Beyond that point the specimen split vertically above the notch, in the location of the center part of the specimen, with no further damage in the studied shear plane.

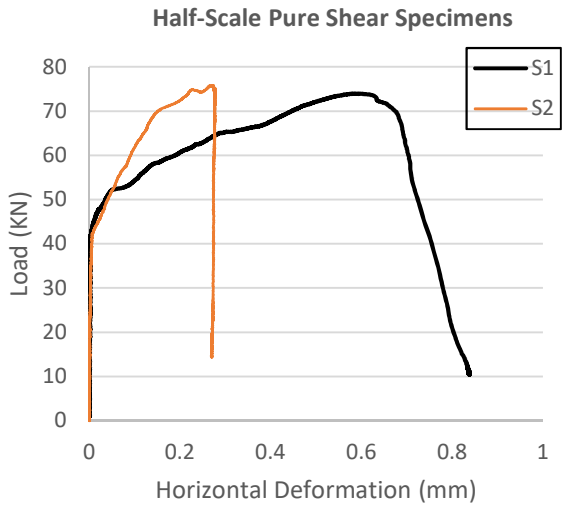

Figure 6.14: Load-displacement curves of half-scale pure shear push-off specimens

- Half-Scale Compression Shear Specimens (SCS)

SCS-S1 reached a maximum of 257.98 KN (and $\delta = 0.26mm$) and then quickly lost the load bearing capacity, failing with a loud sound. SCS-S2 reached a maximum load capacity of 281.23 KN (and $\delta = 0.17mm$). Upon further loading the load capacity dropped quickly, and the specimen reached a 30% residual load with a loud sound (but not as brittle as the S1).

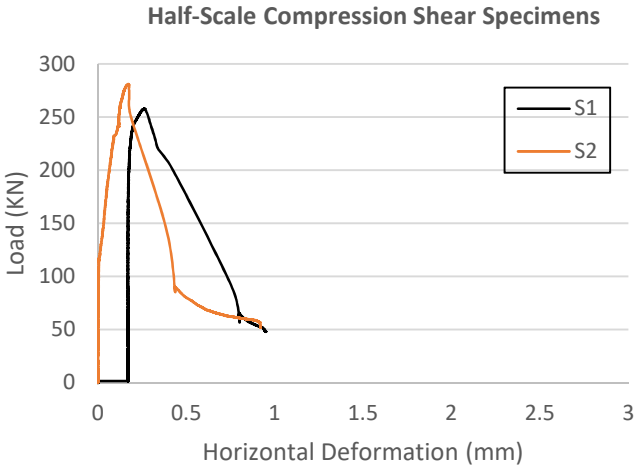

Figure 6.15: Load-displacement curves of half-scale compression shear push-off specimens

The failure cracks of push-off specimens casted from mix 1 are given together with the load-crack opening displacement in Figure 6.16. Specimens from Mix 2 are presented in Figure 6.17. Failure cracks of half scale specimens cast from Mix 1 and Mix 4 are presented in Figure 6.18 and Figure 6.19, respectively.

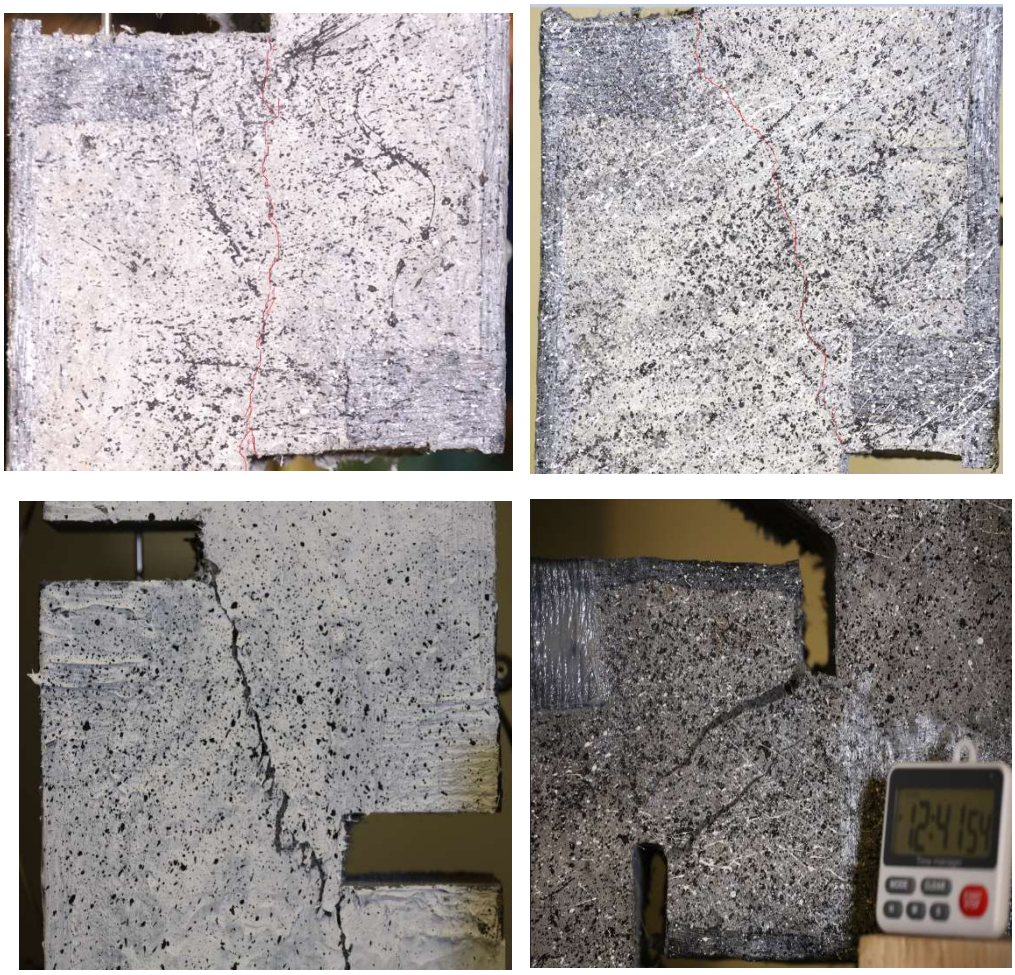

Figure 6.16: Push-off Specimens failure cracks (PS-S1; CS-S1; CS'-S1; TS-S1)

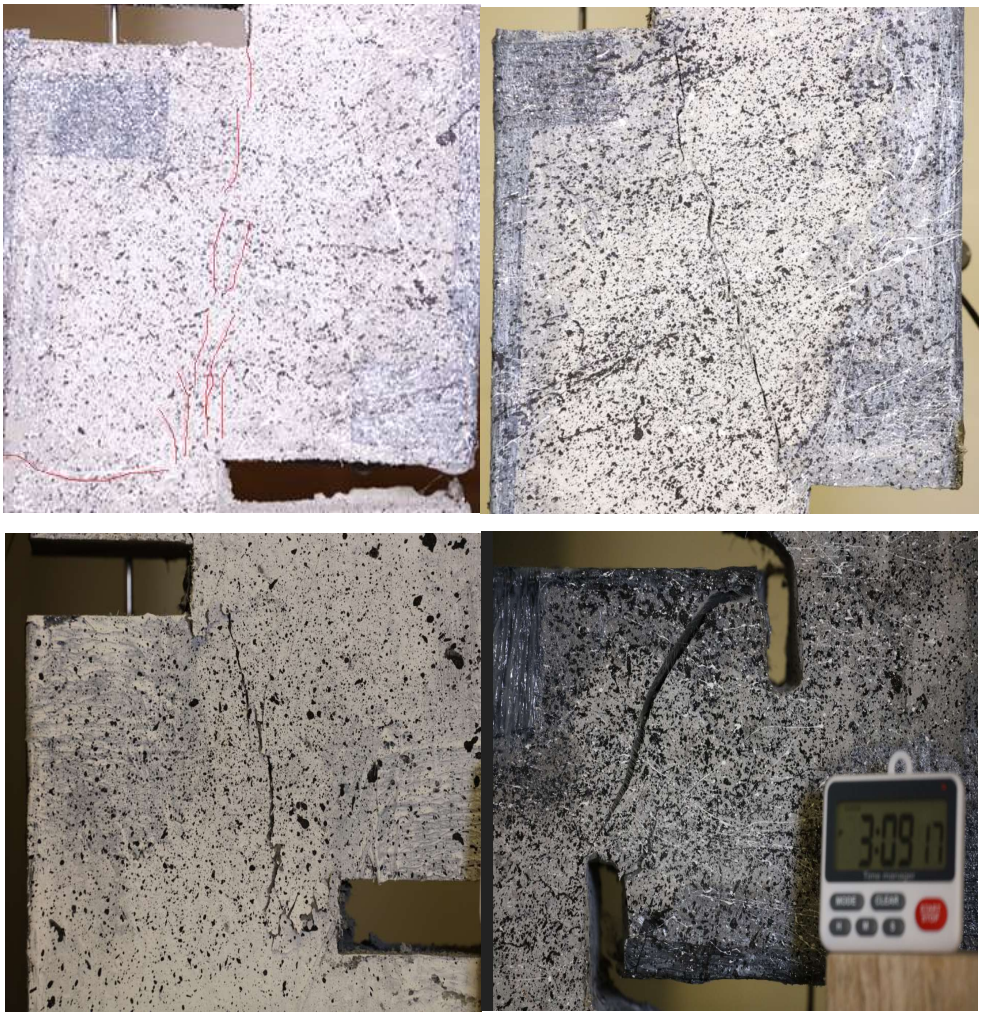

Figure 6.17: Push-off Specimens failure cracks (PS-S2; CS-S2; CS'-S2; TS-S2)

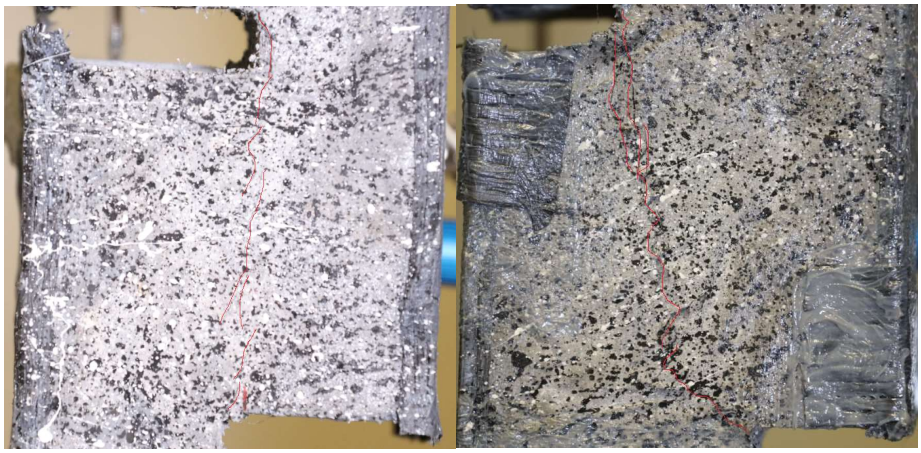

Figure 6.18: Half Scale Push-off Specimens failure cracks (SPS-S1; SCS-S1)

Figure 6.19: Half Scale Push-off Specimens failure cracks (SPS-S2; SCS-S2)

6.3.4.2 Digital Image Correlation (DIC) Analysis

For all push-off specimens, DIC analysis was undertaken and load-displacement curves were plotted as can be seen in Figure 6.20. The quality of pictures taken from SPS-S2 and SCS-S1 were not acceptable and no DIC analysis could be conducted for those specimens. Load versus vertical relative displacement curves of the two faces of the shear planes were also plotted using DIC analysis (Figure 6.21).

Although the select speckles were equally distanced as the two mounting points of the LP, and they were at the same position height wise as the LP, as may be seen in the figures, there is a difference in the results of DIC analysis and LPs. This difference is expected since the speckles monitored were on a different face of the specimen that that where the LP was mounted on.

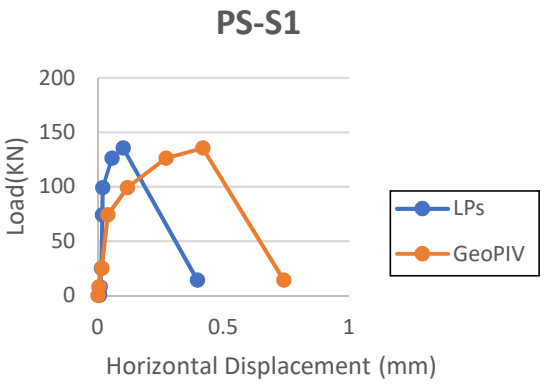
PS-S1
Load(KN)
200
150
100
50
0
0
0.5
1
Horizontal Displacement (mm)
LPs
GeoPIV

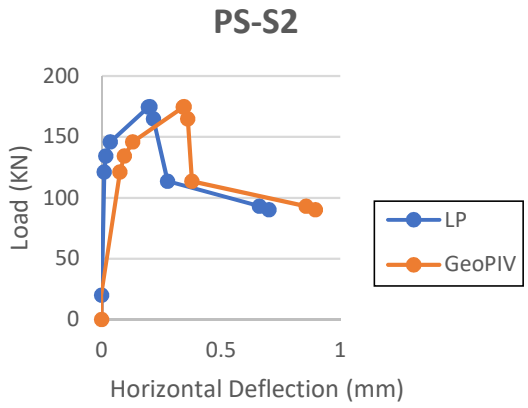
PS-S2
Load (KN)
200
150
100
50
0
0
0.5
1
Horizontal Deflection (mm)
LP
GeoPIV

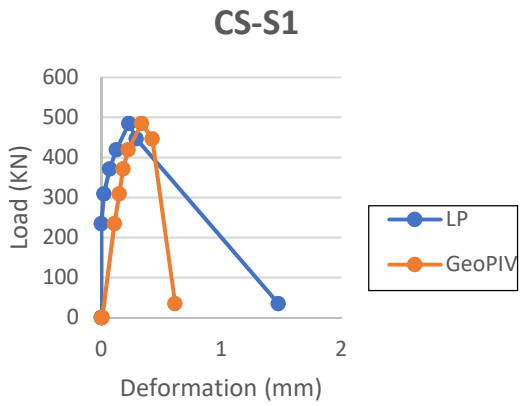
CS-S1
Load (KN)
600
500
400
300
200
100
0
0
1
2
Deformation (mm)
LP
GeoPIV

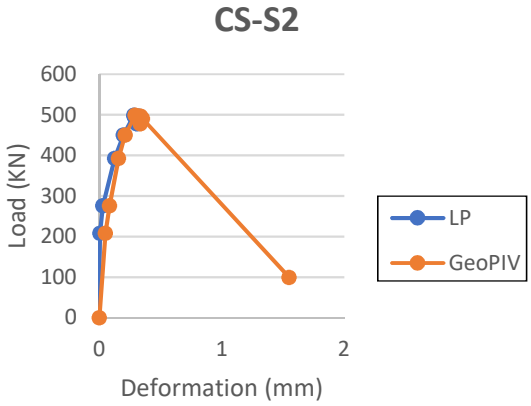
CS-S2
Load (KN)
600
500
400
300
200
100
0
0
1
2
Deformation (mm)
LP
GeoPIV

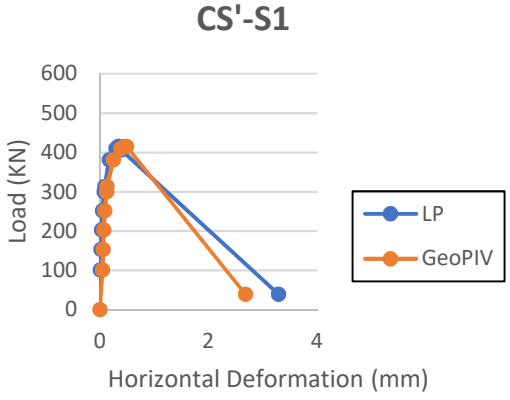
CS'-S1
Load (KN)
600
500
400
300
200
100
0
0
2
4
Horizontal Deformation (mm)
LP
GeoPIV

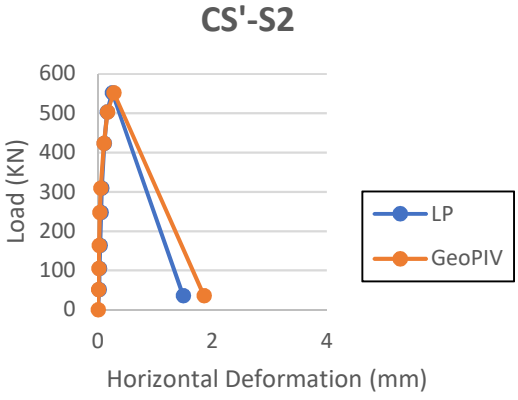
CS'-S2
Load (KN)
600
500
400
300
200
100
0
0
2
4
Horizontal Deformation (mm)
LP
GeoPIV

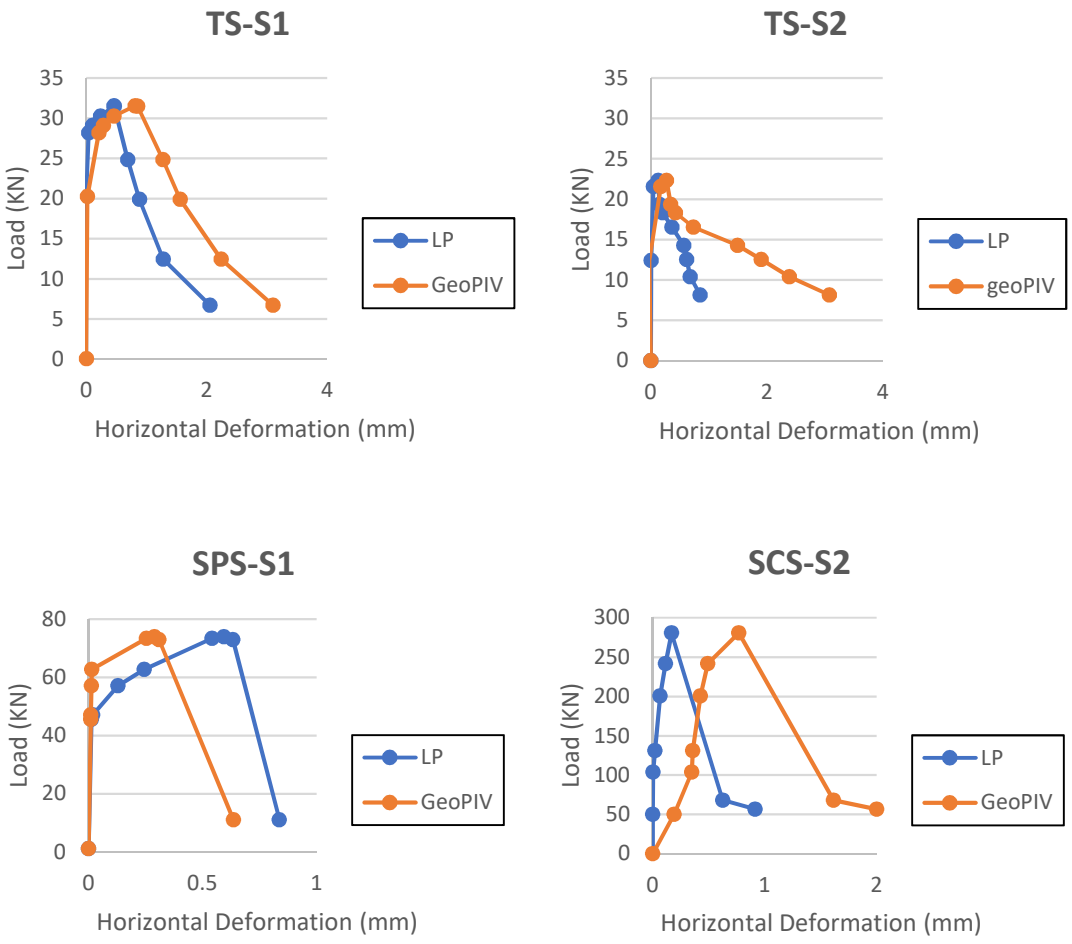

Figure 6.20: Load-displacement curves of push-off specimens from LPs and DIC analysis

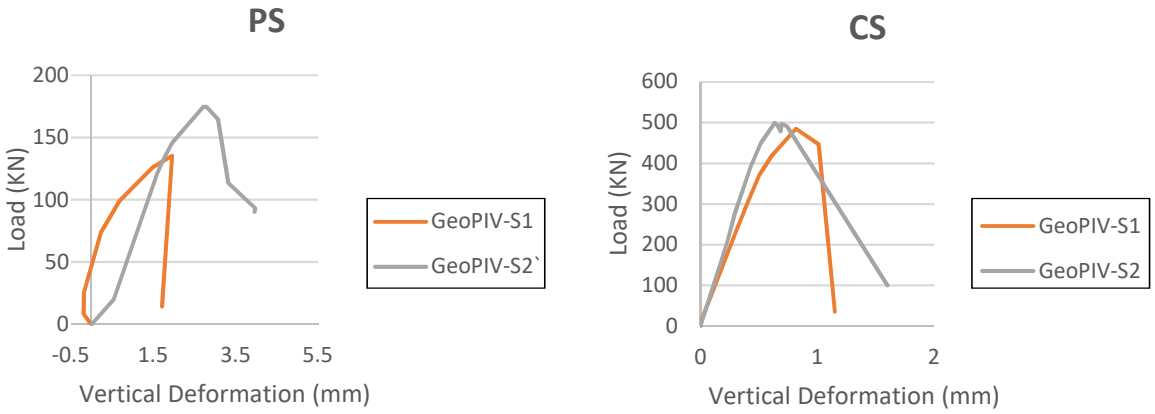

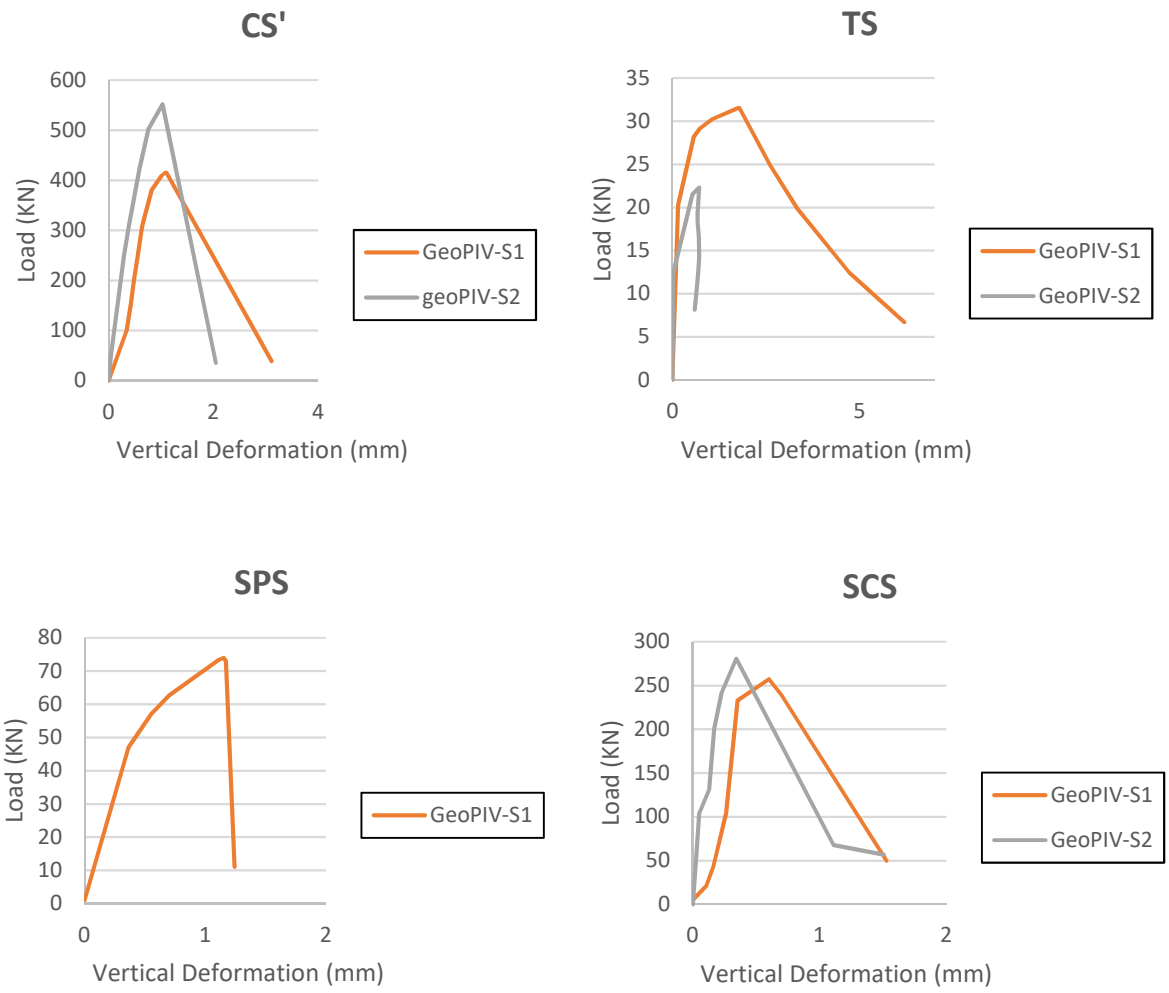

Figure 6.21: Load-vertical displacement of push-off specimens from DIC analysis

6.3.4.3 Data Analysis

The goal of this segment of the experimental program was to derive the τ-σ_n envelope of the SHFRCC that corresponds to a Mohr-Coulomb type of failure envelope. To accomplish this, given the maximum carried load (P), the component of the load normal to the shear plane ($Pcos\alpha$) and parallel to the shear plane ($Psin\alpha$) was determined, where the angle α was the slope of the inclined shear plane ($\alpha = \tan^{-1}$ (vertical distance of the inside edge of the notches / horizontal distance of inside edges of the notches). The applied stresses were obtained by dividing these components by the area of the shear plane as can be seen in Table 6.6.

Table 6.6: Normal and Tangential stresses of push-off specimens

	P (KN)	τ (MPa)	σ (MPa)
PS-S1	175.1	8.54	0
PS-S2	135.4	6.6	0
CS-S1	500.63	20.47	8.99
CS-S2	485.73	19.82	8.7
CS'-S1	551.85	47.57	19.03
CS-S2	415.41	35.81	16.32
TS-S1	31.54	-1.86	-1.86
TS-S2	22.34	-1.31	-1.31
Half scale PS-S1	73.97	7.4	0
Half scale CS-S1	281.23	23.4	10.5
Half scale CS-S2	257.98	21.45	9.65

The τ-σ curve has been drawn for the average value of stresses (Figure 6.22). Blue dots represent full scale push-off specimens; orange dots and gray dots represent half scale pure shear and compression shear specimens, respectively. As may be seen, in case of pure shear no size effect is evident. And for compression shear specimen there is a small difference which may be clearly owing to experimental error.

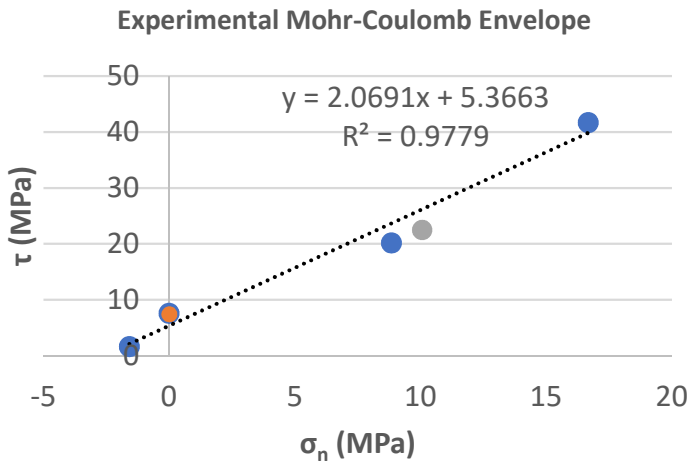

Figure 6.22: Mohr-Coulomb envelope of the push-off specimens

6.3.4.4 Finite Element Analysis

Finite Element (FE) modelling of the push-off specimens were undertaken using the FE software platform VecTor2 (2017) developed at the University of Toronto to investigate the cracking behaviour observed in the tests.

The 2-D mesh used in the analysis comprised a grid of 10 × 10 four-nodded elements, endowed with two translational degrees of freedom per node (eight degrees- of-freedom per rectangular finite element). Reinforcement required to suppress tension failures in the perimeter of the specimens were modeled using truss bar elements. The support condition at the specimen centerline was to fully restrain the node at the specimen centerline at the base, and to restrain the corresponding top node from x and z (out of plane) displacement. All other nodes at the base and at the top were unrestrained in x and z but restrained in the y (at y=0) and set to displacement –Δ at the top surface. The load was applied in a displacement control system monotonically with increment factors of 0.1 mm.

It was decided to model the push off specimens with the properties of the SHFRCC with perimeter reinforcement so as to avoid non-convergence in the analysis. The objective was to find the regions that are in tension to be strengthen with FRP and get an estimation of the maximum load carried by each specimen. Specified material properties in VecTor2 (2017) are summarized in Table 6.7 and Table 6.8. The constitutive models chosen for specimens are shown in Table 6.9.

Table 6.7: Concrete properties in Vector2

	t (mm)	f'_c **(MPa)**	d_g **(mm)**
Material1	100	60	0.3

Table 6.8: Truss Elements Properties in VecTor2

	A_s (mm^2)	d_b (mm)	f_y (MPa)	f_u (MPa)	E_s (GPa)	ε_{sh}	ε_u
Reinforcement1	100	10	500	600	200	10	150

*ε_{sh}: strain hardening strain; ε_u: ultimate strain

Table 6.9: Constitutive models

Compression PrePeak	Hognestad (Parabola)	**Dilation**	Variable - Kupfer
Compression PostPeak	Modified Park-Kent	**Cracking Criterion**	Mohr-Coulomb (Stress)
Compression Softening	Vecchio 1992-A	**Crack Stress Calc**	Basic (DSFM/MCFT)
Tension Stiffening	Modified Bentz 2003	**Crack Width Check**	1 mm Max Crack Width
Tension Softening	Bilinear	**Crack Slip Calc**	Walraven (Monotonic)
FRC Tension	SDEM - Monotonic	**Hysteretic Response**	Nonlinear w/ Plastic Offsets
Confined Strength	Kupfer/Richart		

Finite Element Models of the specimens and the crack pattern when failed are presented in Figure 6.23. Load-displacement curves are also given in Figure 6.24.

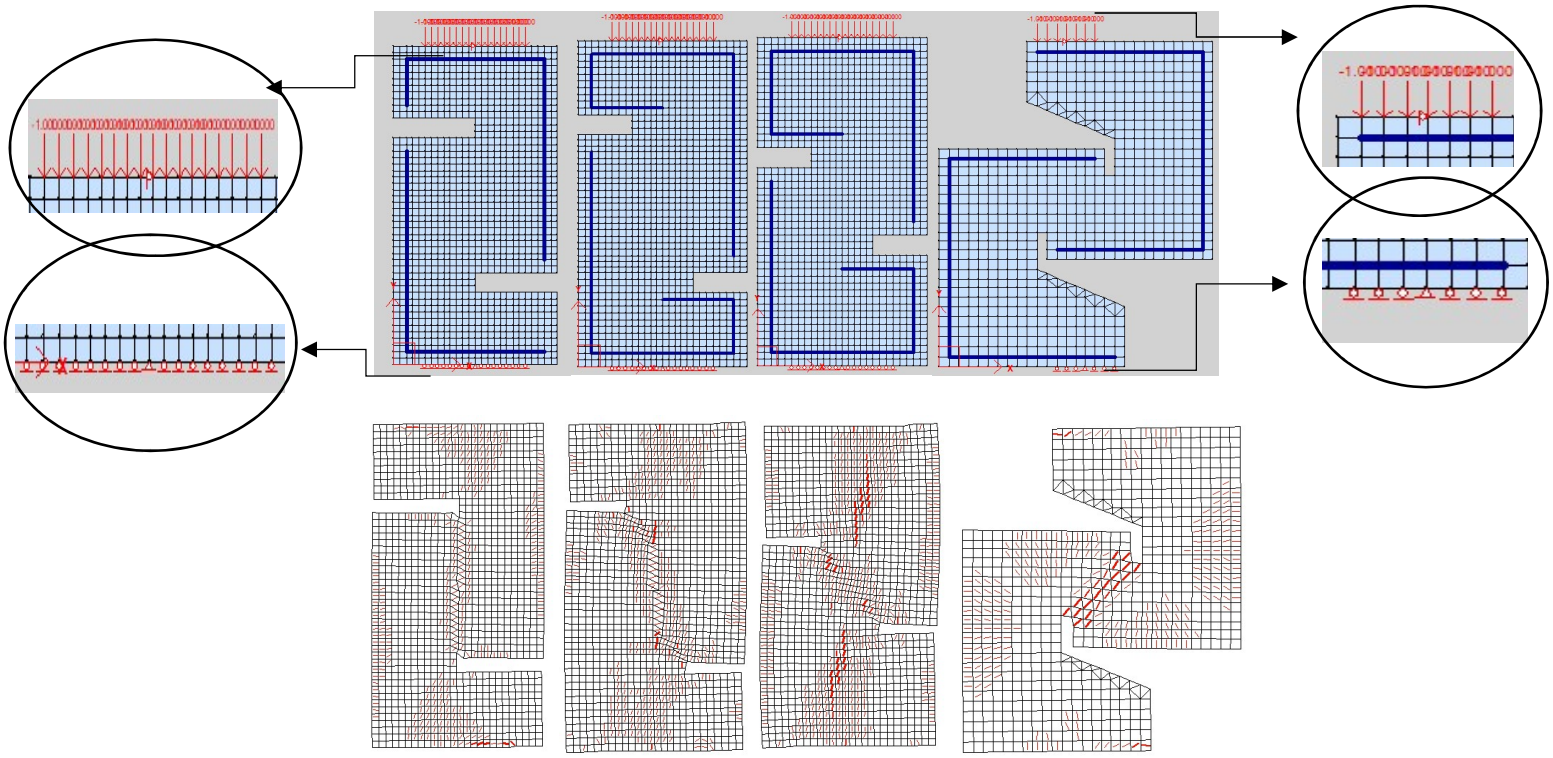

Figure 6.23: Finite Element Models of the push off specimens and the crack pattern when failed

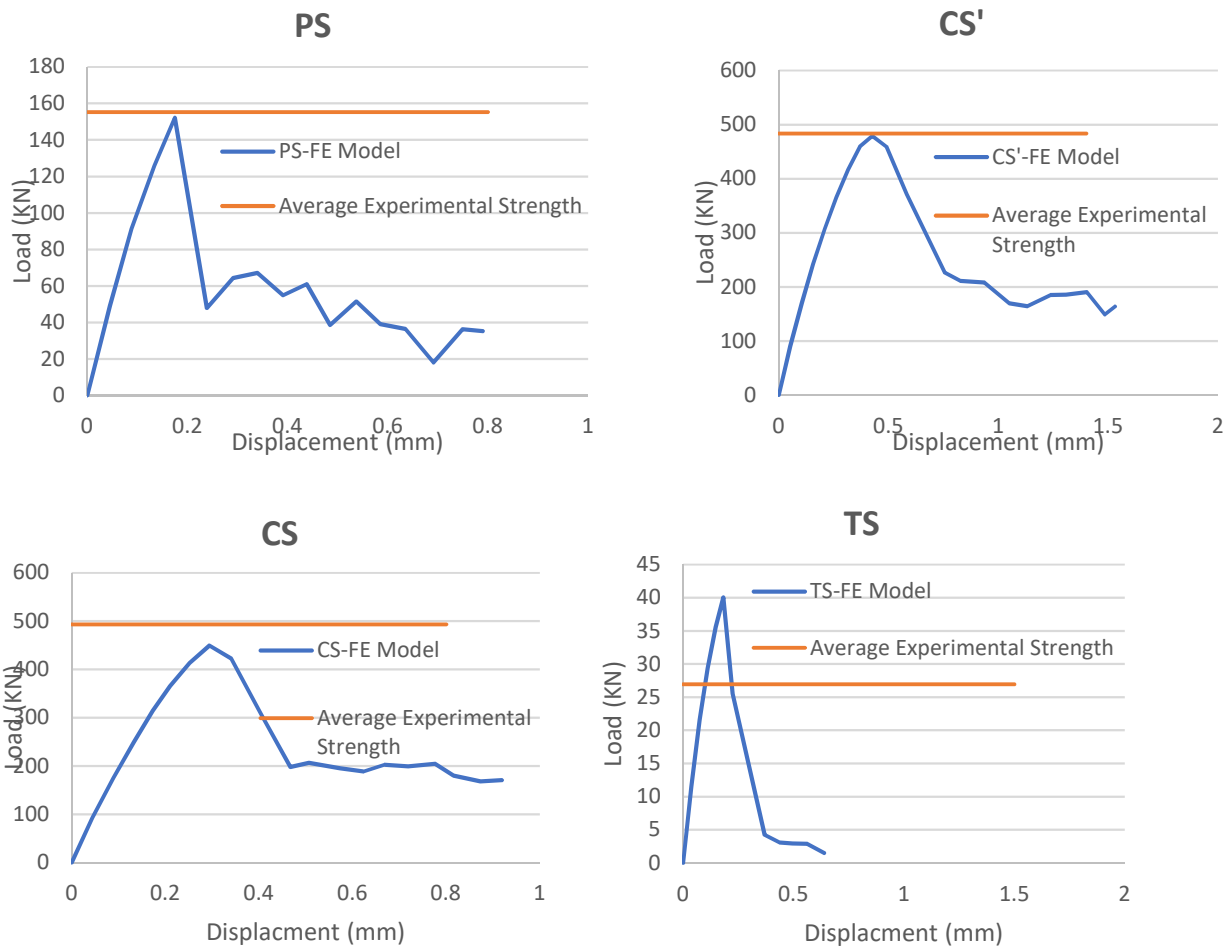

Figure 6.24: Load-displacement curves of Push-off specimens

In all cases the crack pattern matched what we got from the experiment and the maximum capacity of members were almost the same in FE models and what we got from the experiment with the exception of the TS specimens in which due to the overexpressed anti-symmetry the spherical seats rotated slightly introducing undesirable torsion. This gave us premature failure. We believe therefore that this is the reason why the results of the experiment were below what we got from the FE model when using as input the general stress strain law that was measured from the tensile tests.

6.3.5 Four-point Bending Tests of Full-scale SHFRCC beams

In this section, the results of the four-point bending tests performed on reinforced concrete SHFRCC beams (Figure 6.25) are discussed. Beams were cast from Mix 3 (M3) (dimensions: 915×150×150 mm). Details of the setup were given in section 5.7.4.2.

Figure 6.25: Four-point bending test on the full scale SHFRCC beam

6.3.5.1 Test Observations

Beam 1 (B1) with a loading distance of 150 mm, a shear span of 210mm (a/d=1.87), and anchorage length of 9.5 D_b beyond the support was loaded under displacement rate of 0.005 mm/s to a mid-deflection of 20mm. The load-displacement curve is given in Figure 6.26 with an orange-colored line. The maximum load was 245.01KN and the duration of the tests was 61.5 min.

Beam 2 (B2) with a loading distance of 300 mm, again a shear span of 210 mm, and an anchorage length of 4.8 D_b beyond the support was tested under the same displacement rate (0.005 mm/s) to a maximum displacement of 20mm. The load-displacement curve is given by the blue line in Figure 6.26. The maximum load was 216.19 KN and the test duration was 73.86min.

Figure 6.27 shows the failure patterns of both SHFRCC beams.

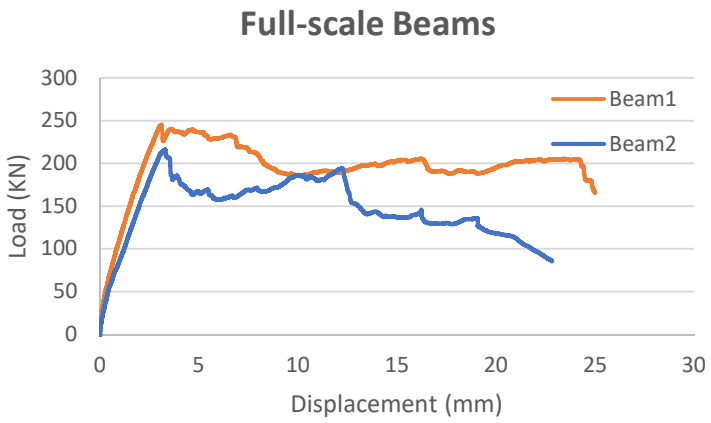

Figure 6.26: Load-Displacement curve of full-scale SHFRCC beams

(a) (b)

Figure 6.27: Beam failure patterns: (a) B1 and (b) B2

From a closer look in Figure 6.28, it is concluded that beam B2 failed along the anchorage in a manner very familiar with what is observed in conventional concrete beams without stirrups. On the other hand, in B1 a fan of shear cracks extending from the point load toward the bottom reinforcement dominated a great range of the test. Only towards the end of the test, very fine bond splitting cracks propagated along the bar in the case of specimen B1 towards the support. Both beams showed very ductile behaviour reaching remarkable midpoint displacements (10mm) but beyond that specimen B2 gradually lost its strength, whereas beam B1 continued to sustain at least 80% of its peak load to more than 25mm midspan deflection.

Crushing failure of the concrete compression zone was observed at these excessive levels of displacement.

(a) (b)

Figure 6.28: Failure cracks of the right shear spans of (a) B1 and (b) B2

CHAPTER 7: SHEAR DESIGN PROVISIONS FOR SHFRCC IN VARIOUS RECOMMENDATIONS, STANDARDS, AND STUDIES

7.1 Introduction

In the last few decades, many research studies around the world were dedicated to the development of Fiber Reinforced Cementitious Composites (FRCC) that are commercially available (proprietary products) in the market nowadays. Shear strength of FRCC has been among the research priorities and a few models have been proposed to calculate the concrete contribution term of FRCC. Of those some are empirical or semi-empirical, whereas others are based on mechanistic constructs. In this chapter, two different mechanical models have been selected to interpret the mechanics of Strain Hardening FRCC in shear. Section 7.5 summarizes the shear strength recommendations based on five different international codes. Furthermore, a database of PVA-Strain Hardening Cementitious Composites beams tested under shear and flexure is presented along with analysis of the collected data.

7.2 Model I – Shear Contribution due to Bond & Development in SHFRCC (Georgiou & Pantazopoulou 2017)

All models can be classified into two categories. In the first category, fiber contribution to shear strength is believed to be separate from the concrete contribution and the general format is written as follows:

$$V = V_c + V_f + V_{st} \tag{7.1}$$

The second category assumes that the fibers enhance the concrete contribution and their influence is considered implicitly.

$$V = V_{FRC} + V_{st} \tag{7.2}$$

The model by Georgiou and Pantazopoulou (2017) belongs in the latter category. In this approach, shear strength is interpreted using the engineering beam theory (for flexural specimens) whereas strut-and-tie models were used for lower aspect ratios (a/h < 2).

- **Engineering Beam Theory – its Relevance to Shear Contribution**

The basic element of the Engineering beam theory that is used here is the method of calculating shear flow between horizontal layers of a member from equilibrium of normal stresses of two adjacent cross sections. With reference to Figure 7.1, this concept may be applied for the segment of the member that is bounded between the free surface on the compression side and the tension reinforcement (Georgiou and Pantazopoulou 2017).

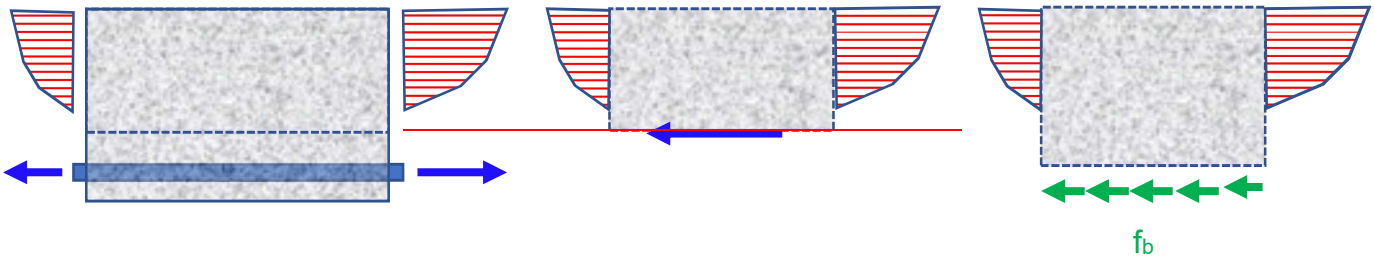

Figure 7.1: (a) Dual Sections; (b) Definition of shear stress from dual-section equilibrium. (c) Extending the concept to bond based on dual section analysis from the compression fiber to the level of tension reinforcement

The familiar layered model of Figure 7.1 is modified further to account a stress block on the tension zone of each critical section, since the SHFRCC sustains its tensile strength past the onset of cracking, as depicted in Figure 7.2.

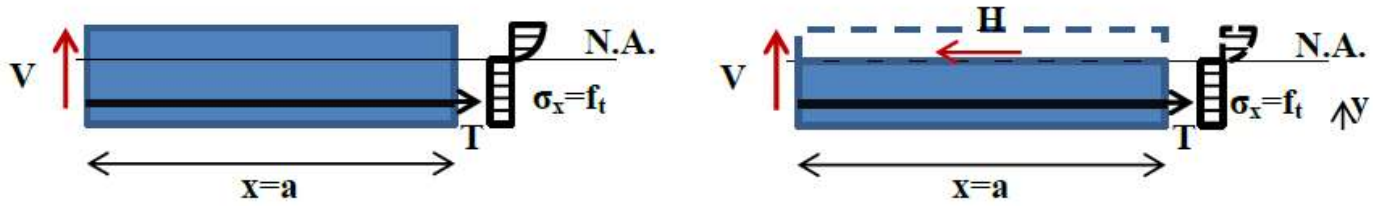

Figure 7.2: (a) Beam segment of length Δx=a with the normal stresses and (b) horizontal cross section of the lower part (tension zone) based on beam theory for calculation of the shear flow q=ΔH/Δx (Georgiou and Pantazopoulou 2017)

$$V = \pi d_b n_b f_b \left(\frac{1}{3}y - c_1 + \frac{2}{3}h\right) + b\frac{f_t\, y}{a}\left(\frac{4h-y}{6}\right) \quad (7.3)$$

From models regarding bond – slip behavior of anchored reinforcement it is well established that the bond strength may be obtained with due consideration to the amount of confinement supplied by stirrups and cover – here the cover presents internal confinement on account of the fiber content. The theoretical bond strength (local value) is obtained from Eq. (7.4):

$$f_b = \frac{2\mu}{\pi}(\sigma_c + \sigma_{st}) = \frac{2\mu\, f_t}{\pi\, d_b}(c_1 + \frac{A_{st}\, e\, f_{y,st}}{n_b.\, f_t.s_{st}}) \;=\; 0.57\,\frac{c_1}{d_b} f_t + 0.19\,\frac{A_{st} f_{y,st}}{n_b d_b s_{st}} \qquad (7.3)$$

where a value for the frictional coefficient equal to μ=1.1 has been assumed. In the absence of stirrups, the bond strength of SHFRCC is taken as $0.57\,\frac{c_1}{d_b} f_t$.

The direct tensile strength of concrete is estimated from $f_{t,fl}$ obtained indirectly from the 4PB tests conducted on unreinforced beams and a properly calibrated multiplier A_{fl}, based on *fib* Model Code (*fib* 2010).

$$f_t = A_{fl}\, f_{t,fl} \qquad (7.4)$$

where

$$A_{fl} = \frac{a_{fl}\, h_b^{0.7}}{1 + a_{fl}\, h_b^{0.7}} = 0.6 \;\; (a_{fl} = 0.06) \qquad (7.6)$$

$$f_{t.fl} = \frac{M_y}{bh^2/_6} \qquad (7.7)$$

Table 7.1: Notation used in the Model by Georgiou & Pantazopoulou (2017)

$\boldsymbol{d_b}$	Diameter of one reinforcing bar
$\boldsymbol{n_b}$	Number of reinforcing bars (restrained by a stirrup)
$\boldsymbol{f_b}$	Bond strength

$\boldsymbol{y}$	Depth of the tensile region of the cross section is taken here as $\boldsymbol{y} = 0.6\,h$
$\boldsymbol{c_1}$	Clear cover of the reinforcing bars
$\boldsymbol{h}$	Height of the cross section
$\boldsymbol{f_t}$	Tensile strength of the cementitious material; obtained indirectly by the four-point bending tests conducted on unreinforced beams as per the Model Code
$\boldsymbol{a}$	Beam segment of length $x = a$
$\boldsymbol{\mu}$	Coefficient of friction for deformed steel is taken $\mu = 0.9$
e	Coefficient averages stirrup-induced confining pressures over the spacing s is taken e=0.33
$\boldsymbol{s_{st}}$	Spacing of stirrups
$\boldsymbol{A_{st}}$	Area of the stirrups legs crossing the splitting plane
$\boldsymbol{M_y}$	Yielding moment
$\boldsymbol{b}$	Width of the beam.

Upon substitution of the relevant terms it follows that the strength in shear for a SHFRCC member containing no shear reinforcement is approximated based on the Engineering Beam Theory as

$$V = \left[1.8\, d_b n_b \cdot \frac{c_1}{d_b} \cdot (0.87\mathrm{h} - \ c_1) + 0.36 b \frac{h^2}{a}\right] \cdot f_t \qquad (7.8)$$

- Strut-and-Tie Approach

For beams with a short span, the engineering beam theory described in the preceding underestimates the shear force. That is because a major fraction of the sustained force is driven to the supports through diagonal compression, described in the literature as a

strut and tie model. Therefore, the equations listed below govern the response (Georgiou and Pantazopoulou 2017):

$$V = T\ tan\vartheta \tag{7.9}$$

T is the ultimate strength of the tension tie and is calculated as:

$$T = \alpha \cdot f_t \cdot b \cdot (h - c) \approx \alpha \cdot f_t \cdot b \cdot 0.6h \tag{7.10}$$

where c is the depth of compression zone and α is a coefficient to account for the shape of the normal tensile stress block in the tension zone ($1/2 \leq \alpha \leq 1$). Angle ϑ is calculated from a postulated strut and tie model as shown in Figure. 7.3 (*a* is the shear span).

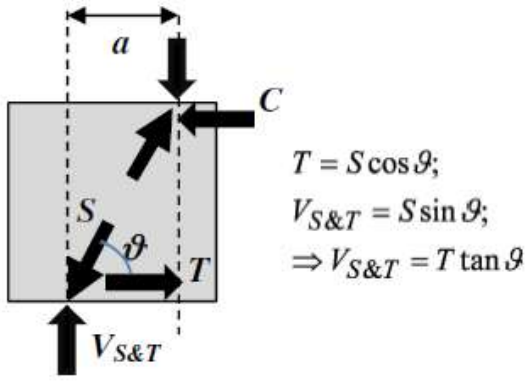

Figure 7.3: Strut-and-tie model (Georgiou and Pantazopoulou 2017)

A comparison of the strength estimates obtained from the two models described above are compared with experimental load values obtained from a test program studying the effect of different parameters on FRCC beams tested under four-point loading: shear span, size of longitudinal bar, presence of fibers or stirrups. The results of comparison of strength estimates for all beams are presented in Figure 7.4, including the flexural strength value at yielding and ultimate expressed as beam load (2 times the support reaction).

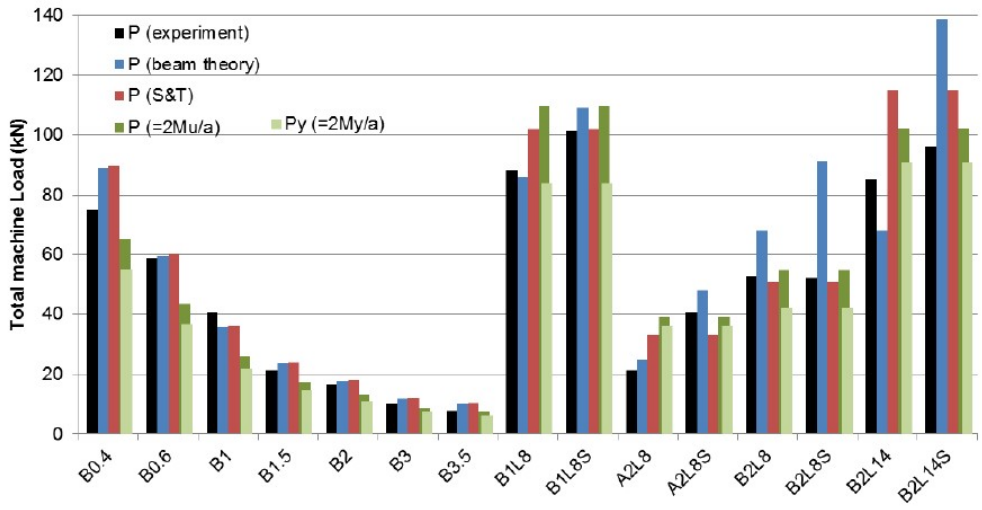

Figure 7.4: Comparison of strength estimates for all specimens (Georgiou and Pantazopoulou 2017)

7.3 Model II: Dinh, Parra-Montesinos & Wight (2011)

In this model (Dinh et al. 2010), shear strength in FRC beams is attributed to contributions by forces transferred through (a) the compression zone and (b) the tension zone, by fibers bridging the diagonal cracks (in their investigation steel fibers were used). Shear carried in the compression zone is estimated by using the failure criterion for concrete subjected to combined compression and shear proposed by Bresler and Pister (1958). The contribution from fiber reinforcement to shear strength is tied to material performance obtained through four-point bending tests conducted as per the ASTM 1609 standard. The two terms contributing to shear strength are calculated as follows:

$$(a)\ V_{cc} = 0.11\, f_c' \beta_1 c\, b = 0.11 \frac{T_s}{0.85} = 0.13\, A_s f_y \tag{7.11}$$

$$(b)\ V_{FRC} = T_f cos\alpha = (\sigma_t)_{ave} b \left(\frac{d-c}{sin\alpha}\right) cos\alpha = (\sigma_t)_{ave} b\,(d-c) cot\alpha \tag{7.12}$$

Where

$$(\sigma_t)_{ave} = \frac{2M}{(h-c)bh} = \frac{2M}{0.9bh^2} \tag{7.13}$$

and $cot\alpha = 45^0$ for simplicity.

Table 7.2: Notation used in the model by Dinh et al. (2011)

V_{cc}	Shear force across the compression region
V_{FRC}	Vertical component of the diagonal tension resistance provided by the fibers
f'_c	Compression strength of concrete
$\beta_1 c$	Whitney's stress block
b	Width of the beam
T_s	Force in the tension reinforcement
A_s	Area of longitudinal reinforcements
f_y	Yielding strength of longitudinal reinforcements
T_f	Tensile force transferred across the critical diagonal crack through fiber tension
$(\sigma_t)_{ave}$	Average tensile stress determined from ASTM 1609
d	Effective depth of the cross section
h	Height of the cross section
M	Moment at the cracked section

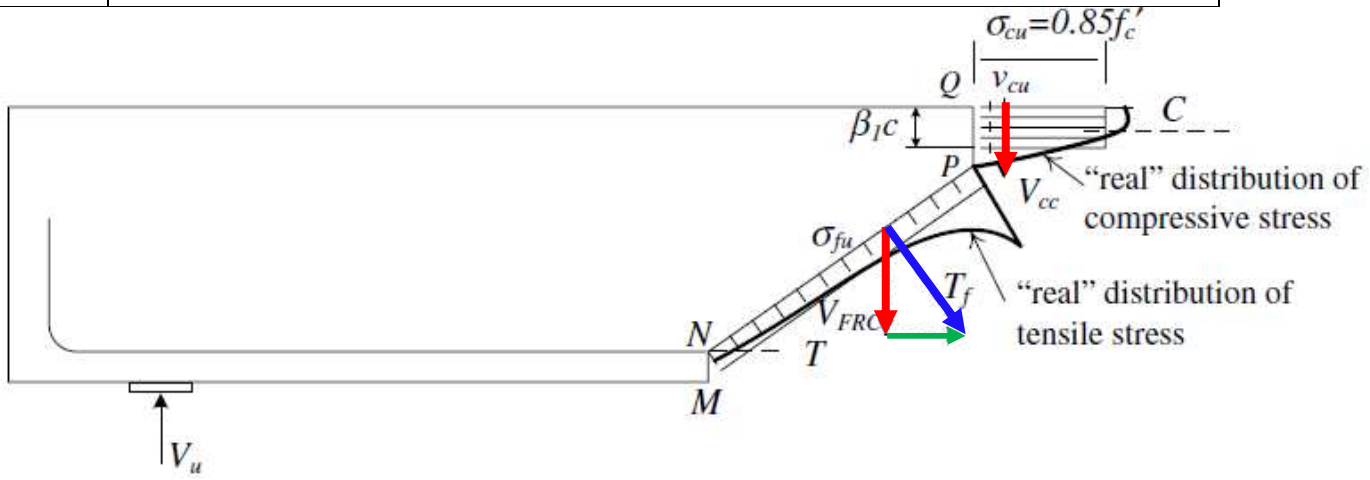

Figure 7.5: Assumed stress distribution in FRC beams: Red arrows represent the contributions to shear in the two zones (compression and tension) (Dinh et al. 2011)

Despite the different origins the equations in this model bear semblance to that one presented previously.

7.4 Codes and Standards

In this section, relevant recommendations for the calculation of shear strength of Fiber Reinforced Concrete in existing codes and guidelines from around the world are outlined.

7.4.1 Model Code 2010

The design value for the shear resistance in members with conventional longitudinal reinforcement and without shear reinforcement is calculated as follows:

$$V_{Rd} = V_{Rd,c} + V_{Rd,F} \quad (7.14)$$

Equation (7.15) is based on steel fiber concrete research for conventional FRC and should be verified if used for other, more advanced types of SHFRCC material.

$$V_{Rd,F} = \left\{ \frac{0.18}{\gamma_c} . k_s . \left[100 . \rho_\ell . \left(1 + 7.5 \frac{F_{Ftuk}}{F_{ctk}} \right) . f_{ck} \right]^{\frac{1}{3}} \right\} . b_w . d \quad (7.15)$$

where k_s is a size effect factor, and ρ_ℓ the ratio of longitudinal tension reinforcement crossing the flexure-shear crack.

$$F_{Ftuk} = f_{Fts} - \frac{w_u}{CMOD_3} (f_{Fts} - 0.5 f_{R3} + 0.2 f_{R1}) \geq 0 \quad (7.16)$$

(refers to the dowel actin of the fibers crossing the flexure-shear crack)

$$f_{Fts} = 0.45 f_{R1} \quad (7.17)$$

$$V_{Rd,Fmin} = v_{min} . b_w . d \quad (7.18)$$

$$v_{min} = 0.035 \, k^{3/2} . f_{ck}^{1/2} \quad (7.19)$$

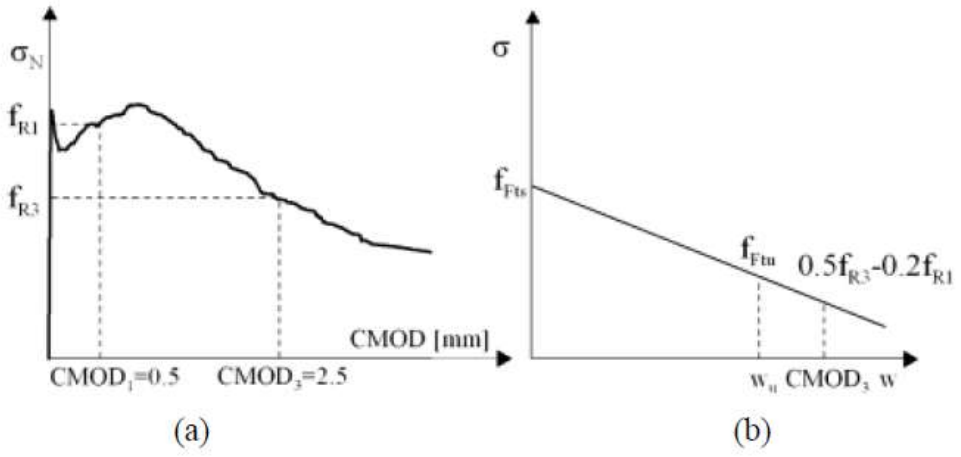

Figure 7.6: (a) Typical results from a bending test on a softening material; (b) Linear post-cracking constitutive law (fib 2010)

Note that these expressions are identical to those used for the concrete contribution term in the older versions of Eurocode 2 for design of conventional reinforced concrete members in shear; the only modifications to these original expressions are in the terms referring to the fiber terms.

Table 7.3: Notation used in New Model Code design expression

$\boldsymbol{V_{Rd,c}}$	Concrete contribution
$\boldsymbol{V_{Rd,F}}$	Fiber contribution
$\boldsymbol{\gamma_c}$	Partial safety factor for the concrete without fibers;
$\boldsymbol{k}$	A factor that takes into account the size effect and it is equal to: $1+\sqrt{\frac{200}{d}} \leq 2.0$
$\boldsymbol{d}$	Effective depth of the cross section, in mm
$\boldsymbol{\rho_\ell}$	Reinforcement ratio for longitudinal reinforcement equal to: $A_{sl}/b_w d$
$\boldsymbol{b_w}$	Smallest width of the cross-section in the tensile zone, in mm.
$\boldsymbol{A_{sl}}$	Cross-sectional area of the reinforcement which extends $\geq \boldsymbol{l_{bd}} + d$ beyond the considered section; in mm^2
$\boldsymbol{w_u}$	Maximum crack opening accepted in structural design (e.g. 0.4mm)

$\boldsymbol{F_{Ftuk}}$	Characteristic value of the ultimate residual tensile strength for FRC, by considering $w_u = 1.5mm$, in MPa; (determined by a direct axial-tensile test (without specifying the procedure, specimen dimensions or testing setup))
$\boldsymbol{f_{R1}}$	Residual strength significant for service condition
$\boldsymbol{f_{R3}}$	Residual strength significant for ultimate condition
$\boldsymbol{F_{ctk}}$	Characteristic value of the tensile strength for the concrete matrix, in MPa;
$\boldsymbol{f_{ck}}$	Characteristic value of cylindrical compressive strength, in MPa;
$\boldsymbol{V_{Rd,Fmin}}$	Minimum shear resistance

7.4.2 The Model by RILEM TC 162-TDF

Again, shear strength comprises contributions from the concrete compression zone and the tension zone owing to fibers that bridge the tension cracks:

$$V_{Rd} = V_{cd} + V_{fd} \tag{7.20}$$

where, the concrete component is identical to what is used in Model Code 2010 for conventional concrete (no fibers).

$$V_{cd} = [\frac{0.18}{1.5}\ k\ (100\rho_1 f_{ck})^{1/3}]b_w d \tag{7. 21}$$

$$k = \ 1 + \sqrt{\frac{200}{d}} \leq 2.0 \tag{7. 22}$$

$$\rho_1 = {}^{A_{sl}}/_{b_w d} \leq 2\% \tag{7. 23}$$

The component associated with the tension zone of the member where the critical crack paths are restrained by fibers is estimated from:

$$V_{fd} = \ 0.7\ k\tau_{fd} b_w d \tag{7. 24}$$

$$\tau_{fd} = 0.12 f_{Rk,4} \tag{7.25}$$

$$f_{Rk,4} = \ 3F_{R,4}L/2bh_{sp}^2 \tag{7.26}$$

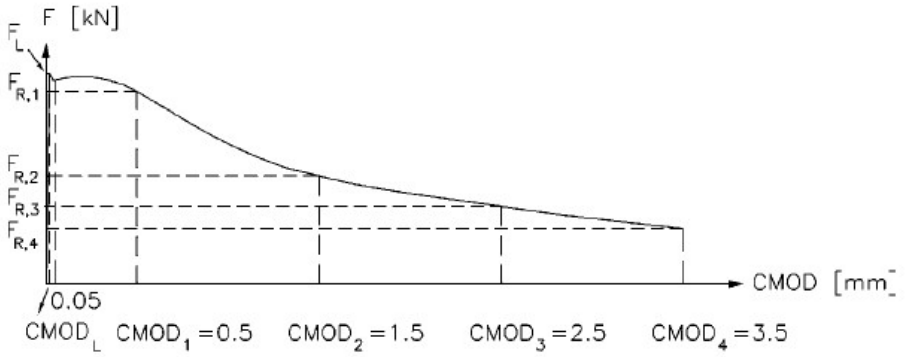

Figure 7.7: Load-CMOD diagram (RILEM TC 162-TDF)

Table 7.4: Notation used in RILEM design expressions

$\boldsymbol{f_{ck}}$	Cylinder strength of concrete
$\boldsymbol{\tau_{fd}}$	Design value of the increase in shear strength in the tension zone due to steel fibers
$\boldsymbol{f_{Rk,4}}$	Characteristic residual flexural tensile strength at the crack mouth opening $\mathrm{CMOD4} = 7.5$ (or $\delta_{R,4} = 3\,mm$) is determined by the CMOD (crack mouth opening displacement) - or deflection controlled bending test on a notched prism according to standards.
$\boldsymbol{F_{R,4}}$	Load recorded at $\mathrm{CMOD_4}$
$\boldsymbol{b}$	Width of the specimen cross section (mm)
$\boldsymbol{h_{sp}}$	Distance between tip of the notch and top of cross section (mm)
$\boldsymbol{L}$	Span of the specimen (mm)

7.4.3 The Model by the Japan Society of Civil Engineers (JSCE, 2008)

Again, this model recognizes a contribution from the concrete in the compression zone and the contribution from the fibers bridging the cracks in the tension zone. The respective terms are calculated from:

$$V_{yd} = V_{cd} + V_{fd} \tag{7.27}$$

$$V_{cd} = \beta_d \beta_p f_{vcd} b_w \, {}^{d}/_{\gamma_b} \quad (7.28)$$

$$f_{vcd} = 0.7 * 0.2 \sqrt[3]{f'_{cd}} \left({}^{N}/_{mm^2}\right), where\ f_{vcd} \leq 0.5\ N/mm^2 \quad (7.29)$$

$$V_{fd} = (f_{vd}\ /tan\beta_u).\, b_w.\, z/\gamma_b \quad (7.30)$$

Table 7.5: Notation used in the JSCE design expression

$\boldsymbol{V_{yd}}$	Design shear capacity of a linear member consisting solely of HPFRCC and reinforcing steel
$\boldsymbol{V_{cd}}$	Design shear capacity of a linear member without any shear reinforcement steels, excluding the strength exerted by reinforcing fiber
$\boldsymbol{V_{fd}}$	Design shear capacity of reinforcing fiber
$\boldsymbol{f'_{cd}}$	Design compressive strength of concrete $({}^{N}/_{mm^2})$
$\boldsymbol{\beta_d}$	$\beta_d = \sqrt[4]{1/d}\,, when \beta_d > 1.5, \beta_d\ is\ taken\ as\ 1.5$
$\boldsymbol{\beta_p}$	$\beta_p = \sqrt[3]{100\,\rho_w}, when \beta_p > 1.5, \beta_p\ is\ taken\ as\ 1.5$ $\rho_w = {}^{A_s}/_{b_w d}$
$\boldsymbol{\gamma_b}$	$\gamma_b = 1.3\ in\ general$
$\boldsymbol{f_{vd}}$	Design tensile yield strength of HPFRCC, $f_{vd} = 0$ when f_{vd} is smaller than $1.5\ N/mm^2$ Determined from uniaxial tensile test (testing method 2)
$\boldsymbol{\beta_u}$	Angle of the diagonal crack surface to the member axis $\beta_u = 45^o$
$\boldsymbol{z}$	Distance from location of compressive stress resultant to centroid of tensile steel (may generally be taken as ${}^{d}/_{1.15}$)

7.4.4 Foster & Agarwal (2014)

A unified model that is applicable to all fiber concrete of all strengths and strain hardening and strain softening, the model by Foster and Agarwal (2014) draws its definition of terms from the general shear design method of the Canadian Code which is based on the

Modified Diagonal Field Theory model by Collins and co-workers (CSA 23.3 2014, Vecchio and Collins 1986)

$$\mathrm{V} = V_{uc} + V_{uf} \tag{7.31}$$

$$V_{uc} = k_v \sqrt{f_c'}\, b_w z \tag{7.32}$$

$$k_v = \frac{0.4}{1+150\ \ _x} \cdot \frac{1300}{1000+\ .7k_{dg}z} \tag{7.33}$$

$$\varepsilon_x = [(M_{Ed}/z)\ + 0.5V_{Ed} \cdot cot\theta]\ /(2E_sA_s) \tag{7.34}$$

$$\theta = 29^0 + 7000\varepsilon_x \tag{7.35}$$

$$k_{dg} = \frac{48}{16+d_g} \geq 1.15 \quad for\ f_c' \leq 70MPa \tag{7.36}$$

$$= 3 \quad if\ f_c' >\ 70MPa \text{ (for light weight concrete)}$$

whereas the term associated with fiber contribution in the tension zone has the form:

$$V_{Rd,f} = k_{fd}.f_{tf}.w.b_w.z.cot\theta \tag{7.37}$$

$$w = 0.2 + 1000\varepsilon_x \geq 0.125mm \tag{7.38}$$

$$f_{tf} =\ K_f\alpha_f\rho_f\tau_b \tag{7.39}$$

$$K_f = \frac{1}{\pi} tan^{-1}[{}^{w_{cr}}/_{\alpha_I l_f}](1 - \frac{2w}{l_f})^2 \tag{7.40}$$

$$\text{if } l_f < l_{crit}\ = \frac{d_f}{2}\frac{\sigma_{fu}}{\tau_b} \tag{7.41}$$

Eq. (7.40) would not apply If Eq. (7.41) is violated (because a portion of the fibers will fracture) In this case, to determine K_f, fiber fracture should be considered (Voo and Foster (2003, 2004, 2009)."

$$\alpha_I = {}^1/_{7.5\alpha_f} \tag{7.42}$$

$$\alpha_f = {}^{l_f}\!/_{d_f} \quad \text{(aspect ratio of the fiber)} \tag{7.43}$$

$$\tau_b = k_b\sqrt{f_c'} \tag{7.44}$$

Table 7.6: Notation used in Foster & Agarwal model (2014)

$\boldsymbol{M_{Ed}, V_{Ed}}$	Design values of stress resultants determined from the factored design loads
$\boldsymbol{A_s}$	Cross-sectional areas of the reinforcing steels
$\boldsymbol{E_s}$	Elastic modulus of the reinforcing steels
$\boldsymbol{z}$	Internal moment lever arm (and is taken as z = 0.9d, where d is the effective depth of the section
$\boldsymbol{d_g}$	Maximum size of the aggregate particles
$\boldsymbol{V_{Rd,f}}$	Fiber contribution to the shear strength
$\boldsymbol{w}$	Crack width at the mid-height on the section
$\boldsymbol{k_{fd}}$	Fiber orientation and dispersion variability factor; taken here as 0.8
$\boldsymbol{f_{tf}}$	Tensile strength provided by the fibers over a plane of unit area
$\boldsymbol{K_f}$	Global fiber orientation factor
$\boldsymbol{w_{cr}}$	Current crack opening displacement
$\boldsymbol{l_{crit}}$	Critical fiber length for fiber fracture
$\boldsymbol{\sigma_{fu}}$	Tensile strength of the fiber
$\boldsymbol{\alpha_I}$	Fiber engagement coefficient
$\boldsymbol{l_f}$	Fiber length
$\boldsymbol{d_f}$	Fiber diameter
$\boldsymbol{\alpha_f}$	Aspect ratio of the fiber
$\boldsymbol{\rho_f}$	Volumetric ratio of fibers
$\boldsymbol{\tau_b}$	Bond stress between the fibers and the concrete matrix

$\boldsymbol{k_b}$	a bond factor determined by the fiber and matrix type 0.8 for end-hooked steel fibers, 0.6 for crimped steel fibers and 0.4 for straight steel fibers in normal and high strength concrete; for UHPFRC it is 1.0 for end-hooked steel fibers, 0.8 for crimped steel fibers and 0.6 for straight steel fibers
$\boldsymbol{f'_c}$	the compressive cylinder strength

7.4.5 The provisions of the ACI318-14

Here the concrete contribution term, calculated over the members' web cross section is given by:

$$V_c = 0.17\lambda\sqrt{f'_c}\, b_w d \tag{7.45}$$

unless a more detailed calculation is made in accordance with Table 7.7.

Table 7.7: Detailed method for calculating V_c (ACI318-14)

$\boldsymbol{V_c}$		
Least of (a), (b), (c):	(a)	$(0.16\lambda\sqrt{f'_c} + 17\rho_w \frac{V_u d}{M_u})b_w d$ (7.5)
	(b)	$(0.16\lambda\sqrt{f'_c} + 17\rho_w)b_w d$ (7.6)
	(c)	$0.29\lambda\sqrt{f'_c}\, b_w d$ (7.7)

M_u occurs simultaneously with $V_u$at the section considered.

$$\frac{V_u d}{M_u} = \frac{d.P/2}{Pa/2} = d/a \tag{7.46}$$

7.5 Analysis and Investigation of PVA-ECC Shear Database

In the following section, the intention is to give a summary of all research studies that have investigated the shear strength of PVA-Engineered Cementitious Composites in rectangular beams containing only longitudinal steel reinforcement and no transverse reinforcement and to collect all relative data in a database format. For this purpose, a database containing information about the shear strength of 17 PVA-ECC beams found in published literature is collected. The specimens were tested under combined flexure and shear in different studies conducted at the University of Cyprus, the Technical University of Denmark, Hohai University (China), the University of Tsukuba (Japan), and Ryerson University (Canada). In all mentioned studies, improvement of shear strength of FRCC beams were reported. The complete database is presented in Appendix C.

7.5.1 Georgiou & Pantazopoulou (2017)

In the study conducted by Georgiou & Pantazopoulou (2017) a total number of 51 small-scale beams were tested under four-point bending among which four beams meet the required criteria to be included in the PVA database (Figure 7.8). The identification code of the specimens contained four-digits as follows: First digit: A (no fiber-High Volume Fly Ash mix (HVFA)), B (with Fiber- Strain Hardening Cementitious Composites (SHCC)); second digit: shear span aspect ratio ($^{a}/_{h}$); third Digit: L (indication of the presence of longitudinal reinforcement); fourth digit: size of longitudinal bar in mm. Beams were extended 50mm over the supports to provide enough anchorage of longitudinal reinforcements.

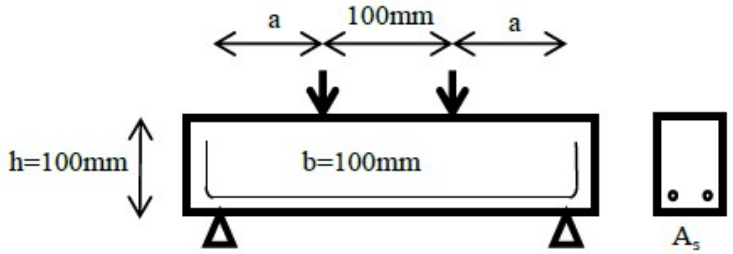

Figure 7.8: Test configuration for four-point bending and reinforcement details for beams with flexural reinforcement (Georgiou & Pantazopoulou 2017)

Dog-bone tests (with sectional dimensions 50×25mm) were conducted to obtain the tensile stress-strain response of SHFRCC.

7.5.2 Paegle & Fischer (2016)

The shear beam test set up by Ohno (1957) depicted in Figure 7.9 is chosen to study the shear in the beams. Only one Engineered Cementitious Composite (ECC) beam that does not have any shear reinforcement in the “area of interest” is selected to be included in this PVA data base.

Dog-bone tests (with sectional dimensions 50×25mm) were conducted to get the tensile stress-strain response of ECC and splitting tensile tests were done according to EN 12390-6.

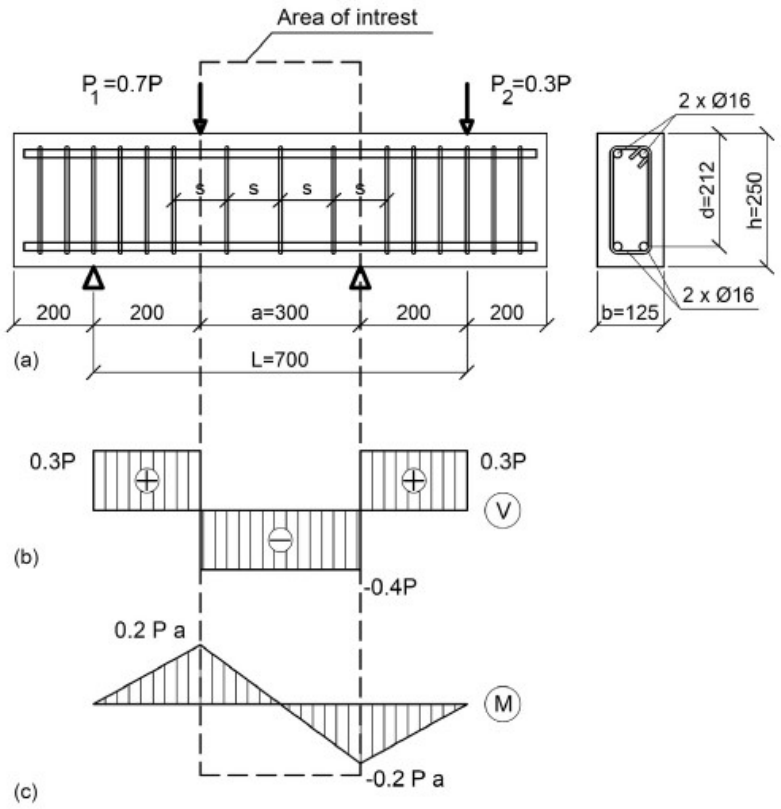

Figure 7.9: (a) Shear beam test setup configuration, (b) shear force distribution, (c) moment distribution (Paegle & Fischer 2016)

7.5.3 Hou et al. (2015)

A total of 14 beams (8 ultra-high toughness cementitious composite (UHTCC) beams denoted by “U” and 6 Reinforced Concrete (RC) beams denoted by “C”) were tested under a three-point loading system (Figure 7.10). Three beams with no web reinforcement ratio ($w0$) with three different shear span aspect ratios (2.06, 3.08, 7.11) were selected to be included in the PVA data base.

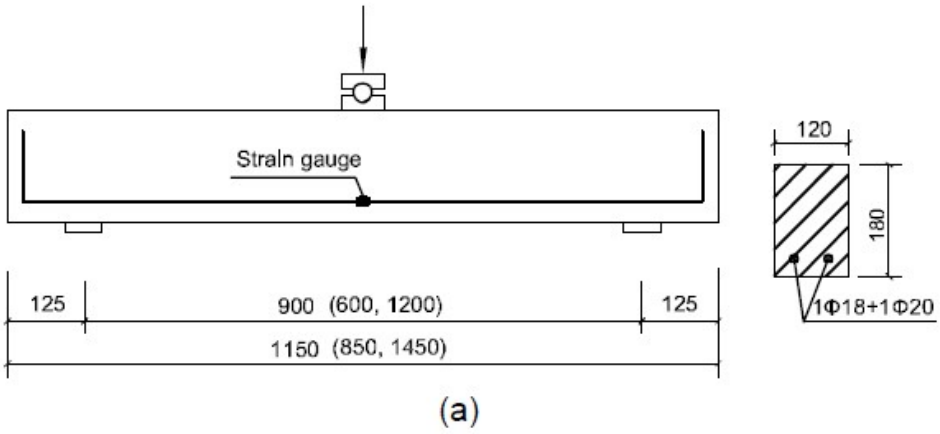

Figure 7.10: Geometry and reinforcement configuration of beams tested without stirrups (Hou et al., 2015)

Thin plate specimens (350 mm long, 50 mm wide, and 15 mm thick) were used to measure the uniaxial tension property of UHTCC. Splitting tensile strength ($f_{sp)}$ was also obtained using 100 mm^3 specimens.

7.5.4 Shimizu (2004)

PVA-ECC beams with shear span ratio of 1.5 and different volume ratios of PVA fiber (1%, 1.5%, 2%) were tested using the setup proposed by Ohno (1957) (Figure 7.11). Only those that do not have any stirrups in their “area of interests” are selected to be under investigation in the present study.

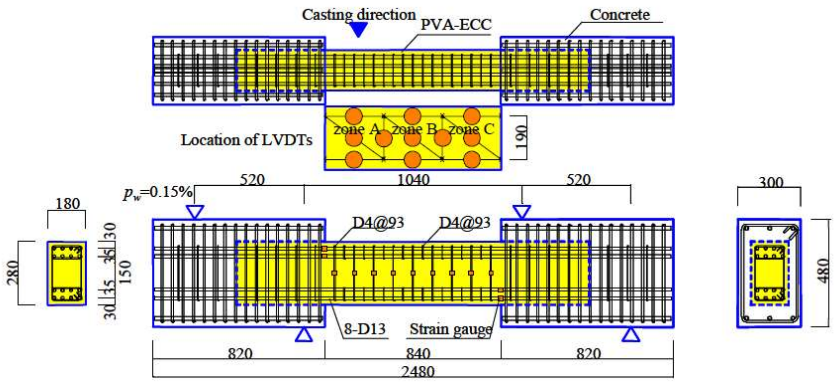

Figure 7.11: Dimension and bar arrangement of beam specimen (Shimizu 2004)

Uniaxial tensile tests were also conducted using dog-bone specimens (sectional dimension 100×60mm).

7.5.5 Alyousif et al. (2015)

Twelve concrete beams (6 ECC beam and 6 Normal Concrete (NC)) were tested under four-point bending loading system (Figure 7.12). Series A beams have 2 @ Φ16 and series B have 4 @ Φ16. Those six ECC beams were selected to be under investigation in this study (Figure 7.12).

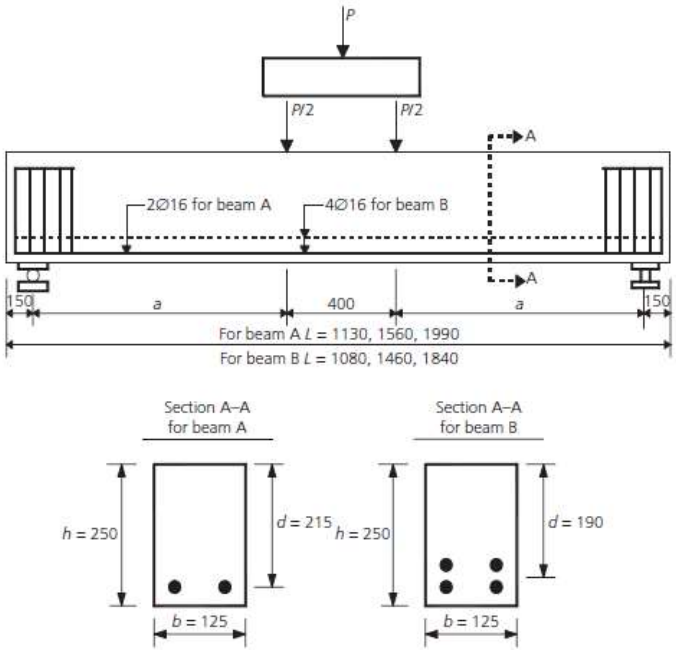

Figure 7.12: Reinforcement details of specimens (dimensions in mm) (Alyousif et al. 2015)

7.5.6 Data Analysis and Discussion

All required parameters to calculate shear strength of beams based on four different recommendations (Model code 2010, RILEM TC 162, JCSE (2008), ACI-318-14) have been collected from the database. The summary of all calculations according to the 4 design models are listed in Table 7.8 Yielding tensile strength and ultimate tensile strength of beams were considered either as was reported by authors (from different experimental tests) or a nominal value was assumed. Figure 7.13 depicts performance of these four different code provisions against the PVA database.

Table 7.8: Calculated shear strength values (in KN) for specimens considered in Data base

Beams	V_{exp}	V_{MC}	V_{RILEM}	V_{JSCE}	V_{ACI}
B1L8	47.20	35.53	15.80	17.86	10.94
B2L8	26.35	35.53	15.80	17.86	10.08
B2L14	42.66	51.6	21.05	18.29	11.84
R/ECC-0	150	126.81	58.29	73.97	35.92
U2-w0	95.86	119.19	46.83	38.06	25.92
U3-w0	66.6	118.46	46.6	38.06	23.5
U4-w0	50.67	118.46	46.6	38.06	22.36
PVA10	123.9	223.35	91.39	80.31	58.42
PVA15	142.8	222.06	89.41	76.41	57.49
PVA20	182.7	235.36	98.66	105.91	59.44
beam 1A	250.73	127.81	53.1	57.01	36.96
beam 1B	275.45	147.43	58.98	51.35	40.29
beam 2A	110.33	127.81	53.1	57.02	33.55
beam 2B	145.41	147.43	58.98	51.35	33.46
beam 3A	71.63	127.81	53.1	57.02	32.42
beam 3B	95.29	147.43	58.98	51.35	31.18

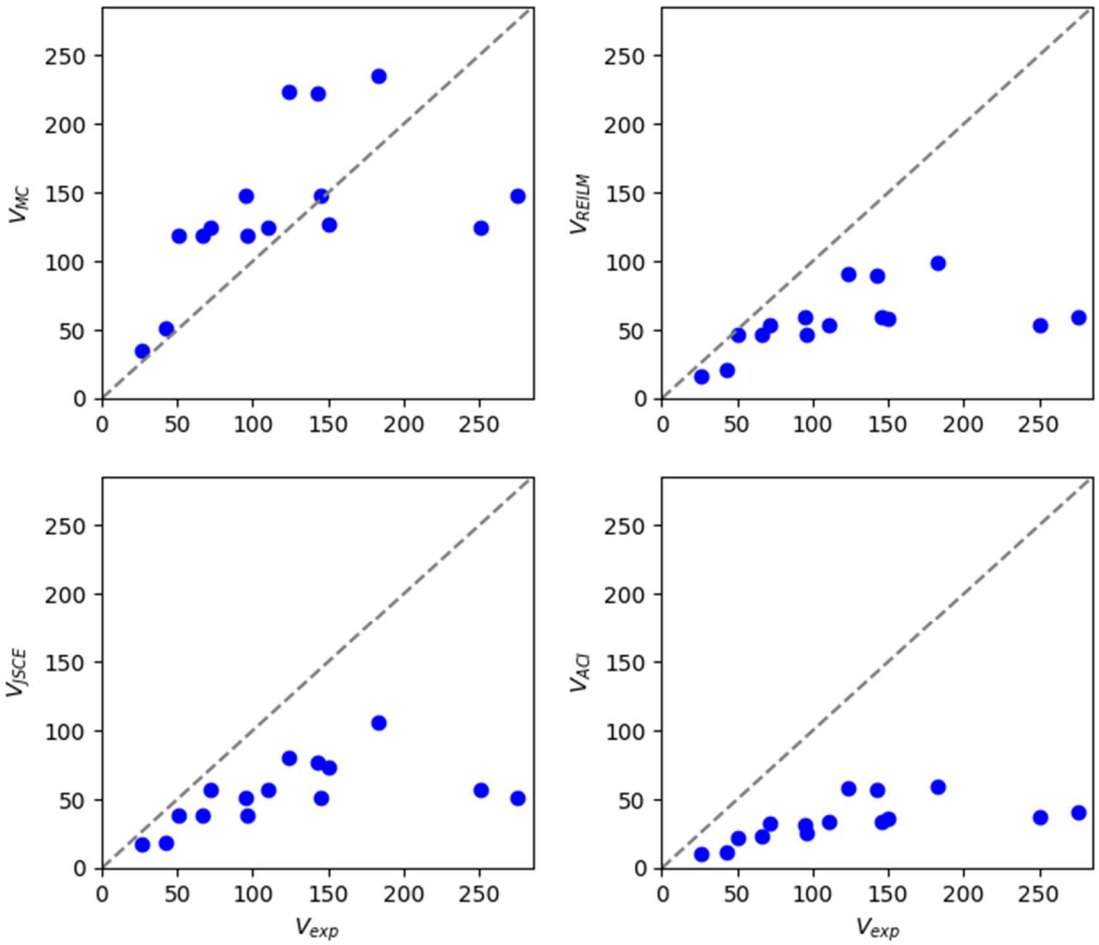

Figure 7.13: Performance of four different codes against the PVA database

The excessive dispersion between analysis and experiment in the case of all models underlines the status of the state of the art regarding the ability to assess the shear strength contributions of SHFRCC. The discrepancy increases with higher specimen forces which correspond generally to larger size members. A much more thorough investigation is called for to develop a new interpretation that organizes the data in a more convincing manner before a design expression is adopted in Engineering Practice. While this issue remains unresolved, however, practical use of the emerging SHFRCC materials is seriously impaired by lack of dependable models to conduct the calculations.

CHAPTER 8: CONCLUSIONS

In the present thesis a consistent interpretation of the mechanics of shear failure in reinforced concrete members with no shear reinforcement is pursued. The question explored is whether many of the so-called shear failures in specimens included in the databases used for calibration of the code equations are actually shear or bond failures that occur due to strain penetration from the last flexural crack of the beam and towards the anchorage of longitudinal reinforcement. The advantage of this interpretation, apart from it being consistent with the first principles when applied to the shear span of a beam, is that it addresses the question of size effect on shear, as it is related to the scaling of bar sizes when going from a small-scale specimen to a large one keeping constant the area ratio of longitudinal reinforcement.

This model is used as the basis for interpretation of the enhanced shear strength of beams comprising SHFRCC materials. To study the mechanics of shear in this type of structural members without stirrups, an experimental program was undertaken with emphasis on a green sustainable PVA Strain Hardening Cementitious Composite as a new generation of cement-based materials. The material was made in-house using local ingredients – fabrication was a result of an extensive preliminary investigation into the ideal mix design which would yield optimal ductility in the response. Through this effort it was shown that the combination of high volume fly ash (HVFA) and short discontinued synthetic polyvinyl-alcohol (PVA) fibers results in an innovative cementitious composite that will outperform normal concrete in many aspects such as ductility in tension, compression, shear and flexure. In addition to the environmentally beneficial aspect of the use of waste materials such as fly ash, silica fume and slag in the developed cementitious composite, a more compact composite in microstructure level is produced which is an ideal characteristic for improved durability of structures.

The aim of the experimental component of the thesis was to study the structural performance of SHFRCC, with particular interest in its behavior and failure under shear, either combined with flexural action or not. A longer-term interest is to combine information regarding the bond behavior of reinforcement embedded in this type of material in order to evaluate the shear strength of members made of SHFRCC. The

underlying concepts refer to the development capacity of the reinforcement, consistently with the Engineering Beam Theory and the developments in the first part of the study regarding interaction of bond with strain penetration.

In the preliminary experimental study several different materials were examined to experimentally achieve a true Strain Hardening Fiber Reinforced Cementitious Composite (SHFRCC) in the structural laboratory of Lassonde School of Engineering at York University. The performance of different developed batches was examined through compression and flexural testing of small scale specimens.

A large concrete casting (200 liter) was conducted in the main phase of the research to study the shear strength of SHFRCC and any possible size effect through testing of six different types of push-off specimens and to analyse the data so as to extract the Mohr-Coulomb failure envelope of this material. Moreover, four-point bending tests were performed on large-scale SHFRCC beams to study the behaviour of SHFRCC under combined shear and flexure. From the tests it was seen that all specimens have multiple cracking properties through pull out rather than fracturing behaviour of fibers at crack locations.

In the analytical part of this work, the primary objective was to understand the effective parameters in shear failure and to develop an alternative way of calculating one-way shear strength of concrete beams.

The work contained several different phases from which the following conclusions are drawn:

1. Actual state of bond of reinforcement along the shear span of a beam controls the failure in reinforced beams without stirrups. In the absence of confinement an anchorage can support a maximum bar strain at the critical section the magnitude of which is controlled by the characteristic fracture energy of the material. As a result of this limitation, once the strain demand exceeds this limiting value, the anchorage splits the cover precipitously and failure is controlled by this “unzipping mechanism”. Thus, if the anchorage length is not enough to provide the required bond force so as to equilibrate the force in the longitudinal reinforcements, strain

penetration over the unconfined length spreads further into the anchorage and may propagate over the entire length of available longitudinal reinforcement, perpetrating brittle failure and collapse at loads that are much lower than the nominal shear strength.

2. The addition of PVA fibers in a properly graded cementitious mix offers characteristic benefits in terms of internal confinement, tensile strain capacity and strain ductility, and control of crack widths.
3. Substantial structural member displacement ductility can be achieved by using PVA fibers even in the absence of stirrups.
4. A relatively small amount of fine, high quality silica sand is required to ensure strain hardening and multiple cracking.
5. Control of bond between PVA fiber and cementitious material through pertinent surfactants is feasible through coating of fibers however it needs special considerations that complicate significantly the process of batching the fresh mix.
6. Workability of PVA-SHFRCC is achievable with use of proper superplasticizer. However, the proper percentage and correct procedure to add the superplasticizer needs extra care.
7. PVA fibers may be used as a partial replacement of conventional transverse reinforcement.
8. Shear strength of PVA-SHFCC material is in order of 8-10MPa and proved to be higher than that of normal concrete (which is about $0.2\sqrt{fc}$, which for concrete with a comparable compressive strength as the SHFRCC (64MPa) gives a shear strength value of 1.6 MPa)
9. It seems there is no size effect involved in PVA-SHFRCC specimens. This is expected as an outcome of the large strain capacity of the material which enables redistribution of strain energy upon cracking initiation with no loss of strength.

Recommendations:

1. Continued work on development of SHFRCC is needed with focus on control of bond properties of PVA fibers and increased ductility of cementitious composites.
2. An extensive research program similar to this thesis is beneficial to further study the effect of the developed PVA-SHFRCC mix on hardened concrete specimens and to provide more experimental data for the PVA database.
3. A research on effect of cyclic loading on PVA-SHFRCC is required.
4. A Finite Element analysis of PVA-SHFRCC is required to further investigate the behaviour of this material and to reverse engineer the uniaxial tensile stress-strain properties.
5. Further expansion of “strain penetration in longitudinal bar anchorage” concept for one-way shear strength of SHFRCC beams is needed.
6. Improved design models for shear of SHFRCC that account explicitly for the bond stress interaction between the matrix and steel reinforcement are needed to obtain a consistent interpretation of the experimental evidence. Such developments are necessary in order to implement these materials in the construction or the precast industry.

BIBLIOGRAPHY

ACI Committee 318 (2014). Building code requirements for reinforced concrete.

ACI Committee 544 (2008). State-of-the-Art Report on Fiber Reinforced Concrete - ACI 544.1R-96 (Reapproved 2002). ACI Manual of Concrete Practice, Part 6, 2008, pp. ACI544.1R-7 – ACI544.1R-24.

Ahmed, S. F. U., & Mihashi, H. (2007). A review on durability properties of strain hardening fibre reinforced cementitious composites (SHFRCC). Cement and Concrete Composites, 29(5), 365-376.

Alyousif, A., Anil, O., Sahmaran, M., Lachemi, M., Yildirim, G., & Ashour, A. F. (2015). Comparison of shear behaviour of engineered cementitious composite and normal concrete beams with different shear span lengths. Magazine of Concrete Research, 68(5), 217-228.

Anon. (1914). An investigation of the pozzolanic nature of coal ashes. Engineering News, 71 (24), pp 1334-1335.

Arakawa, T., Ohno, K. (1957) Transactions of the Architectural Institute of Japan, 57, 581-584 (in Japanese).

Archontas, N., & Pantazopoulou, S. J. (2012). Microstructural aspects of the mechanical behavior of nanomodified cementitious materials. In CD-ROM proceedings, 4th international symposium of nanocomposites in construction (NICOM-4), Agios-Nicolaos, Crete Google Scholar.

ASTM C1609/C1609M (2010). Standard test methods for flexural performance of fiber-reinforced concrete (using beam with third-point loading).

ASTM C230/C230M (2014). Standard Specification for Flow Table for Use in Tests of Hydraulic Cement.

ASTM C1856/C1856M (2017). Fabricating and Testing Specimens of Ultra-High-Performance Concrete.

Balaguru, P. N., & Shah, S. P. (1992). Fiber-reinforced cement composites.

Bazant, Z. P., & Planas, J. (1997). Fracture and size effect in concrete and other quasibrittle materials (Vol. 16). CRC press.

Bažant, Z. P. (1999). Size effect on structural strength: a review. Archive of applied Mechanics, 69(9-10), 703-725.

Bažant, Z. P. (2002). Concrete fracture models: testing and practice. Engineering fracture mechanics, 69(2), 165-205.

Belarbi, A., Kuchma, D. A., & Sanders, D. H. (2017). Proposals for New One-Way Shear Equations for the 318 Building Code. Concrete International, 39(9), 29-32.

Bentz, E. C., & Collins, M. P. (1998). Response-2000: Reinforced Concrete Sectional Analysis using the Modified Compression Field Theory.

Bentz, D. P., Ferraris, C. F., & Snyder, K. A. (2013). Best practices guide for high-volume fly ash concretes: Assuring properties and performance (No. Technical Note (NIST TN)-1812).

Bentz, E. C., & Collins, M. P. (2017). Updating the ACI Shear Design Provisions. Concrete International, 39(9), 33-37.

Bresler, B., & Pister, K. S. (1958). Strength of concrete under combined stresses. In Journal Proceedings (Vol. 55, No. 9, pp. 321-345).

Canadian Standards Association (2006). Design of concrete structures. Mississauga, Ont.: Canadian Standards Association.

Cladera, A., & Marí, A. R. (2004). Shear design procedure for reinforced normal and high-strength concrete beams using artificial neural networks. Part I: beams without stirrups. Engineering Structures, 26(7), 917-926.

Cladera, A., Marí, A., Bairán, J. M., Oller, E., & Ribas, C. (2017). One-Way Shear Design Method Based on a Multi-Action Model. Concrete International, 39(9), 40-46.

Collins, M. P., Mitchell, D., Adebar, P., & Vecchio, F. J. (1996). A general shear design method. ACI Structural Journal, 93(1), 36-45.

Collins, M. P., & Kuchma, D. (1999). How safe are our large, lightly reinforced concrete beams, slabs, and footings? Structural Journal, 96(4), 482-490.

Daluga, D., McCain, K., Murray, M., & Pujol, S. (2017). Effect of Geometric Scaling on Shear Strength of Reinforced Concrete Beams with Stirrups. ACI Structural Journal, 114(6).

Darwin, D., & Pecknold, D. A. (1977). Nonlinear biaxial stress-strain law for concrete. Journal of the Engineering Mechanics Division, 103(2), 229-241.

Darwin, D., Barham, S., Kozul, R., & Luan, S. (2001). Fracture energy of high-strength concrete. American Concrete Institute.

De Normalisation, Comité Européen. Eurocode 2 (2004): Design of concrete structures. Brussels, Belgium.

Dinh, H. H., Parra-Montesinos, G. J., & Wight, J. K. (2010). Shear strength model for steel fiber reinforced concrete beams without stirrup reinforcement. Journal of Structural Engineering, 137(10), 1039-1051.

EN 1991-1-1 (2004). Eurocode 2: Design of concrete structures. CEN, European Committee for Standardization, Brussels, Belgium

Eshghi, N (2018), Different Types of Fibers in FRCC, Retrieved from https://mohandesbano.wordpress.com/

Eshghi, N. & Pantazopoulou, S., J., (2018). An alternative interpretation of one-way shear strength: strain penetration in longitudinal bar anchorage, In Proceedings of the CSCE Conference, Fredericton, New Brunswick, Canada, 13-16 June.

Feld, J., & Carper, K. L. (1997). Construction failure (Vol. 78). John Wiley & Sons.

Ferraris, C. F., Obla, K. H., & Hill, R. (2001). The influence of mineral admixtures on the rheology of cement paste and concrete. Cement and concrete research, 31(2), 245-255.

fib (Federation International du Beton) (2010). fib model code 2010, Paris.

fib Bulletin No. 72 (2014). Bond and anchorage of embedded reinforcement.

fib Bulletin No. 85 (2014). Towards a rational understanding of shear in beams and slabs

Foster, R. M., Morley, C. T., & Lees, J. M. (2015). Modified push-off testing of an inclined shear plane in reinforced concrete strengthened with CFRP fabric. Journal of Composites for Construction, 20(3), 04015061.

Foster, S. J., Agarwal, A. (2014). A Unified Approach for Shear Design of SFRC and UHPFRC Girders.

Frosch, R. J., Yu, Q., Cusatis, G., & Bažant, Z. P. (2017). A unified approach to shear design. Concrete International, 39(9), 47-52.

GeoPIV-RG (2015) University of Western Australia - Queens' University, Canada URL http://www.geopivrg.com/

Georgiou, A. V., (2017) Characterization of the structural performance of strain-hardening fiber reinforced cementitious composites.

Georgiou, A. V., Pantazopoulou, S., J. & Petrou, M. (2014). Increasing ductility of FRCC with proprietary coating agents. In 10th fib International PhD Symposium in Civil Engineering (pp. 25-30).

Georgiou, A. V., & Pantazopoulou, S. J. (2016). Use of Waste Fly Ash from Power Plants for Use in Cementitious Composites for Structural Elements. In Proceedings of the 4th International Conference on Sustainable Solid Waste Management, Limassol, Cyprus.

Georgiou, A. V., & Pantazopoulou, S. J. (2016). Effect of fiber length and surface characteristics on the mechanical properties of cementitious composites. Construction and Building Materials, 125, 1216-1228.

Georgiou, A. V., & Pantazopoulou, S. J. (2017). Behavior of Strain Hardening Cementitious Composites in Flexure/Shear. Journal of Materials in Civil Engineering, 29(10), 04017192.

Grégoire, D., Rojas-Solano, L. B., & Pijaudier-Cabot, G. (2013). Failure and size effect for notched and unnotched concrete beams. International Journal for Numerical and Analytical Methods in Geomechanics, 37(10), 1434-1452.

Hasse, R. (1989). Rainwater reservoirs above ground structures for roof catchment. Gate, Vieweg, Braunschweig/Wiesbaden, Germany, 102p.

Hofbeck, J. A., Ibrahim, I. O., & Mattock, A. H. (1969, February). Shear transfer in reinforced concrete. In Journal Proceedings (Vol. 66, No. 2, pp. 119-128).

Holland, T. C. (2005). Silica fume user's manual. Federal Highway Administration.

Hopkins, D. S., Thomas, M. D. A., Oates, D. B., Girn, G., & Munro, R. (2001). York University uses high-volume fly ash concrete for green building. In Annual conference of the canadian Society for Civil Engineering, CSCE.

Hou, L. J., Luan, Z. Y., Chen, D., & Xu, S. L. (2015). Experimental study of the shear properties of reinforced ultra-high toughness cementitious composite beams. Journal of Zhejiang University-SCIENCE A, 16(4), 251-264.

Islam, M. S., Pam, H. J., & Kwan, A. K. H. (1998). Shear capacity of high-strength concrete beams with their point of inflection within the shear span. Proceedings of the Institution of Civil Engineers: Structures and Buildings.

Japan Society of Civil Engineers: Standard specifications for concrete structures: Materials and Construction. (2005).

Jiménez-Quero, V. G., León-Martínez, F. M., Montes-Garcia, P., Gaona-Tiburcio, C., & Chacón-Nava, J. G. (2013). Influence of sugar-cane bagasse ash and fly ash on the rheological behavior of cement pastes and mortars. Construction and Building Materials, 40, 691-701.

Kang, S. B., Tan, K. H., Zhou, X. H., & Yang, B. (2017). Experimental investigation on shear strength of engineered cementitious composites. Engineering Structures, 143, 141-151.

Kani, G. N. J. (1964). The riddle of shear failure and its solution. In Journal Proceedings (Vol. 61, No. 4, pp. 441-468).

Kani, G. (1967, March). How safe are our large reinforced concrete beams?. In Journal Proceedings (Vol. 64, No. 3, pp. 128-141).

Karihaloo, B. L., Abdalla, H. M., & Xiao, Q. Z. (2003). Size effect in concrete beams. Engineering fracture mechanics, 70(7-8), 979-993.

Kasparkiewicsz, J., (1978) Discussion, in Proceedings of RILEM Symposium on Testing and Test Methods of Fiber Cement Composites, Edited by N. Swamy, The Construction Press, England, pp. 493–495.

Kirane, K., Singh, K. D., & Bažant, Z. P. (2016). Size Effect in Torsional Strength of Plain and Reinforced Concrete. ACI Structural Journal, 113(6).

Kupfer, H. (1964). Expansion of Morsch's truss analogy by application of the principle of minimum strain energy. CEB bulletin, 40.

Lawler, J. S., Zampini, D., & Shah, S. P. (2005). Microfiber and macrofiber hybrid fiber-reinforced concrete. Journal of Materials in Civil Engineering, 17(5), 595-604.

Leonhardt, F. (1964). On the reduction of shear reinforcement as derived from the Stuttgart shear tests 1961-1963. In IABSE congress report (Vol. 7).

Lepech, M. D., & Li, V. C. (2006). Long Term Durability Performance of Engineered Cementitious Composites/Langzeitbeständigkeit Systematisch Entwickelter Zusammengesetzter Zement Gebundener Werkstoffe. Restoration of Buildings and Monuments, 12(2), 119-132.

Lepech, M. D., & Li, V. C. (2008). Large-scale processing of engineered cementitious composites. ACI Materials Journal, 105(4), 358.

Lepech, M. D., & Li, V. C. (2009). Water permeability of engineered cementitious composites. Cement and Concrete Composites, 31(10), 744-753.

Li, V. C., & Kanda, T. (1998). Innovations forum: engineered cementitious composites for structural applications. Journal of Materials in Civil Engineering, 10(2), 66-69.

Li, V. C., Kong, H. J., & Chan, Y. W. (1998). Development of self-compacting engineered cementitious composites.

Li, V. C. (2002). Advances in ECC research. ACI Special Publications, 206, 373-400.

Li, V. C. (2002). Reflections on the research and development of engineered cementitious composites (ECC).

Li, V. C., Wu, C., Wang, S., Ogawa, A., & Saito, T. (2002). Interface tailoring for strain-hardening polyvinyl alcohol-engineered cementitious composite (PVA-ECC). Materials Journal, 99(5), 463-472.

Li, V. C. (2003). On engineered cementitious composites (ECC). Journal of advanced concrete technology, 1(3), 215-230.

Li, Y. A., Hsu, T. T., & Hwang, S. J. (2017). Shear Strength of Prestressed and Nonprestressed Concrete Beams. Concrete International, 39(9), 53-57.

MacGregor, J. G., Wight, J. K., Teng, S., & Irawan, P. (1997). Reinforced concrete: Mechanics and design (Vol. 3). Upper Saddle River, NJ: Prentice Hall.

Majdzadeh, F., Soleimani, S. M., & Banthia, N. (2006). Shear strength of reinforced concrete beams with a fiber concrete matrix. Canadian Journal of Civil Engineering, 33(6), 726-734.

Manz, O.E. 1993. "Worldwide production of coal ash and utilization in concrete and other products." In Proceedings of the 10th International Ash Use Symposium, EPRI TR-101774, Vol. 2, Electric Power Research Institute, pp 64/1-12.

Manz, O. E. (1997). Worldwide production of coal ash and utilization in concrete and other products. Fuel, 76(8), 691-696.

Megalooikonomou, K. G., Tastani, S. P., & Pantazopoulou, S. J. (2018). Effect of yield penetration on column plastic hinge length. Engineering Structures, 156, 161-174.

Miyazato, S., Hiraishi, Y., Zakharov, A., & Gizzatullin, R. 4484-TRANSPORT PROPERTIES AND STEEL CORROSION IN DUCTILE FIBER REINFORCED CEMENT COMPOSITES. In ICF11, Italy 2005.

Mondo, E. (2011). Shear Capacity of Steel Fibre Reinforced Concrete Beams without Conventional Shear Reinforcement.

Mörsch E. Concrete-steel construction. New York: McGraw-Hill Book Company; 1909. 368pp.

Mörsch, E. (1902). Der eisenbetonbau, seine anwendung und theorie. Wayss and Freytag, AG, Im Selbstverlag der Firma, Neustadt ad Haardt.

Mörsch, E., & Goodrich, E. P. (1910). Concrete-steel Construction:(Der Eisenbetonbau). Engineering News Publishing Company.

Naaman, A. E. (1972). A statistical theory of strength for fiber reinforced concrete (Doctoral dissertation, Massachusetts Institute of Technology).

Naaman, A. E., & Reinhardt, H. W. (2003). High performance fiber reinforced cement composites HPFRCC-4: International RILEM Workshop. Materials and Structures, 36(10), 710-712.

Naaman, A. E., & Reinhardt, H. W. (2006). Proposed classification of HPFRC composites based on their tensile response. Materials and structures, 39(5), 547-555.

Naaman, A. E. (2007). Tensile strain-hardening FRC composites: Historical evolution since the 1960. In Advances in construction materials 2007 (pp. 181-202). Springer, Berlin, Heidelberg.

Naaman, A. E. (2018). FIBER REINFORCED CONCRETE: FIVE DECADES OF PROGRESS. Composite Materials. Rio de Janeiro.

Ozbolt, J., & Eligehausen, R. (2002). 20 SIZE EFFECT IN CONCRETE AND REINFORCED CONCRETE STRUCTURES. Size-Scale Effects in the Failure Mechanisms of Materials and Structures, 290.

Paegle, I., & Fischer, G. (2012). Shear crack formation and propagation in fiber reinforced cementitious composites (FRCC). In High Performance Fiber Reinforced Cement Composites 6 (pp. 231-238). Springer, Dordrecht.

Paegle, I., & Fischer, G. (2016). Phenomenological interpretation of the shear behavior of reinforced engineered cementitious composite beams. Cement and Concrete Composites, 73, 213-225.

Pal, S. C., Mukherjee, A., & Pathak, S. R. (2003). Investigation of hydraulic activity of ground granulated blast furnace slag in concrete. Cement and Concrete Research, 33(9), 1481-1486.

Park, H. G., & Choi, K. K. (2017). Unified Shear Design Method of Concrete Beams Based on Compression Zone Failure Mechanism. Concrete International, 39(9), 59-63.

Peled, A., & Shah, S. P. (2003). Processing effects in cementitious composites: extrusion and casting. Journal of Materials in Civil Engineering, 15(2), 192-199.

Quach, P. T. (2016). Understanding and safely predicting the shear response of large-scale reinforced concrete structures (Doctoral dissertation, University of Toronto (Canada)).

R Core Team (2015). A language and environment for statistical computing. R Foundation for Statistical Computing, Vienna, Austria, URL http://www.R-project.org/.

Redon, C., Li, V. C., Wu, C., Hoshiro, H., Saito, T., & Ogawa, A. (2001). Measuring and modifying interface properties of PVA fibers in ECC matrix. Journal of Materials in Civil Engineering, 13(6), 399-406.

Reineck, K. H. (1990). Ein mechanisches Modell für den Querkraftbereich von Stahlbetonbauteilen (Mechanical model for the behaviour of reinforced concrete members in shear). PhD thesis, University of Stuttgart, 1-273.

Reineck, K. H. (1991). Ultimate shear force of structural concrete members without transverse reinforcement derived from a mechanical model (SP-885). Structural Journal, 88(5), 592-602.

Reineck, K. H., Kuchma, D. A., Kim, K. S., & Marx, S. (2003). Shear database for reinforced concrete members without shear reinforcement. Structural Journal, 100(2), 240-249.

Reineck, K. H. (2017). Proposal for ACI 318 Shear Design. Concrete International, 39(9), 65-70.

Ritter, W. (1899). The Hennebique construction method. Die Bauweise Hennebique"), Schweizerische Bauzeitung, 33(7), 41-61.

RILEM TC 162-TDF (2003). Test and design methods for steel fibre reinforced concrete." Materials and structures 36, pp. 560-567.

Romualdi, J.P & Batson, G.B. (1963): Mechanics of Crack Arrest in Concrete. Journal of the Engineering Mechanics Division, 1963, Vol. 89, Issue 3, Pg. 147-168.

Romualdi, J. P., & Mandel, J. A. (1964, June). Tensile strength of concrete affected by uniformly distributed and closely spaced short lengths of wire reinforcement. In Journal Proceedings (Vol. 61, No. 6, pp. 657-672).

SAP2000, CSI (2017) SAP2000 Integrated Software for Structural Analysis and Design, Computers and Structures Inc., Berkeley, California.

Shimizu, K., Kanakubo, T., Kanda, T., & Nagai, S. (2004, August). Shear behavior of steel reinforced PVA-ECC beams. In 13th World Conference on Earthquake Engineering, Conference Proceedings DVD, Paper (No. 704, p. 8).

Song, G., & Van Zijl, G. P. A. G. (2004, September). Tailoring ECC for commercial application. In Proceedings of the 6th RILEM symposium on fiber-reinforced concretes (FRC)—BEFIB (pp. 20-22).

Tastani, S. P., & Pantazopoulou, S. J. (2007). Behavior of corroded bar anchorages. ACI Structural Journal, 104(6), 756.

Tastani, S. P., & Pantazopoulou, S. J. (2013a). Reinforcement and concrete bond: state determination along the development length. Journal of Structural Engineering, 139(9), 1567-1581.

Tastani, S. P., & Pantazopoulou, S. J. (2013b). Yield penetration in seismically loaded anchorages: Effects on member deformation capacity. Earthq. Struct, 5(5), 527-552.

Taylor, H. P. (1972). Shear strength of large beams. Journal of the Structural Division, 98 (Proc Paper 9329).

Thomas, M. D. A. (2007). Optimizing the use of fly ash in concrete (Vol. 5420). Skokie, IL: Portland Cement Association.

Thürliman, B., Bachmann, H., Kraus, R., Caflisch, R., Hemgartned, E. (1978) shear tests on partially prestressed beams. Institut fur bautechnik ETH Zurich, Report Nr.6504-2, 6504-3, 6504-5, 6504-6.

Van Zijl, G. P., Wittmann, F. H., Oh, B. H., Kabele, P., Toledo Filho, R. D., Fairbairn, E. M., ... & Altmann, F. (2012). Durability of strain-hardening cement-based composites (SHCC). Materials and structures, 45(10), 1447-1463.

Vecchio, F. J., & Collins, M. P. (1986). The modified compression-field theory for reinforced concrete elements subjected to shear. ACI J., 83(2), 219-231.

VecTor2 (2017) Finite Element Analysis of Reinforced Concrete- F.J. Vecchio- University of Toronto, URL http://vectoranalysisgroup.com/

Walraven, J. C., & Reinhardt, H. W. (1981). Concrete mechanics. Part A: Theory and experiments on the mechanical behavior of cracks in plain and reinforced concrete subjected to shear loading. NASA STI/Recon Technical Report N, 82.

Walraven, J., Mercks, P. (1983), The bearing capacity of prestressed hollow core slabs, Heron, Vol. 28, No. 3

Wang, S., & Li, V. C. (2006). Polyvinyl alcohol fiber reinforced engineered cementitious composites: material design and performances. In RILEM PRO (Vol. 49).

Xu, Shilang, and Hans W Reinhardt. (2005). “Shear Fracture on the Basis of Fracture Mechanics.” Otto-Graf-Journal 16: 21–78.

Yazdanbakhsh, A., Altoubat, S., & Rieder, K. A. (2015). Analytical study on shear strength of macro synthetic fiber reinforced concrete beams. Engineering Structures, 100, 622-632.

Yun, H. D., & Rokugo, K. (2012). Freeze-thaw influence on the flexural properties of ductile fiber-reinforced cementitious composites (DFRCCs) for durable infrastructures. Cold Regions Science and Technology, 78, 82-88.

APPENDICES

APPENDIX A: R CODES

```
 #M-epsilon Curve
M_epsilon <- function(epsilon){
if (epsilon <= NUMBER1)
{M_epsilon <- EQ1}
 else
{M_epsilon<- EQ2}
   return(M_epsilon) }
##########################################################################
 # Seeking Second Crack
   epsilon <- FIRST GUESS
   eps_elas <- M_epsilon(epsilon)*ys_na/(Ec*I)
   eq2 <- function(p, w, ys_na, Ec, I, Ls, b, h, epsilon, range=c(0, Ls), step = .01,tol =
10^(-9)){
     eps_elas <- M_epsilon(epsilon)*10^6*ys_na/(Ec*I)
     s <- numeric()
     xx <- numeric()
     x <- range[1]
     summation <- 1
     j <- 0
     while(x >= range[1] & x<=range[2]){
       x <- x + step
       C1 <- .5*exp(w*x)*(eps_elas*(1+1/(w*Ls)-x/Ls))
       C2 <- .5*exp(-w*x)*(eps_elas*(1-1/(w*Ls)-x/Ls))
       summation <- C1+C2-epsilon
       s <- c(s, summation)
       xx <- c(xx, x)
       j <- j+1
```

```
    }return(list(C1=C1, C2=C2, iters=j-1, process=cbind(xx,s), summation=min(abs(s)), Ld=xx[which(abs(s)==min(abs(s)))]))}
  sol <- eq2(p, w, ys_na, Ec, I, Ls,b, h, epsilon, range=c(0, Ls), step = .01, tol = 10^(-9))#, max_inter=100000)
  Ld1 <- sol$Ld
##########################################################################
#Seeking the 2nd crack X place
#1
# Posibility one: Inside Ld
x <- seq(0,Ld1,by = Ld1/50)
eps_elas <- M_epsilon(epsilon)*10^6*ys_na/(Ec*I)
C1 <- .5*exp(w*Ld1)*(eps_elas*(1+1/(w*Ls)-Ld1/Ls))#-N/(Ec*b*h))
C2 <- .5*exp(-w*Ld1)*(eps_elas*(1-1/(w*Ls)-Ld1/Ls))#-N/(Ec*b*h))
epsilon_x <- C1* exp(-w*x)+ C2* exp (w*x)
Crack <- ifelse(Es * As * (epsilon - epsilon_x) > fct * Aeff, "crack", "no crack")
x[which(Crack=="crack")]
##########################################################################
#Otherwise -> Posibility two: outside Ld
e_cr_reinf <- e_cr*ys_na/(0.5*h)
eps_elas <- M_epsilon(epsilon)*10^6*ys_na/(Ec*I)
x_cr2 <- (1-e_cr_reinf/eps_elas)*Ls1
x_cr2
##########################################################################
#flexural theory
x_ <- seq(Ld1,Ls, by = (Ls-Ld1)/10)
epsilon_x_ <- eps_elas * (1-x_/Ls)
##########################################################################
#Slip
#if x<ld1
c <- (C2 * exp(w*Ld1)-C1 * exp(-w*Ld1))/w
```

```
slip <- (C1 * exp(-w*x)-C2 * exp(w*x))/w + c
#############################################################################
#To find third crack
epsilon2 <- SECOND GUESS
M0 <-  M_epsilon(epsilon2)
Mcr_2 <- M0 * (1-x_cr2/Ls1)
eps_elas <- M0*10^6*ys_na/(Ec*I)
epsilon_Mcr_x2 <- function(Mcr_2){
if (Mcr_2 <= 3.154)
{epsilon_Mcr_x2 <- (Mcr_2 +4*10^-16)/73349}
  else
{epsilon_Mcr_x2 <- (Mcr_2 -3.4078)/21301}
return(epsilon_Mcr_x2)}
epsilon_Mcr_x2 <- epsilon_Mcr_x2 (Mcr_2)
#############################################################################
#Disturbed region
eq3 <- function(p, w, ys_na, Ec, I, Ls, b, h, epsilon,epsilon_Mcr_x2, x_cr2, range, step,
tol){
eps_elas <- M0*10^6*ys_na/(Ec*I)
s <- numeric()
xx <- numeric()
x <- range[1]
summation <- 1
 j <- 0
 while(x >= range[1] & x<=range[2]){
 x <- x + step
C1 <- .5*exp(w*x)*(eps_elas*(1+1/(w*Ls)-(x+x_cr2)/Ls))#-N/(Ec*b*h))
C2 <- .5*exp(-w*x)*(eps_elas*(1-1/(w*Ls)-(x+x_cr2)/Ls))#-N/(Ec*b*h))
 summation <- C1+C2-epsilon_Mcr_x2
 s <- c(s, summation)
```

```
xx <- c(xx, x)
   j <- j+1 }
 return(list(C1=C1, C2=C2, iters=j-1, summation=min(abs(s)), Ld=xx[which(abs(s)==min(abs(s)))]))}
sol <- eq3(p, w, ys_na, Ec, I, Ls,b, h, epsilon2,epsilon_Mcr_x2, x_cr2, range=c(x_cr2, Ls), step = .01, tol = 10^(-9))#, max_inter=100000)
Ld2 <- sol$Ld
#############################################################################
#Investigating the part one (from 0 to xcr_2)
x1 <- seq(0,x_cr2,by = x_cr2/10)
C_prim1 <- (epsilon_Mcr_x2-epsilon2*exp(w*x_cr2))/(exp(-w*x_cr2)-exp(w*x_cr2))
C_prim2 <- (-epsilon_Mcr_x2+epsilon2*exp(-w*x_cr2))/(exp(-w*x_cr2)-exp(w*x_cr2))
epsilon_x_part1 <- C_prim1* exp(-w*x1)+ C_prim2* exp (w*x1)
slip_part1 <- (C_prim1 * exp(-w*x)-C_prim2 * exp(w*x))/w
#############################################################################
##Investigating the part two (from xcr_2 to Ls)
#if x_cr2+Ld2 >Ls then we should go for Anchorage solution
#Anchorage solution- Part two Whole length
epsilon3 <- epsilon_Mcr_x2
Lb <-Ls-x_cr2
x2 <- seq(x_cr2,Ls,by = Lb/50)
epsilon_x_Anchorage <- (epsilon3/(1-exp(-2*w*Lb)))*(exp(-w*(x2-x_cr2))-exp(w*(x2-x_cr2)-2*w*Lb))
slip_Anchorage<- epsilon3*(exp(-w*(x2-x_cr2))+exp(w*(x2-x_cr2)-2*w*Lb))/(w*(1-exp(-2*w*Lb)))
#############################################################################
#Part one slip:
#Slip from zero to x_cr2
x <- x_cr2
slip1<- epsilon3*(exp(-w*(x-x_cr2))+exp(w*(x-x_cr2)-2*w*Lb))/(w*(1-exp(-2*w*Lb)))
x <- Ls
```

```
slip2<- epsilon3*(exp(-w*(x-x_cr2))+exp(w*(x-x_cr2)-2*w*Lb))/(w*(1-exp(-2*w*Lb)))
slip3 <- (C_prim1 * exp(-w*x_cr2) - C_prim2 * exp(w*x_cr2))
C_prim <- (slip1 - slip2) - slip3
S1 <- (C_prim1 * exp(-w*x1) - C_prim2 * exp(w*x1)) /w + C_prim
##############################################################################
#Anchorage solution- Whole length (0 to Ls)
epsilon_el_i <- s1*w*(1-exp(-2*w*Ls))/(1+exp(-2*w*Ls)) #end of elastic region
epsilon4 <- THIRD GUESS
Lb <-Ls
x <- seq(0,Lb,by = Lb/50)
epsilon_x_bond <- (epsilon4/(1-exp(-2*w*Lb)))*(exp(-w*(x))-exp(w*(x)-2*w*Lb))
slip<- epsilon4*(exp(-w*(x))+exp(w*(x)-2*w*Lb))/(w*(1-exp(-2*w*Lb)))
plot(x,epsilon_x_bond, type = "l")
lines(c(x_cr2,  x_cr2), c(0,epsilon4 ),lty = "dashed", col="red")
lines(c(0,  Ls), c(epsilon_secondcrack,epsilon_secondcrack ),lty = "dashed", col="blue")
    # x_secondcrack_anchorage<-x_cr2
    # epsilon_secondcrack_anchorage <- (epsilon4/(1-exp(-2*w*Lb)))*(exp(-
w*(x_secondcrack_anchorage))-exp(w*(x_secondcrack_anchorage)-2*w*Lb))
##############################################################################
#Bond Plastification
# Lp <- Ls - (1/(2*w)) * Log((s1*w+epslion_el_ii)/(s1*w-epslion_el_ii))
##############################################################################
#Calculating Lp
epsilon5 <- FORTH GUESS
fn_lp <- function(x){
 epsilon5
 fb_max
  Es
  Db
  Ls
```

```
 w
 s1
 return(s1 - (((-4*fb_max * x)/(Es*Db)+epsilon5)*(1+exp(-2*w*(Ls-x)))/(w*(1-exp(-2*w*(Ls-x))))))
 }
initial_lp = GUESS
lp <- nleqslv(initial_lp, fn=fn_lp)$x
#After Calculation of Lp
epslion_el_ii <- epsilon5 - 4* fb_max * lp/(Es*Db)
#Platu Part of the Curve 0<x<Lp
x_platu <- seq(0,lp,by = lp/10)
epsilon_x <- epsilon5 - 4 * fb_max * x_platu/(Es*Db)
#slip <- s1 + 0.5 * (lp-x)(epsilon_x + epslion_el_ii)
constant <- s1 - (2*fb_max*lp^2/(Db*Es)) + epsilon5 * lp
slip_platu <- (2*fb_max*x_platu^2/(Db*Es)) - epsilon5 * x_platu + constant
##############################################################################
#Elastic Part of the curve lp<x<Lb
x_Elastic <- seq(lp,Ls,by = (Ls-lp)/50)
epsilon_elastic <- epslion_el_ii * (exp(-w*(x_Elastic-lp))-exp(w*(x_Elastic-lp)-2*w*(Lb-lp))) / (1-exp(-2*w*(Lb-lp)))
Slip_elastic <- epslion_el_ii * (exp(-w*(x_Elastic-lp))+exp(w*(x_Elastic-lp)-2*w*(Lb-lp))) / (w*(1-exp(-2*w*(Lb-lp))))
```

APPENDIX B: TEST RESULTS

B.1: Mix design of different batches casted in the preliminary phase of the experimental program

Series Name	Date	Fiber (gr)	Defoamer (gr)	Cement		Sand		Fly Ash (Kg)	Slag (gr)	Silica Fume (gr)	W/C	SP (gr)
				Type	Weigh (Kg)	Type	Weigh (Kg)					
B1	June 5th	-	-	GU	2	1	1	-	-	-	0.4	-
B2	June 6th	-	-	GU	1.4	50/50 - 1 & 3	1.4	1.2	-	-	0.38	-
B3	June 6th	26	-	GU	1.4	50/50 - 1 & 3	1.4	1.2	-	-	0.38	-
B4	June 8th	26	-	GU	1.3	4	1.02	1.6	-	-	0.26	20
B5	June 8th	26	-	GU	1.3	4	1.02	1.6	-	-	0.26	20*
B6	June 12th	78	-	GU	3.9	4	3.06	4.8	-	-	0.26	50.4
B7	June 14th	13	-	GU	0.65	70/30 - 4 & 2	0.51	0.8	-	-	0.27	8.4

B8	June 15th	13	-	GU	0.65	50/50 - 4 & 2	0.51	0.8	-	-	0.26	8.4**
B9	June 15th	13	-	GU	0.65	50/50 - 4 & 2	0.51	0.8	-	-	0.27	8.4**
B10	June 15th	13	-	GU	0.65	70/30 - 4 & 2	0.51	0.8	-	-	0.26	8.4
B11	June 19th	13	-	GU	0.65	50/50 - 4 & 2	0.51	0.8	-	-	0.27	8.4
B12	June 23rd	13	-	GUL	0.572	70/30 – 4 & 2	0.51	0.8	26	52	0.26	8.4
B13	June 26th	13	-	GUL	0.572	70/30 – 4 & 5	0.51	0.8	26	52	0.27	8.4
B14	June 28th	13	-	GUL	0.572	70/30 - 4 & 6	0.51	0.8	26	52	0.27	8.4

B15	July 4th	13	-	GUL	0.65	4	0.51	0.704	32	64	0.3	10
B16	July 4th	13	-	GUL	0.65	4	0.51	0.704	32	64	0.27	14.4
B17	July 7th	13	-	GUL	0.65	4	0.51	0.576	64	160	0.28	16.4
B18	July 7th	13	-	GUL	1.044	4	0.51	-	116	290	0.3	26.4
B19	July 12th	13	-	GUL	0.572	4	0.51	0.8	26	52	0.28	10
B20	July 28th	25	-	GUL	1.3	4	1.04	1.123	125	312	0.25	26
B21	Aug. 9th	13	-	GUL	0.65	50/50 - 3 &4	0.51	0.576	64	160	0.26	20
B22	Aug. 9th	13	-	GUL	0.65	50/50 - 3 &4	0.51	0.464	96	240	0.26	25
B23	Oct. 17th	Coat 27.95	-	GUL	0.468	4	0.52	0.78	52	130	0.28	28
B24	Jan. 8th	27.95	1.2	GUL	0.468	4	0.52	0.78	52	130	0.25	68
B25	Jan. 10th	28	-	GUL		4						

B26	Jan. 12th	3.25	0.15	GUL	0.050	4	0.0555	0.08334	5.6	14	0.25	1
B27	Jan. 17th	22.75	10	GUL	0.350	4	0.389	0.583	39.2	98	0.25	18
B28	Jan. 26th	22.75	-	GUL	0.350	7	0.389	0.583	39.2	98	0.25	18
B29	Jan. 26th	22.75	-	GUL	0.350	7	0.389	0.583	39.2	98	0.25	5.85
B30	Jan. 26th	22.75	-	GUL	0.350	4	0.389	0.583	39.2	98	0.25	18
B31	Jan. 26th	22.75	-	GUL	0.350	4	0.389	0.583	39.2	98	0.25	5.85
B32	Jan. 29th	22.75	-	GUL	0.350	7	0.389	0.583	39.2	98	0.25	11.7*
B33	Jan. 29th	22.75	-	GUL	0.350	7	0.389	0.583	39.2	98	0.25	5.85*
B34	Feb. 12th	22.75	-	GUL	0.350	7	0.389	0.583	39.2	98	0.25	8.7
B35	Feb. 12th	22.75	-	GUL	0.487	7	0.389	0.583	-	-	0.25	8.7
B36	Feb. 23rd	22.75	2.26	GUL	0.350	7	0.389	0.583	39.2	98	0.25	8.3

B37	Mar. 2nd	22.75	4.67	GUL	0.350	7	0.389	0.583	39.2	98	0.25	8.3
B38	Mar. 5th	22.75	4.67	GUL	0.350	8	0.389	0.583	39.2	98	0.25	8.3
B39	Mar. 5th	22.75	-	GUL	0.350	8	0.389	0.583	39.2	98	0.25	8.3

B.2: Age of specimens and results of compression and flexural tests in the Preliminary phase

Mix number	Age	f'_c (MPa)	F_{max}(KN)
B1	9 66	C37.1 -	- T3.25
B2	28 65	C43.43 -	- T2.7
B3	28 65	C42.11	- T2.3
B4	28 64	C50.03	- T2.82
B5	28 64	C61.59	- T2.79
B6	28 64 233	C59.1	- T4.07 5.52
B7	N/A		Bleeding
B8	28 No SCC	61.23	No Prism
B9	28	58.77	No Prism
B10	28 230	55.55	 4.07
B11	28 226	66.94	 4.65
B12	28 222	62.22	 3.96
B13	28	61.28	-

	46		T2.53
B14	28 217	54.67	4.53
B15	28 211	48.46	5.75
B16	28 211	64.56	4.41
B17	28 208	65.78	5.89
B18	28 208	79.42	5.17
B19	28 203	60	4.27
B20	28 187	73.8	No Prism
B21	28 175	81.47	3.2
B22	28 175	84.13	4.51
B23	127	40	2.13
B24	Jan8		Lightweigh
B25	Jan1 0		No Prism
B26	40	55	No Prism
B27	35 37	72.61	4.45

B28	3		3.33
B29	28		5.96
B30	5		No Prism
B31	Jan26		Not flowable
B32	28 28	70.68	4.42
B33	- 28	-	4.98
B34	28 28	64.5	4.96
B35	28 28	65.31	3.87
B36	28 28	40	3.76
B37	28 28	56.46	5.99
B38	28 28	58.24	4.65
B39	28 28	70.95	5.63

B.3: Failure crack of small-scale prisms (280*50*50 mm)

B6 (June 12th); B10 (June 15th); B11 (June 19th)

B12 (June 23rd); B14 (June 28th); B15 (July 4th)

B16 (July 4th); B17 (July 7th); B18 (July 7th)

B19 (July 12th); B21 (Aug. 9th); B22 (Aug. 9th)

B23 (Oct. 17th); B27 (Jan. 17th); B28 (Jan. 26th)

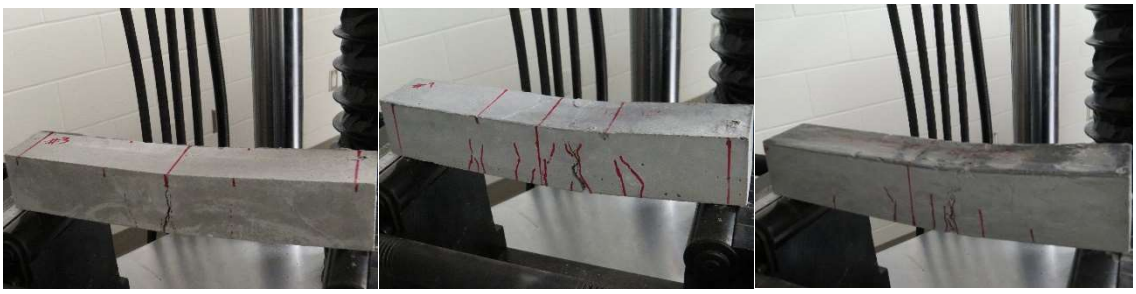

B29 (Jan. 26th); B30 (Jan. 26th), B32 (Jan. 29th)

B33 (Jan. 29th); B34 (Feb. 12th); B35 (Feb. 12th)

B36 (Feb. 23rd); B37 (Mar. 2nd), B38 (Mar. 5th)

B39 (Mar. 5th)

B.4: Load-actuator displacement of flexural prisms

B4.1: Three-point Bending Tests

B1- Aug 10th- 3PB; B3-Aug 10th-3PB

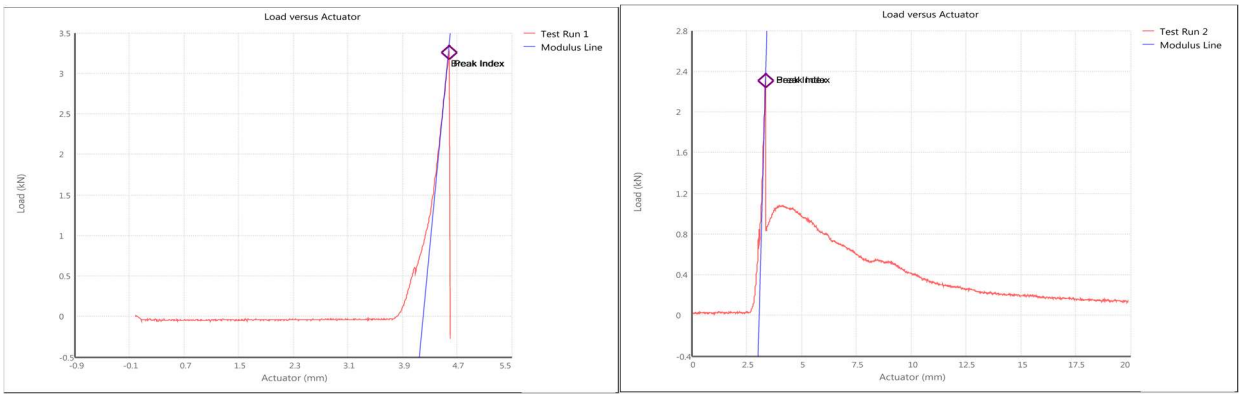

B2, B4, B5, B6, B13-Aug 11th-3PB

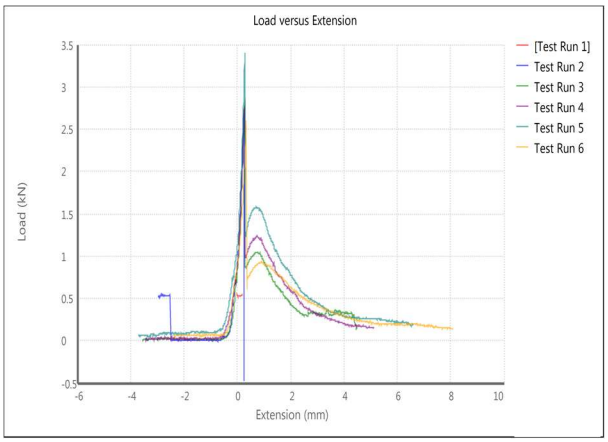

A4.2: Four-Point Bending Tests

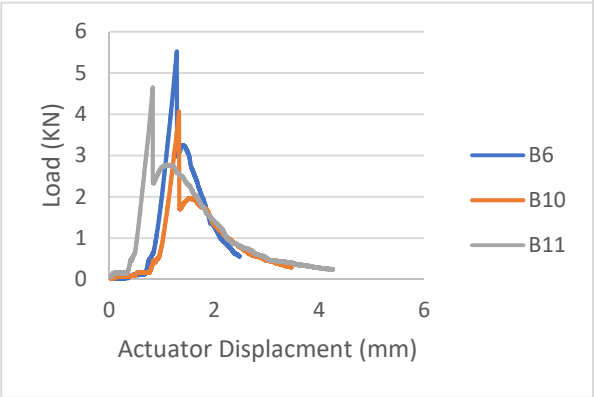

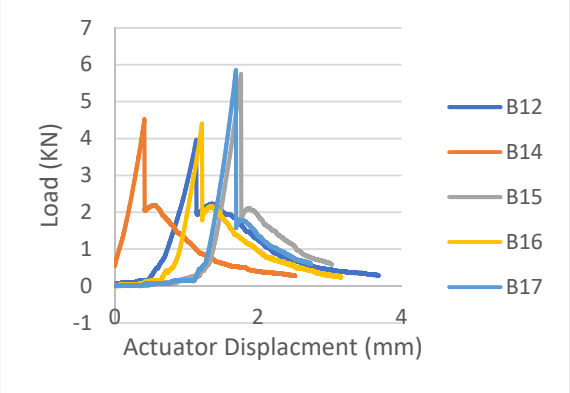

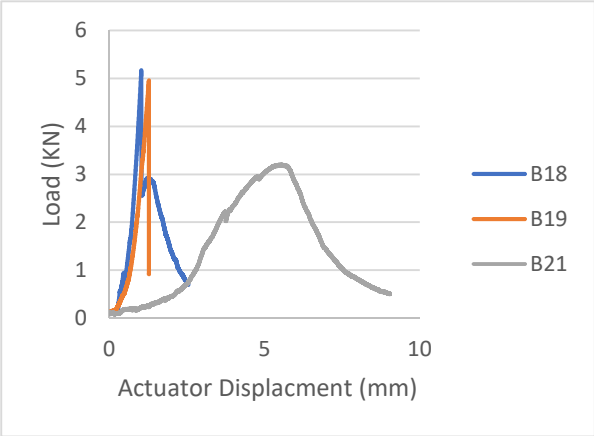

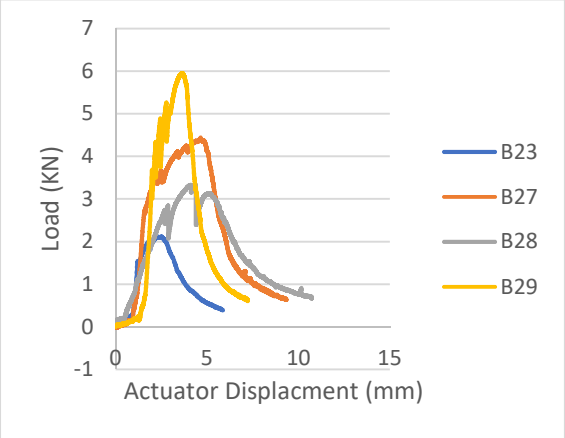

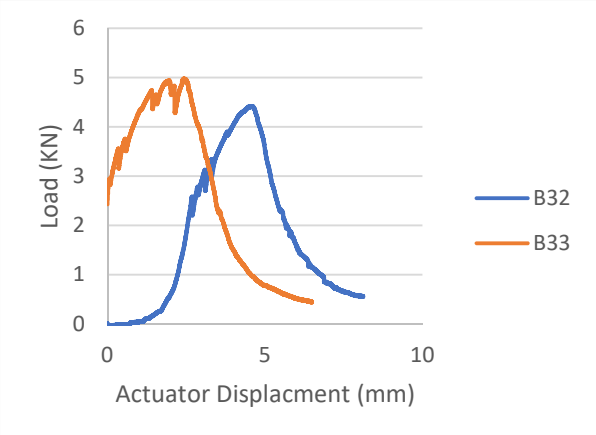

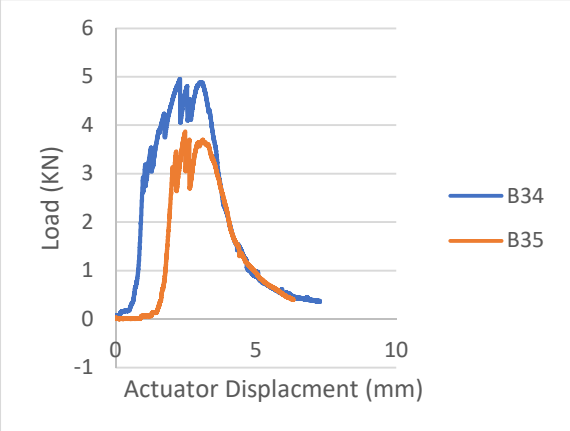

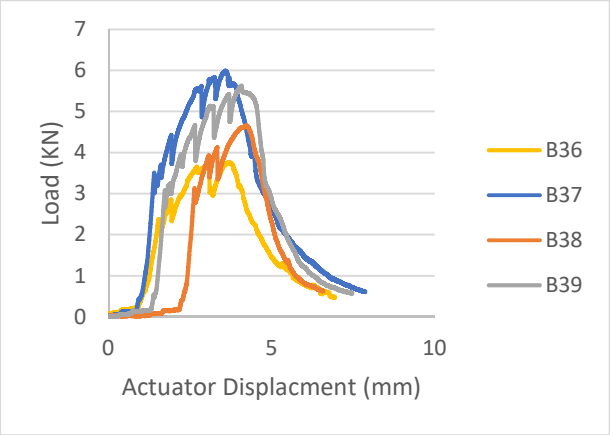

B5: Failure Cracks of SHFRCC Specimens

B5.1: Failure cracks of long and short flexural prisms

S1; S2 (long prisms)

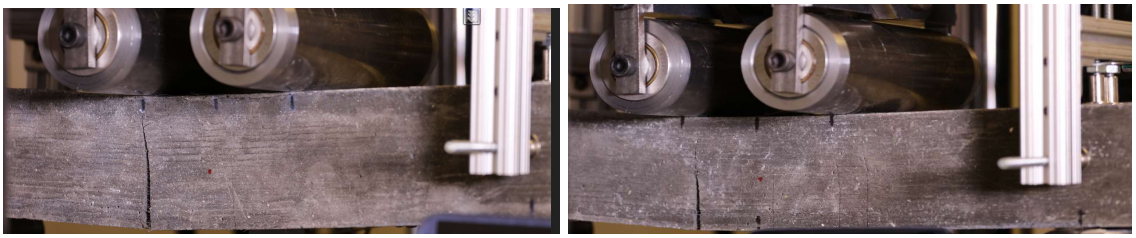

S3; S4 (long prisms)

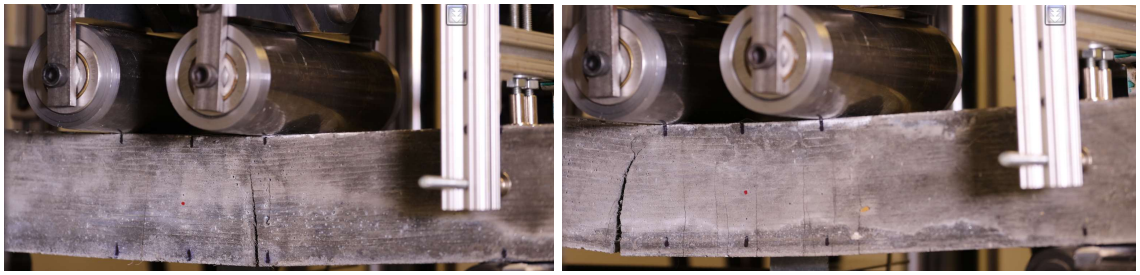

S1; S2 (short prisms)

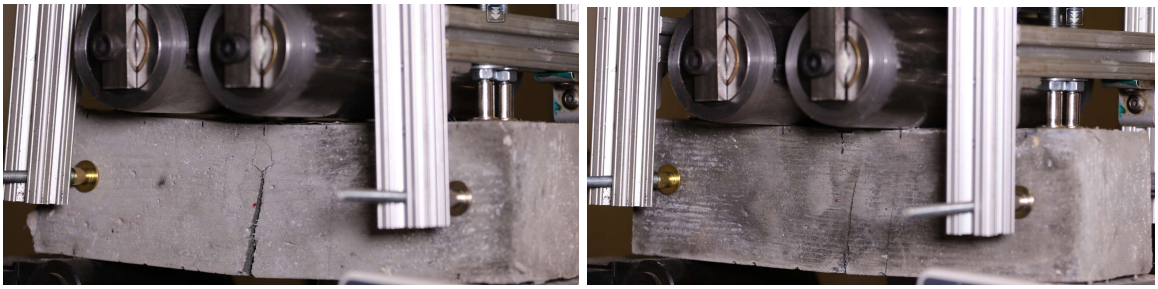

B5.2: Failure cracks of front and back of Push-off Specimens

PS1

PS2

CS1

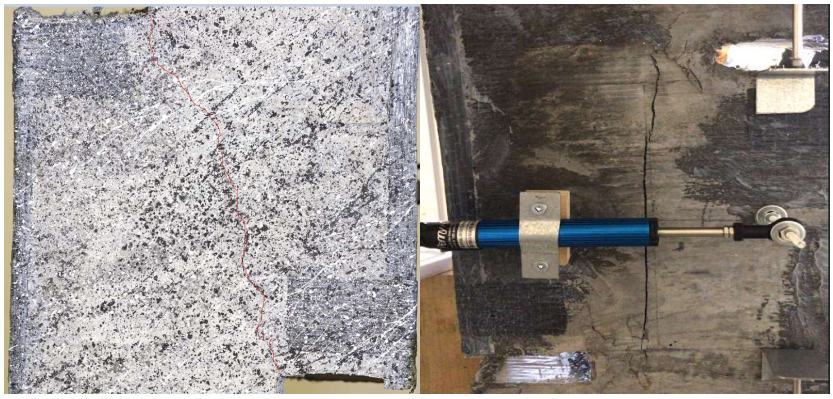

CS2

SPS1

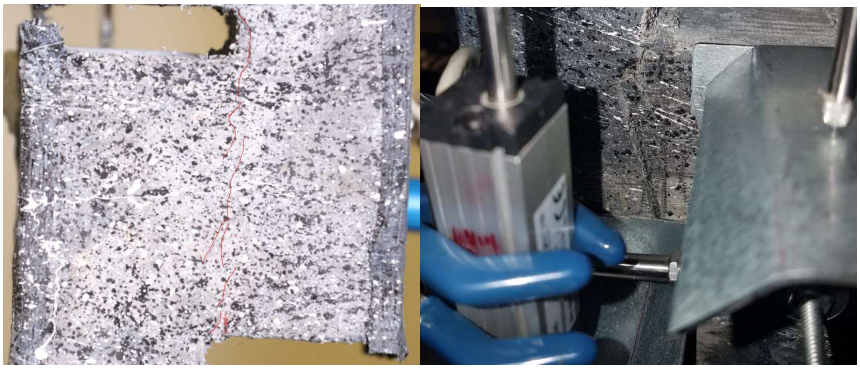

SPS2

SCS1

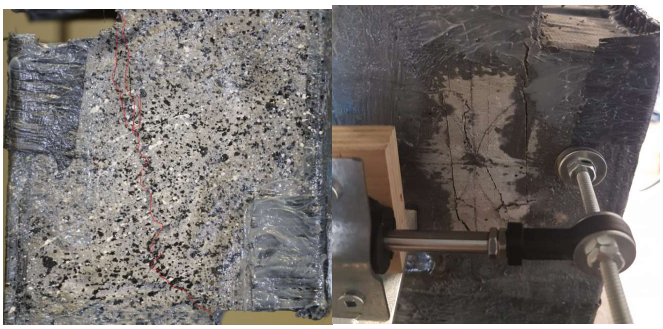

SCS2

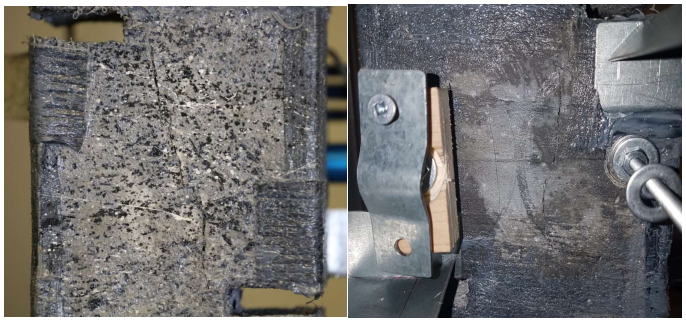

CS'1; CS'2

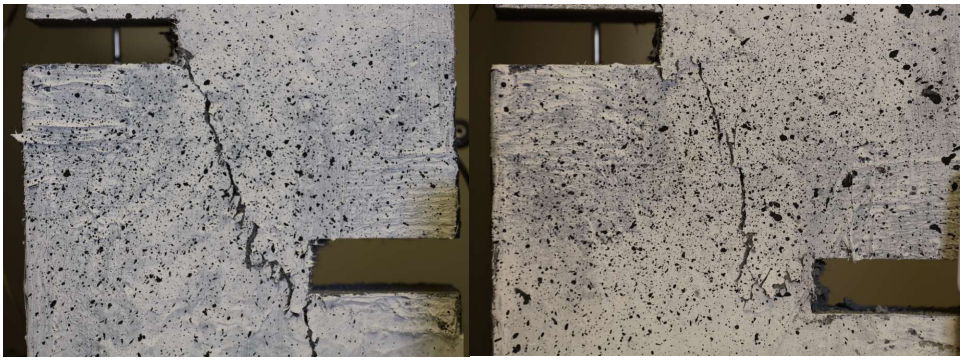

TS1

TS2

B6: Fiber distribution in the failed parts of specimens

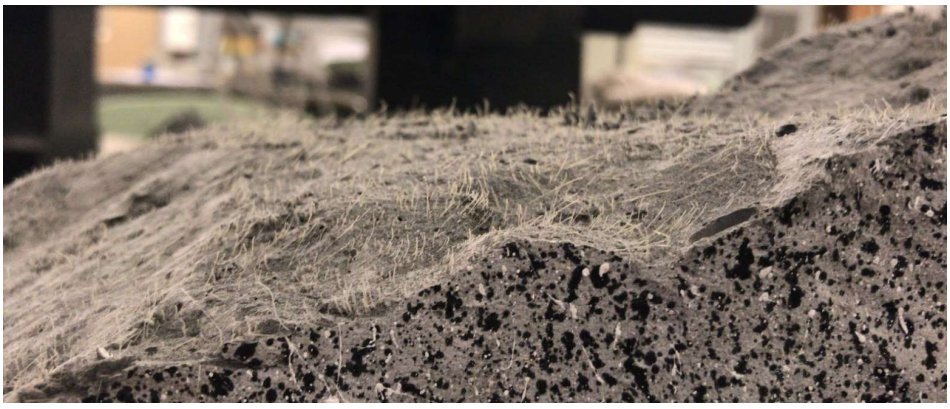

B7: The exact locations of the selected points (red dots) to extract displacements from DIC software (GeoPIV)

- **Compression Prisms**

M1; M2

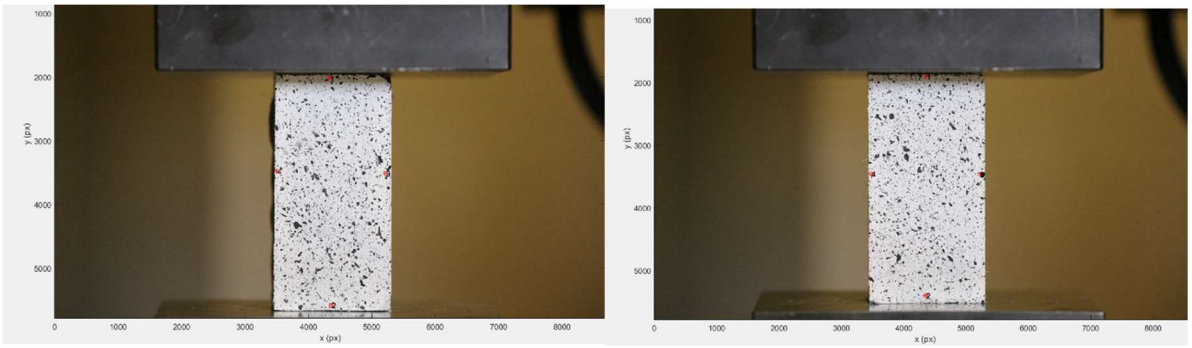

M4; M5

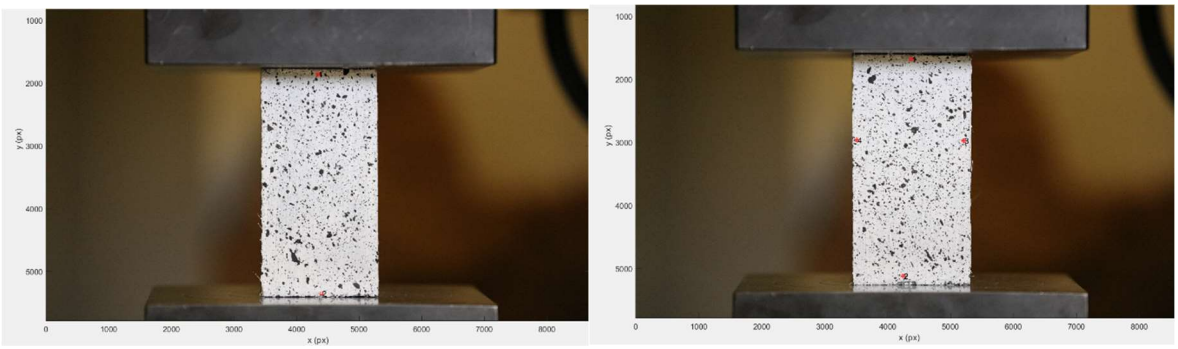

- **Long Prisms**

S1; S2

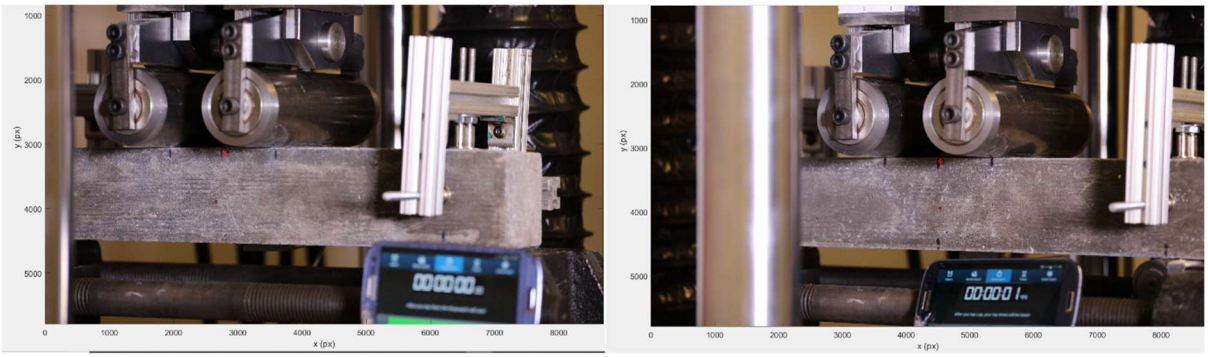

S3; S4

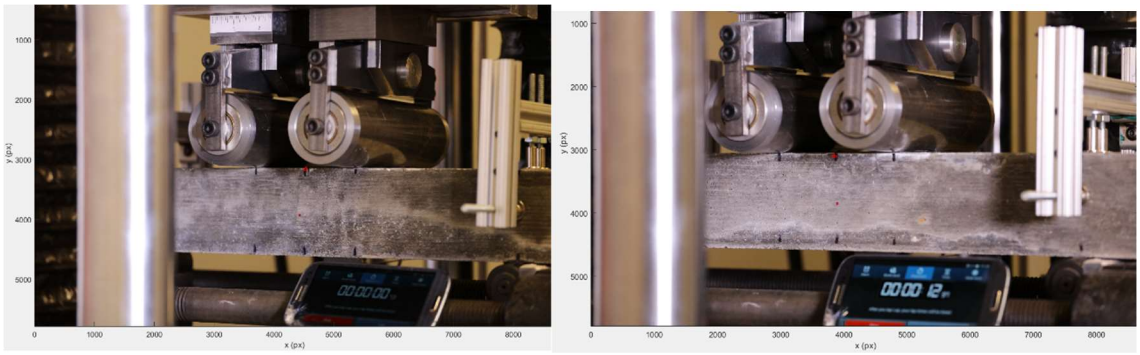

- **Short Prisms**

S1; S2

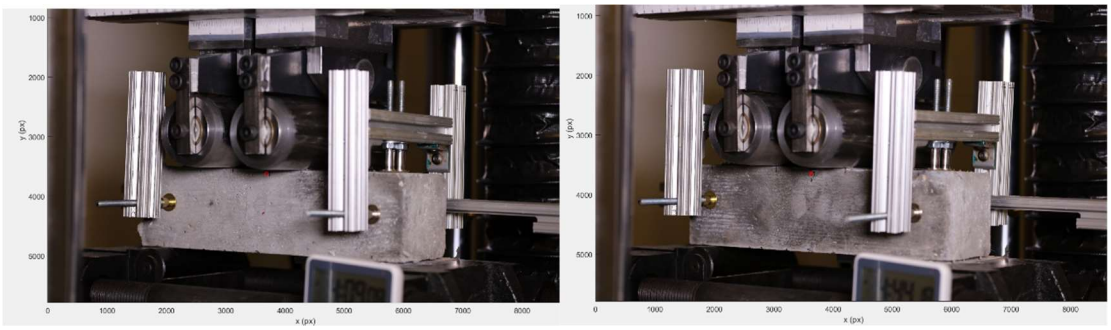

- **Push-off Specimens**

PS-S1; PS-S2

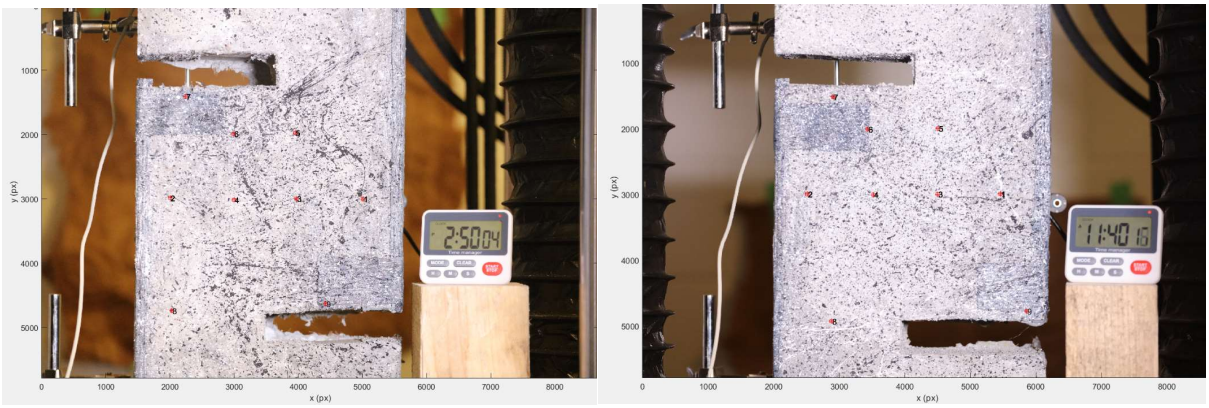

CS-S1

CS-S2

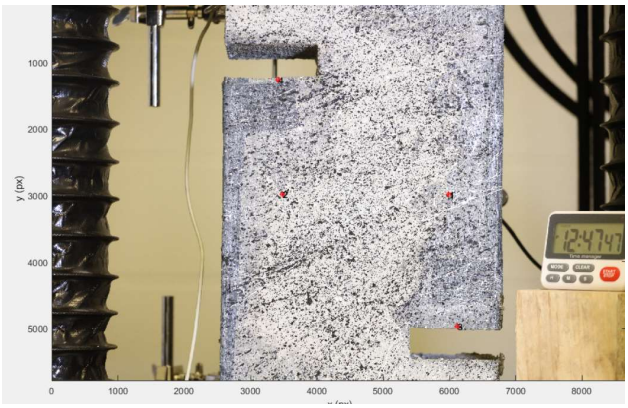

SPS-S1; SCS-S1

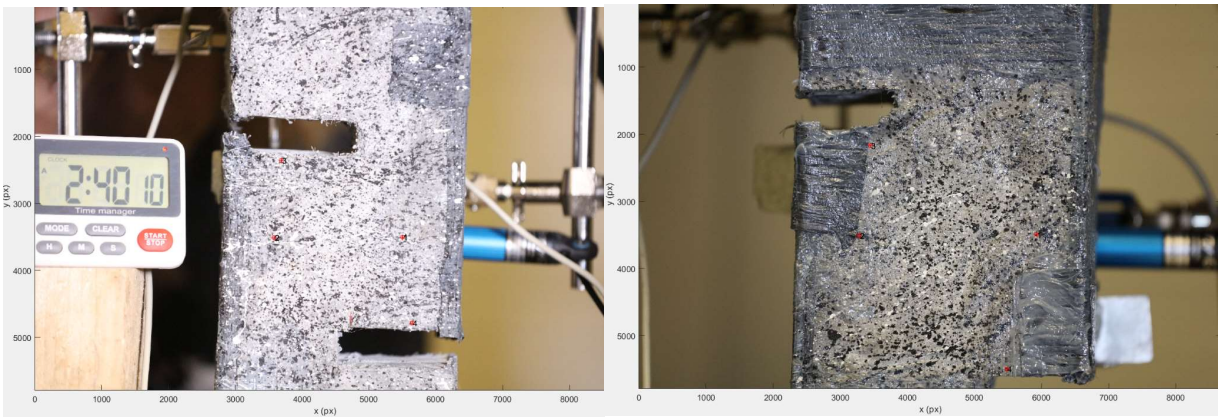

SCS-S2

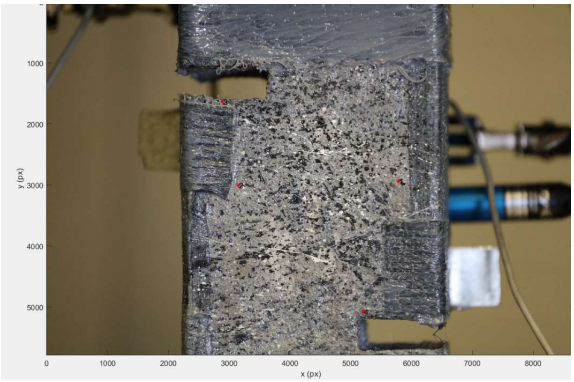

CS'-S1' SCS'-S2

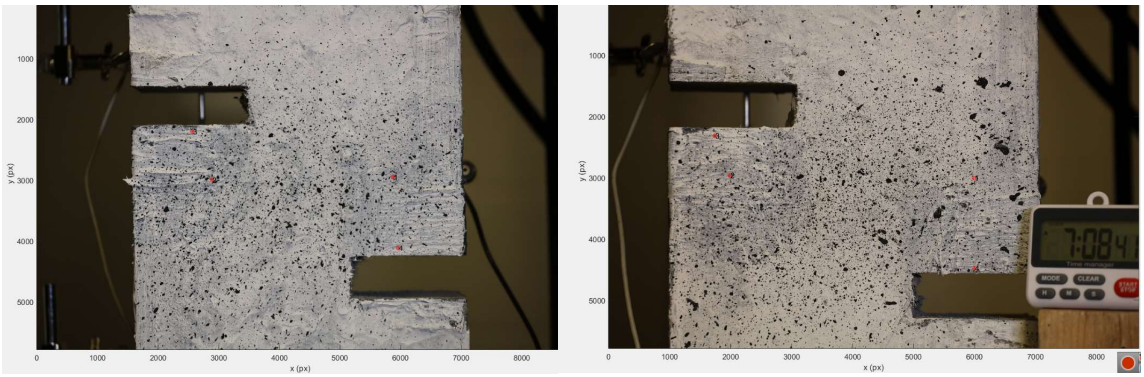

TS-S1; TS-S2

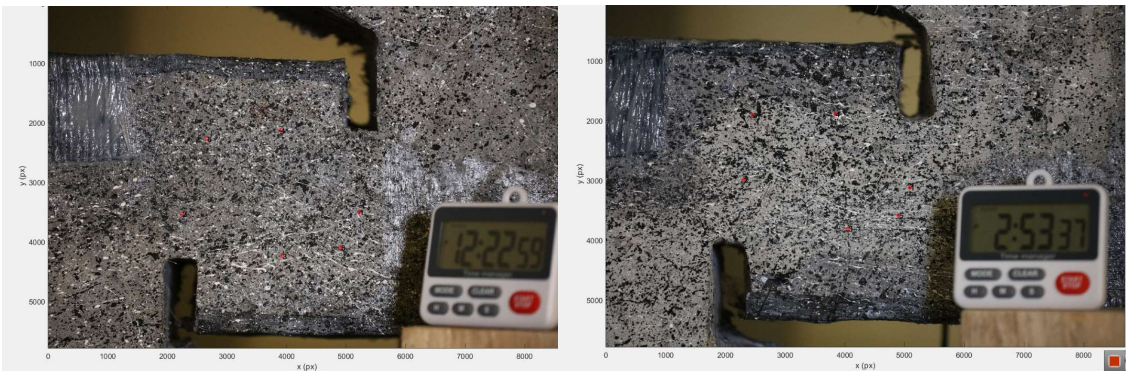

APPENDIX C: PVA-DATABASE

	Beam Properties									Peak Load (kN)	Fiber Properties				
	Beam No.	b	h	d	L	a/d	No. Bar (Bottom)	No. Bar (Top)	fc (MPa)		Fiber Volume Fraction %	Fiber Length (mm)	Fiber Diameter (mm)	Tensile Strength Mpa	Elastic modulus Gpa
R1	B1L8	100	100	-	-	1	2 @ 8mm	-	52	88.402	2	12	0.039	1600	40
	B2L8	100	100	-	-	2	2 @ 8mm	-	52	52.709	2	12	0.039	1600	40
	B2L14	100	100	-	-	2	2 @ 14mm	-	52	85.329	2	12	0.39	1600	40
R2	R/ECC-0	125	250	212	1100	1.4	2 * Φ16	2 * Φ16	53.6	300	2	8		1560	40
R3	U2-w0	120	180	146	850	2.06	1 * Φ18 + 1 * Φ20	-	46.59	191.72	2	12	0.04	1600	40
	U3-w0	120	180	146	1150	3.08	1 * Φ18 + 1 * Φ20	-	45.7	133.2	2	12	0.04	1600	40
	U4-w0	120	180	146	1450	4.11	1 * Φ18 + 1 * Φ20	-	45.7	101.34	2	12	0.04	1600	40
R4	PVA10	180	280	243.5	-	1.5	8-D13	8-D13	37.3	247.8	1	12	0.04	1600	40
	PVA15	180	280	243.5	-	1.5	8-D13	8-D13	35.7	285.6	1.5	12	0.04	1600	40
	PVA20	180	280	243.5	-	1.5	8-D13	8-D13	39.1	365.4	2	12	0.04	1600	40
R5	ECC beam 1A	125	250	215	1130	1	2 * Φ16	-	49.1	501.47	2	8	0.039	1610	N/A
	beam 1B	125	250	190	1080	1	4* Φ16	-	49.1	550.91	2	8	0.039	1610	N/A
	beam 2A	125	250	215	1560	2	2 * Φ16	-	49.1	220.66	2	8	0.039	1610	N/A
	beam 2B	125	250	190	1460	2	4 * Φ16	-	49.1	290.83	2	8	0.039	1610	N/A
	beam 3A	125	250	215	1990	3	2 * Φ16	-	49.1	143.27	2	8	0.039	1610	N/A
	beam 3B	125	250	190	1840	3	4 * Φ16	-	49.1	190.59	2	8	0.039	1610	N/A